THE UNIVERSITY OF CHICAGO

QUANTUM MATTER SYNTHESIZER: SEEING AND ARRANGING ATOMS IN AN OPTICAL LATTICE

A DISSERTATION SUBMITTED TO
THE FACULTY OF THE DIVISION OF THE PHYSICAL SCIENCES
IN CANDIDACY FOR THE DEGREE OF
DOCTOR OF PHILOSOPHY

DEPARTMENT OF PHYSICS

BY
MINGJIAMEI ZHANG

CHICAGO, ILLINOIS
AUGUST 2025

To my beloved family and friends

What's past is prologue.

TABLE OF CONTENTS

LIST OF FIGURES

LIST OF TABLES

ACKNOWLEDGMENTS

First of all, I would like to thank my advisor, Prof. Cheng Chin for his guidance and support over the last few years. He is a very experienced experimentalist and a patient teacher, always available for discussion and willing to share his expertise on all aspects of an experiment. He is also very devoted to educating junior students in the lab by organizing reading groups and tutorials on the fundamentals. The years in the group really deepened my understanding of the state-of-the-art of cold atoms research.

I would also like to thank all the people that I worked with in the QMS experiment: Mickey, Jon, Lauren and Evan. Mickey was a postdoc when I was a summer undergrad in 2017, and we briefly overlapped during my first year in the PhD program. He taught me a lot of tricks to align optics and his humor has always enlightened the lab. Jon is the person with whom I spent most of my time working. He is also the first PhD graduate who participated in the very early stage the project and has shared a lot of his knowledge and experience to me. It was only after he graduated that I began to realize how fortunate I had been to have someone in the lab who was familiar with every detail of the setup. Lauren and Evan are the younger generation students and have made increasingly significant contributions to the project over the last two years. I wish them all the best in carrying forward the QMS mission and hope they enjoy the journey of developing the new entangled photon source.

I also want to thank the other past and current members of the Chin group: Zhendong, Kevin, Lei, Shu, Frank, Krutik, Brian, Henry, Sarah, Tadej, and new members Lambert, Rahaf, Claire and Bethel. Thank you for making Chin lab a friendly place to work with and generously supporting other members. The PhD is never easy - we need to overcome huge challenges to make meaningful progress. None of it would be possible without everyone's effort, either directly or indirectly.

I want to thank Brenda for organizing JFI coffee hours, Maria for handling reimbursements, and Bentley for managing the building. I want to thank Putri and Zosia in the Physics

department for helping with the administrative issues, and the Office of International Affairs for all the immigration related support.

I want to thank my parents, who always encourage me not to overestimate the trouble. I also want to thank my sister Jiali and my brother-in-law Xiaosong. You always welcome me to your California home and support me exploring different career options. I want to thank my husband, Jinyang. The joyful moments we share constantly remind me that, beyond the research, there are so many other things in life that I deeply value.

I also want to thank my friends at UChicago, Northwestern, and the Chinese Christian Church. Many of us are or were Chinese PhD students, and we share many common challenges, wether related to research, family, career and immigration policies. I am grateful to be a member of such a wonderful community, where I always feel understood and free to share my thoughts openly.

These past few years have been the most challenging of my life. Experiments are never easy - *everything* has to go right for them to work, and often, just one thing going wrong is enough to bring it all down. They are even harder because *nobody* has done it before - you are venturing unknown territory, and more often than not, you discover something you overlooked in the beginning only when it is too late to change it easily. Through cycles of failure and perseverance, you eventually learn something, about the physics and also about yourself. Looking back, I feel that I've grown from a naive - yet fearless - young person into a more mature, resilient and responsible individual. That, perhaps, is the most valuable lesson I've learned from my PhD.

ABSTRACT

Quantum simulation with ultracold atoms offers a powerful route to exploring complex quantum systems that are beyond the reach of classical computation. Two major experimental platforms have driven progress in this field: degenerate quantum gases in optical lattices, which enable the study of many-body dynamics governed by Hubbard-type Hamiltonians; and reconfigurable Rydberg atom arrays, which provide programmable geometries for quantum information processing.

This thesis presents the development of a new experimental platform, the Quantum Matter Synthesizer (QMS), which integrates the strengths of both approaches by combining dynamic tweezer arrays with optical lattices. The envisioned QMS experiment contains three main steps. First, we stochastically load a thermal atomic gas into a two-dimensional optical lattice, and perform site-resolved imaging to determine the initial atom occupancy. Second, dynamic optical tweezers are applied to rearrange the atomic distribution into a desired target configuration. Third, after the rearrangement, we perform a second imaging to verify the resulting atom distribution, and subsequently cool the atoms to their motional ground states to enable coherent many-body dynamics.

This thesis presents the design and characterization of the QMS, with emphasis on the two key capabilities: site-resolved imaging and integration of dynamic optical tweezers. We highlight the dual-objective microscope setup that demonstrates excellent mechanical stability. We detail the implementation of optical trapping using a triangular lattice in conjunction with a light sheet, and fluorescence imaging based on degenerate Raman sideband cooling. This configuration enables high-fidelity, diffraction-limited, site-resolved imaging of atoms in the lattice. We also describe the implementation of an innovative scheme for real-time control of optical tweezers using digital micromirror devices (DMD), operating at a binary pattern refresh rate of 2.88 kHz. We present the calibration procedure for addressing individual lattice sites with DMD-generated patterns, along with initial results demonstrating

controlled atom transport using dynamically shifting tweezers.

The future integration of ground-state cooling will allow rapid and flexible initialization of many-body quantum states, enhancing preparation and manipulation of strongly correlated atomic systems through independent control of single atoms.

CHAPTER 1
INTRODUCTION OF THE QUANTUM MATTER SYNTHESIZER

1.1 Degenerate quantum gas for quantum simulation

Ultracold alkali atoms, characterized by highly controllable collisional properties and well-understood electronic structures, have served as a valuable platform for both experimentalists and theorists to explore complex quantum phenomena over the past few decades [1]. As the temperature approaches absolute zero and random thermal motion freezes, intriguing quantum dynamics starts to emerge. One of the most well-known phenomena is the formation of a Bose-Einstein Condensate (BEC), which occurs when the thermal de Broglie wavelength $\lambda_{dB} = \hbar/(2Mk_BT)^{1/2}$ of bosons becomes comparable to the interatomic separation, causing atomic wavefunctions to overlap and become indistinguishable [2, 3, 4]. This results in a *degenerate* state where a macroscopic number of atoms occupy the same quantum state. With the ability to precisely tune the interatomic interaction through Feshbach resonances [5], degenerate quantum gas provides a clean and versatile system that enables experimental study of a wide range of physics, including quantum phase transition[6], many-body chemical reactions [7], mediated interactions [8], etc. The overlapping wavefunctions and controllable interaction make degenerate quantum gas particularly suitable for engineering strongly-correlated many-body state, which is challenging to achieve in other platforms.

An important application of degenerate quantum gas experiment is *quantum simulation*, which is to simulate the dynamic of one complex quantum system by experimentally probing another quantum system that follows a Hamiltonian with a similar form, instead of running simulation on a classical computer [9]. Unlike *quantum computation*, which aims to provide a universal framework for harnessing quantum mechanics to solve a broad range of problems, quantum simulation is typically platform-specific - the Hamiltonian governing the physical

system inherently limits the class of models that can be simulated. Although quantum simulation might not be universally applicable to different problems, it offers a viable alternative for gaining insights into the complex quantum dynamics, especially when the system of interest is more difficult to directly control or probe than the simulation platform, and when the classical simulation proves computationally challenging. One example is the dynamics of strongly correlated electrons in a solid material which explains the emergence of high-temperature superconductivity. Such problem is beyond the capability of current theoretical tools and computational methods, but can be simulated using an ultracold atom system [10].

The potential of quantum simulation goes well beyond emulating condensed matter systems. For instance, the dynamics of the evolution of the early universe [11, 12] and Unruh radiation in a curved space-time [13] can all be simulated with degenerate quantum gas. As atomic physicists gain access to an expanding tool-sets, the range of problems that quantum gas experiments can simulate continues to grow, making the present to be an exciting era for innovation and development. As Richard Feynman famously said, *"Nature isn't classical, dammit, and if you want to make a simulation of nature, you'd better make it quantum mechanical, and by golly it's a wonderful problem, because it doesn't look so easy"* [14]. Using a quantum system to simulate quantum behavior is the most natural and accurate approach, though certainly not without its challenges.

1.2 Development of cold atom toolboxes

Since the advent of laser cooling and trapping techniques in 1980s [15], the cold atoms experimental toolboxes have expanded rapidly. From thermal to degenerate quantum gases [16], from alkali atoms to more complex species[17, 18], from neutral atoms to ultracold molecules [19, 20], and from atomic ensembles to single atoms [21, 22] - driven by the pursuit of increasingly challenging and elusive problems, the continuous advancement of control and detection technologies has remained a persistent theme throughout history.

1.2.1 Quantum Gas Microscope

One popular cold atom platform that has been developed for quantum simulation is *Quantum Gas Microscope* (QGM) based on degenerate quantum gas trapped in an optical lattice. The optical lattice provides scalable microtraps (lattice sites) at sub-micrometer spacing to confine single atoms and to access various quantum spin models [23]. The integration of high Numerical Aperture (NA) microscope offers diffraction-limited optical resolution which enables imaging and control at single site level [24, 25, 26, 27, 28]. In the recent years, site-resolved imaging has been demonstrated on alkali-earth and alkali-earth-like atomic species [29, 30], dipolar quantum gas [31], ultracold molecules [32] and in non-standard lattice geometries [33, 34]. With advanced techniques that involves a bilayer system to circumvent the pairwise loss due to light-assisted collisons from imaging, full spin- and density-resolved images has also been achieved [35, 36].

In a QGM system, the dynamic of interacting atoms in a lattice potential is usually described by a Hubbard model Hamiltonian. For bosonic atoms, the Bose-Hubbard Hamiltonian reads [37]:

$$H = -J \sum_{\langle i,j \rangle} \left(\hat{a}_i^\dagger \hat{a}_j + \hat{a}_j^\dagger \hat{a}_i \right) + \frac{U}{2} \sum_i \hat{n}_i (\hat{n}_i - 1) + \sum_i \epsilon_i \hat{n}_i \tag{1.1}$$

Here $\langle i, j \rangle$ denotes adjacent pairs of lattice sites, $\hat{a}_i$ and $\hat{a}^\dagger$ denotes the bosonic annihilation and creation operators of atoms on the ith lattice site, $\hat{n}_i = \hat{a}_i^\dagger \hat{a}_i$ is the atomic number operator on the ith lattice site, and ϵ_i is the energy offset of the ith lattice site due to harmonic envelope of the trapping lasers. In this model, atoms trapped in the same lattice site interact with a short-range interaction characterized by U, which is proportional to the s-wave scattering length a and the overlapping of single-particle wavefunction $w(\mathbf{x})$:

$$U = \frac{4\pi\hbar^2 a}{m} \int |w(\mathbf{x})|^4 \, \mathrm{d}^3 x \tag{1.2}$$

The coherent tunneling between neighboring sites is characterized by J, which is the matrix elements between wavefunction at neighboring sites:

$$J = -\int \mathrm{d}^3x \; w(\mathbf{x}-\mathbf{x}_i)\left(-\frac{\hbar^2\nabla^2}{2m} + V_{lat}(\mathbf{x})\right) w(\mathbf{x}-\mathbf{x}_j) \tag{1.3}$$

Here $V_{lat}(\mathbf{x})$ denotes the lattice potentials.

In an experiment, the scattering length a can be tuned using an external magnetic field via a Feshbach resonance [5], allowing precise control over the on-site interaction strength U. The lattice laser intensity can also be tuned to control the spatial extent of single particle wavefunction $w(\mathbf{x})$, which in turns affects both on-site interaction U and the tunneling J. With precise tuning of experimental parameters, a QGM can access a wide range of the tunneling J and on-site interaction U, making it a powerful platform for simulating and exploring the complex phases and quantum phase transitions predicted by Hubbard model.

A typical QGM experiment starts with preparation of degenerate quantum gas from room-temperature atoms through multiple stages of cooling. By adiabatically loading the degenerate gas to lattice to a Mott-insulating regime, one can obtain near unity filling. This uniform atomic sample can then be cookie-cut into a predefined configuration suited for the specific experimental objective [38]. Such preparation requires extensive optical setup and relatively long experimental cycle time, usually on the order of a few to tens of seconds. Although recent effort has shown the promise of creating quantum degenerate gas in a much shorter time without the time-consuming evaporative cooling [39, 40, 41, 42, 43], such technique has not yet been integrated to QGM experiments. Additionally, since atoms are heated during imaging, site-resolved detection is typically performed as the final step of the experimental sequence, after which the atoms are discarded. This inherently reduces time efficiency, as a fresh atomic sample must be prepared for each repetition. The resulting long experimental cycle time in QGM platforms presents a significant limitation for studies that rely on extensive statistical averaging — for instance, boson sampling via quantum

walks in optical lattices [44]. It also poses challenges for applications aiming to demonstrate computational speedups over classical approaches.

1.2.2 Reconfigurable Rydberg atom arrays

More recently, reconfigurable Rydberg atom arrays have emerged as a promising platform for quantum simulation and quantum information processing [21, 22]. Like optical lattice experiments, these systems employ arrays of microtraps - commonly referred to as optical tweezers - to confine individual atoms. Unlike lattices formed by optical interference, these microtraps are generated by individually focusing laser beams through a high NA objective. The typical spacing between optical tweezers is on the order of a few micrometers. This relatively large inter-site separation facilitates unambiguous detection of individual atoms. However, it simultaneously suppresses coherent tunneling between sites, making it challenging to realize Hubbard-model dynamics in optical tweezer arrays. When optical tweezers are brought sufficiently close, coherent tunneling between adjacent sites has been observed [45, 46]. However, scaling such configurations to thousands of sites remains challenging, in contrast to optical lattice systems where large-scale arrays with coherent dynamics are more readily achieved [47].

To induce interactions between atoms confined in spatially separated tweezer sites, long-range interactions are required. These are typically introduced by exciting the atoms to Rydberg states with high principal quantum numbers, which give rise to strong long-range van der Waals interactions [48].

Preparing defect-free atom arrays in tweezer-based systems is technically more challenging than in lattice-based platforms. Tweezer-based systems typically do not require starting from a degenerate quantum gas. As a result, in the absence of a Mott-insulating regime, the initial atom loading process is inherently stochastic. To prepare near-unity loaded array, early efforts focused on enhancing loading efficiency using blue-detuned laser shielding

techniques [49, 50]. More recently, attention has shifted toward rearranging atoms by dynamically moving optical tweezers during an experimental sequence. The introduction of dynamic reconfigurability has proven to be a key enabling technique - not only facilitating the preparation of defect-free atom arrays, but also expanding the scope of research by providing enhanced programmability and control [51, 52, 53].

Today, reconfigurable atom arrays have emerged as a leading platform for building neutral atom quantum computers in both academia and industry settings [54, 55]. Recent developments in reconfigurable atom arrays have emphasized improving scalability [56, 57] and demonstrated quantum error correction protocols for the realization of logical qubits [53].

1.2.3 Bridging the two platforms

Although both QGM and reconfigurable atom arrays are based on arrays of microtraps and have demonstrated high-fidelity single atom imaging and control, they rely on distinct underlying technical infrastructures. There are on-going efforts to bring the technical tools from one platform to the other, particularly with emphasis on integrating optical lattices into reconfigurable atom array experiments. Some experiments use the lattice to create scalable trapping sites, serving as a reservoir or "storage" medium for the tweezer-trapped atoms [55, 57]. Other experiments focus on enabling access to the coherent tunneling, which is characteristic of lattice system, in tweezer-trapped atom arrays. For instance, in recent work from JILA, by implanting tweezer-loaded atoms to an optical lattice, people can access Hubbard model coherent tunneling between large number of lattice sites similar to a QGM experiment [58, 44].

However, as far as we are aware, there is no known demonstration of integration of the key technology of reconfigurable atom arrays platform - dynamic tweezers - into a QGM system This thesis focuses on our efforts to develop a new experimental platform, the *Quantum Matter Synthesizer*, which combines the strength of the two platforms by integrating

dynamic optical tweezers into a lattice system. As part of this work, we introduce an innovative scheme for generating moving tweezers using a digital micromirror device (DMD). Once established, this technique can be readily adopted by existing quantum gas microscope (QGM) experiments to enhance control and programmability, with the potential to significantly reduce experimental cycle times and enable continuous operation of the experimental sequence.

1.3 Roadmap to quantum degeneracy via atom assembly

1.3.1 Working principle of the QMS

Quantum Matter Synthesizer (QMS) is the next generation quantum simulation platform that integrates dynamic tweezers to an optical lattice experiment using ultracold Cesium (^{133}Cs) atoms. Based on a typical QGM architecture, the QMS aims to introduce dynamic tweezer rearrangement to enable fast preparation of a degenerate quantum gas at a predefined configuration in a lattice. As illustrated in Fig. 1.1, the working principle of the system is detailed as follows:

1. **Loading and imaging a thermal gas in an optical lattice.** We begin by preparing a thermal atomic gas and loading it into an optical lattice, followed by site-resolved imaging to determine atom occupancy. Due to the stochastic nature of the loading process, the resulting initial distribution of atoms is random.

2. **Rearrangment of atom occupancy.** After extracting the initial occupancy from the first image, we turn on optical tweezers at the positions of the lattice-loaded atoms and dynamically rearrange them to their target locations.

3. **Cooling to quantum degeneracy.** Following tweezer rearrangement, we verify the final atom occupancy by taking a second site-resolved image. Subsequently, we apply

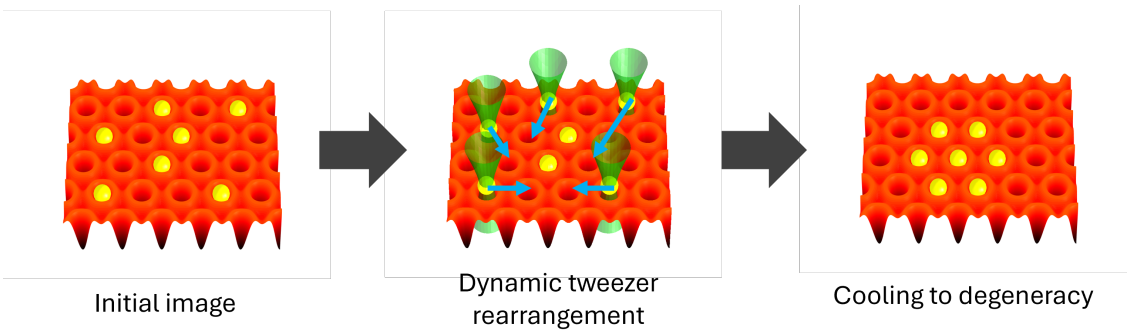

Figure 1.1: Working principle of the Quantum Matter Synthesizer (QMS). Starting from an initial site-resolved image of atom occupancy in an optical lattice, QMS aims to introduce dynamic tweezers to reconfigure atom occupancy, and finally verify such reconfiguration with a second site-resolved image.

efficient ground-state cooling to bring the assembled atoms to their motional ground states at the respective lattice sites. To achieve quantum degeneracy, we adiabatically lower the lattice depth, allowing atomic wavefunctions at adjacent sites to overlap and establish coherent many-body dynamics.

This procedure, enabled by dynamic tweezer technology, represents a departure from the conventional approach to preparing a degenerate quantum gas via evaporative cooling. Moreover, it is also a demonstration of the concept of *Maxwell's demon* similar to the work in Ref. [59]. By gathering information of the atom occupancy which increases the entropy of the outside world, the guided rearrangement lowers the system configurational entropy.

There are three major technical goals for completing the QMS platform:

- **Seeing**: High-fidelity site-resolved imaging in an optical lattice.
- **Arranging**: Ability to rearrange atom occupancy in the lattice with dynamic tweezers.
- **Ground-state cooling**: Efficient cooling to motional ground state at the lattice sites.

This thesis will focus on the development on *Seeing* and *Arranging*, while also provide outlook on future implementation of *Ground-state cooling* in the current system.

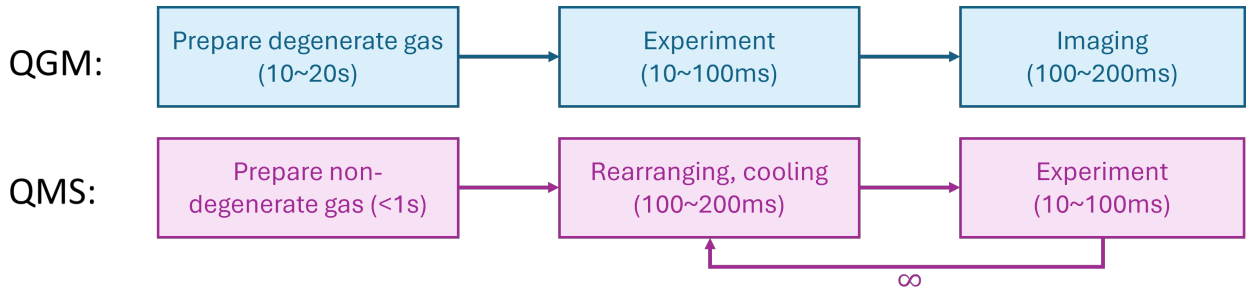

Figure 1.2: Technical applications of QMS. With dynamic rearrangement and ground-state cooling, QMS aims to shorten the time to prepare a degenerate quantum gas in the QGM experiment, and achieve continuous operation by dynamically recycling atoms in the sequence.

1.3.2 Applications of the QMS

One direct application of QMS is to demonstrate faster preparation of a degenerate quantum gas and continuous operation with dynamic atom recycling. A typical QGM experiment starts with preparation of a degenerate gas, which usually takes several to tens of seconds. After the sample preparation, the experiment stage involves introducing coherent tunneling between lattice sites. In the subsequent imaging stage, site-resolved measurements are performed to extract the atom occupancies within the lattice. In QMS, the use of the "rearrange and cool" protocol allows one to bypass the time-consuming evaporative cooling typically required for producing a degenerate gas. As a result, the time to reach quantum degeneracy can be reduced to approximately one second, compared to the tens of seconds typically needed in standard QGM experiments. Additionally, if atoms are not lost during the experiment stage, the tunneled atoms can be re-collected by the dynamic tweezers and re-cooled for use in the next round of experiment. For a typical atom lifetime of 20 seconds and the estimated recycle time of 400 ms, atoms can be reused for over ten experimental cycles before requiring re-preparation.

In addition to the technical advancements, QMS also enables access to problems that require coherent tunneling between lattice sites similar to a traditional QGM, while offering added advantage from fast and deterministic initial state preparation. One example is

quantum walk in a 2D lattice [60, 61, 47]. With controllable interaction, we could explore the strong interacting regime where the two-particle correlation is expected to resemble a non-interacting Fermionic statistics [62]. Another example is collective effect from ordered atom arrays with sub-micrometer spacing. Such arrays prepared by QMS can be utilized to engineer emitter-photon interactions [63]. Moreover, there is ongoing development of narrow line-width entangled photon source in Chin Lab and integrating the single-photon source with the single-atom control of the QMS platform presents an exciting avenue for future research on quantum networking with hybrid systems. Additionally, the dual objectives configuration of QMS offers the capability to image single atoms in a two-layer lattice, which could be an interesting direction to explore [64].

1.4 Outline of the thesis

This thesis is organized as follows:

- Chapter 2 reviews properties of cesium atoms and introduces fundamental concepts for modeling atom-light interaction with their applications to QMS experiments.
- Chapter 3 provides a brief overview of the system, including the vacuum system, lasers, microwave and magnetic field control, and computer control architecture.
- Chapter 4 introduces the design and construction of the system, including scheme and performance for long-distance optical transport, three-layer optical layout that combines lattice and tweezers, stable mounting structure for dual objectives, and stability measurement of the projected potentials.
- Chapter 5 details the optical trapping, cooling and site-resolved imaging in the glass cell, including the optical setup for 2D triangular lattice and light sheet, implementation and performance of degenerate Raman-sideband cooling, and image processing algorithms for reconstructing site-wise counts and occupancy statistics.

- Chapter 6 describes the current state of tweezers integration in the QMS apparatus, including the optical setup for direct projection, scheme for fast real-time control of projected patterns, calibration of frame transformations to address single lattice sites, long-term stability measurement, and results on transporting atoms with moving patterns.
- Chapter 7 will conclude the thesis and discuss the outlook of this experiment.

CHAPTER 2

FUNDAMENTALS

In this chapter, we begin with a brief overview of the relevant properties of cesium atoms, followed by a review of fundamental concepts for modeling atom-light interaction with the emphasis on the applications in the QMS experiment.

2.1 Properties of Cesium atoms

In the QMS experiment, we use ultracold ^{133}Cs atoms, the only stable isotope of cesium and the heaviest element in the alkali metal group. It has a nuclear spin of $I = 7/2$ and one unpaired electron. The electronic ground state $6S_{1/2}$ has two hyperfine levels $F = 3$ and $F = 4$ which are splitted by the exact clock transition frequency 9.192631770 GHz.

In the experiment, we use resonant lasers near 852 nm, corresponding to the D2 transition ($6S_{1/2}$ to $6P_{3/2}$). The other transition from the ground state to the $6P_{1/2}$ level is known the D1 line, which occurs at a wavelength of around 894 nm. The excited state of D2 line $6P_{3/2}$ is splitted into four hyperfine levels with quantum number $F' = 2, 3, 4, 5$ separated by about 150 to 250 MHz. These splittings are well resolved given the natural linewidth of the transition of about 5.2 MHz [65], which enables efficient sub-Doppler cooling using optical molasses.

At low temperature, atomic two-body elastic collisions can be fully described by the s-wave scattering length a which can be tuned by applying an external magnetic field through Feshbach resonance [66]. For Cs atoms at the absolute ground state $|F = 3, m_F = 3\rangle$ and zero field, the scattering length is large and negative $a \sim -2500a_0$, where $a_0 = 0.53$ Å is the Bohr radius. The scattering length has a zero crossing at $B = 17.1$ G, and there is a narrow g-wave resonance and a d-wave resonance below 50 G, which provides a convenient tuning knob for controlling the interatomic interaction.

2.2 Interaction with near-resonance light

When atoms interact with light, the oscillating electromagnetic field induces a frequency-dependent response, leading to both photon scattering and energy-level shifts. In a semi-classical model, the interaction between a classical electric field $\mathbf{E} = \frac{1}{2}\mathbf{E}_0 e^{i\omega t} + \text{h.c.}$ and atoms can be described by the Stark interaction Hamiltonian [67]

$$H_{Stark} = -\mathbf{d} \cdot \mathbf{E} \tag{2.1}$$

Here $\mathbf{d} = e\ \hat{\mathbf{r}}$ is the electric dipole operator. Considering atoms as a simple two-level system with a transition frequency ω_0 between the ground state $|g\rangle$ and the excited state $|e\rangle$, the application of an oscillating field at frequency ω introduces a coherent coupling between the two states which is governed by the detuning $\Delta = \omega - \omega_0$ and the Rabi frequency Ω

$$\Omega = \frac{\langle e|\mathbf{d} \cdot \mathbf{E}_0|g\rangle}{\hbar} = \frac{e\mathbf{E}_0}{\hbar} \cdot \langle e|\hat{\mathbf{r}}|g\rangle \tag{2.2}$$

Taking into account that the excited state decays to the ground state at a rate Γ due to spontaneous emission, the steady-state population at $|e\rangle$ is given by

$$\rho_{ee} = \frac{\Omega^2/4}{\Delta^2 + \Omega^2/2 + \Gamma^2/4} \tag{2.3}$$

The photon scattering rate is $\Gamma_{sc} = \rho_{ee}\Gamma$. When the driving field is strong and on-resonance, $\Delta = 0$ and $\Omega \gg \Gamma$, the excited state population saturates to $1/2$, and the scattering rate is $\Gamma/2$. Because the Rabi frequency is proportional to electric field amplitude, we can define a saturation parameter s and saturation intensity I_{sat} such that the Rabi frequency at this intensity is $\Gamma/\sqrt{2}$

$$s = \frac{I}{I_{sat}} = \frac{2\Omega^2}{\Gamma^2} \tag{2.4}$$

The photon scattering rate can then be expressed as

$$\Gamma_{sc} = \frac{\Gamma}{2} \cdot \frac{s}{1 + s + \left(\frac{2\Delta}{\Gamma}\right)^2} \tag{2.5}$$

For a two-level system, the spontaneous decay rate (or the natural linewidth) of the excited state Γ is related to transition dipole moment that characterizes the strength of coupling between $|g\rangle$ and $|e\rangle$ via the dipole operator $\hat{\mathbf{r}}$

$$\Gamma = \frac{e^2\omega_0^3}{3\pi\epsilon_0\hbar c^3} \, |\langle g|\hat{\mathbf{r}}|e\rangle|^2 \tag{2.6}$$

Combining Eqn. 2.2, Eqn. 2.4 and Eqn. 2.6, and the relationship between electric field amplitude and intensity $I = \frac{1}{2}c\epsilon_0|E|^2$, one can derive the expression of saturation intensity

$$I_{sat} = \frac{\hbar\omega_0^3\Gamma}{12\pi c^2} \tag{2.7}$$

If we set Γ and ω_0 according to Cs atoms D2 transition, this gives a saturation intensity of 1.10 mW/cm^2.

2.2.1 Absorption imaging

A common technique for measuring the density profile of an atomic cloud is absorption imaging. In this method, a resonant probe beam is directed through the cloud, where atoms absorb and scatter photons. The resulting shadow formed by the attenuation of the probe beam is imaged onto a CCD camera, allowing for spatially resolved measurement of the atomic column density.

Given a sample of atoms with spatial number density $n_{3D}(x, y, z)$, if the probe laser is

propagating along z direction, the photon scattering rate by atoms in a volume of $\mathrm{d}S\,\mathrm{d}z$ is

$$\frac{\mathrm{d}N_{photon}}{\mathrm{d}t} = -\Gamma_{sc} n_{3D}(x,y,z)\,\mathrm{d}S\,\mathrm{d}z \tag{2.8}$$

Each photon carries an energy of $\hbar\omega$ and the power is related to intensity by $P = I\,\mathrm{d}S$, then the attenuation of probe laser intensity is $\mathrm{d}I = -n_{3D}\cdot\hbar\omega\Gamma_{sc}\,\mathrm{d}z$. Assuming the light is on resonance ($\omega = \omega_0$), and combining with Eqn. 2.5 and Eqn. 2.7, we obtain the Beer-Lambert law for light attenuation through absorptive medium

$$\frac{\mathrm{d}I}{\mathrm{d}z} = -n_{3D}\ \sigma_0\ \frac{I}{1+I/I_{sat}} \tag{2.9}$$

Here we define the scattering cross section $\sigma_0 = 3\lambda^2/2\pi$ where λ is the transition wavelength. Integrate this expression in the beam propagation direction z, we can obtain the relationship between the integrated atomic column density $n(x,y) = \int n_{3D}(x,y,z)\,\mathrm{d}z$ and the attenuation in probe light intensity

$$n(x,y) = -\frac{1}{\sigma}\left\{\ln\frac{I_f(x,y)}{I_i(x,y)} + \frac{I_f(x,y)-I_i(x,y)}{I_{sat}}\right\} \tag{2.10}$$

Where I_i is the initial intensity of the probe beam and I_f is the final intensity after passing through the medium. This formula serves as the basis for calculating the atom column density from absorption images obtained in the experiments. In the limit when the probe beam is weak $I \ll I_{sat}$, the linear term can be neglected and the column density can be obtained directly from the optical density OD

$$OD(x,y) = -\ln\frac{I_f(x,y)}{I_i(x,y)} \tag{2.11}$$

To perform absorption imaging, we use a probe beam locked to the $4 \to 5'$ ($|F=4\rangle \to |F=5'\rangle$) cycling transition to resonantly excite atoms. We also have a repumping beam at

$3 \rightarrow 4'$ to recycle the atoms at $F = 3$ state back to $F = 4$ to ensure that they remain in the imaging cycle. The imaging pulse is usually 20 to 100 μs in length. To avoid the differential light shift introduced by the trapping lasers, we typically perform imaging shortly after releasing atoms into free space.

In a real experiment, extracting the atom number from images also requires calibrating the physical size corresponding to each camera pixel. This is typically done by releasing the atomic cloud into free space, tracking the center-of-mass position over time, and fitting the trajectory to that of free fall under gravity.

To measure the momentum distribution of an atomic cloud, one can release the atoms from their trapping potential and image the density profile after a time-of-flight (TOF) expansion. When the cloud expands such that its size significantly exceeds the initial spatial extent and interactions during the expansion are negligible, the TOF image closely reflects the momentum-space distribution of the original sample. This provides a reliable method for extracting the temperature of the gas. More specifically, for a thermal gas with temperature T undergoing ballistic expansion, the Gaussian width $\sigma(t)$ of the cloud after time t is given by:

$$\sigma(t)^2 = \sigma_0^2 + \langle v^2 \rangle t^2 = \sigma_0^2 + \frac{k_B T}{m} t^2 \tag{2.12}$$

Fitting the expansion of width over time allows extraction of the temperature of the atoms.

2.2.2 Optical pumping

Optical pumping is a widely used technique to prepare atoms in a specific internal state, often a *stretched state* which is the Zeeman sublevel with the maximal magnetic quantum number $m_F = \pm F$. This is achieved by illuminating the atoms with near-resonant light that is circularly polarized (σ^+ or σ^-), typically in the presence of a quantization magnetic field. The selection rules for electric dipole transitions guide the atoms through a series of absorption and spontaneous emission events, gradually transferring population into the

desired stretched state, which becomes a dark state that no longer couples to the optical field. This state preparation method is essential for experiments requiring high spin polarization, state initialization, or effective state-selective manipulation.

For Cs atoms, optical pumping to $|F = 3, m_F = 3\rangle$ can be done with a $3 \rightarrow 2'$ beam containing both σ^+ and π polarization components. In this configuration, $|F = 3, m_F = 3\rangle$ is the only dark state. Repumping from the other ground state $F = 4$ is necessary to keep the population at $F = 3$, and is usually done by setting the repumping beam frequency to $F = 4 \rightarrow F' = 4$ with the same polarization as the optical pumping beam.

2.3 Interaction with far-off-resonance light

2.3.1 Dynamical polarizability

In the regime of large detuning from atomic resonance, the scattering rate is greatly suppressed, and the primary effect of the atom-light interaction is to induce a conservative energy shift of the atomic state. This energy shift, known as the *AC Stark shift*, or *light shift*, is a fundamental concept in optical trapping and plays a central role in determining the shape and depth of the trapping potential.

The light shift depends on many factors, including the dynamical polarizability of the atomic state, and the intensity and polarization of the light field [68]. For atoms at a single hyperfine state $|nJF\rangle$, the light shift has the following form:

$$V_{Stark} = -\frac{1}{4}|E|^2 \left\{ \alpha^s_{nJF} - i\alpha^v_{nJF} \frac{[\mathbf{u}^* \times \mathbf{u}] \cdot \mathbf{F}}{2F} + \alpha^T_{nJF} \frac{3[(\mathbf{u}^* \cdot \mathbf{F})(\mathbf{u} \cdot \mathbf{F}) + (\mathbf{u} \cdot \mathbf{F})(\mathbf{u}^* \cdot \mathbf{F})] - 2\mathrm{F}^2}{2F(2F-1)} \right\} \quad (2.13)$$

Here E is the amplitude of electric field of the laser, $\mathbf{u}$ is a complex unit vector representing the polarization of the electric field, $\mathbf{F}$ is the total angular momentum operator $\mathbf{F} = \mathbf{I} + \mathbf{J}$,

and α^s_{nJF}, α^v_{nJF}, α^T_{nJF} are the scalar, vector and tensor polarizabilities of atomic state $|nJF\rangle$, which depend only on the wavelength of driving field.

From the expression, it is evident that the total light shift of an atomic energy state $|nJF\rangle$ comprises three distinct contributions. The first is the *scalar light shift* which is independent of the magnetic sub-level m_F and the polarization of the light field. The second is the *vector light shift* that depends on the polarization of the light field and varies linearly with m_F. The third is the *tensor light shift* which arises from the polarization anisotropy of the light field and depends quadratically on the m_F quantum number.

It is worth noting that the vector light shift manifests as an *effective* magnetic field, in the sense that, like the Zeeman shift induced by a real magnetic field, it produces an energy shift that is linear to the magnetic quantum number m_F. The strength of vector shift depends on the degree of circular polarization, characterized by the cross product $\mathbf{u}^* \times \mathbf{u}$. For a circularly polarized light (either right-handed or left-handed), this vector has a magnitude of 1. In contrast, for linearly polarized light, this cross product vanishes, resulting zero contribution from the vector shift.

For alkali atoms in the ground state, the tensor polarizability α^T vanishes. Additionally, if the applied light field is linearly polarized, the vector shift also vanishes. As a result, the total light shift reduces to a state-independent scalar shift that is simply proportional to local light intensity $\sim |E|^2$.

When laser light is red-detuned from an atomic transition ($\omega < \omega_0$), the resulting interaction is attractive, characterized by a positive scalar polarizability α^s, which draws atoms toward regions of highest local intensity where the potential energy is minimized. Conversely, for blue-detuned light ($\omega > \omega_0$), the interaction becomes repulsive, and atoms are confined near intensity minima. In the case of multi-level atomic systems, the total polarizability must be obtained by summing over the contributions from all relevant transition channels.

The dynamical polarizabilities calculated following methods in Ref. [68] at wavelengths

relevant to QMS experiments are listed in Tab. 2.1. Note that in the table, the unit of scalar polarizability α^s is chosen such that the scalar potential U can be conveniently calculated in the temperature unit $(k_B \cdot \mu\text{K})$ from laser intensity I using $U = -\alpha^s I$. The vector polarizability α^v is in the unit of $\text{mG}/(\text{W}/\text{mm}^2)$ such that the effective field from the vector shift can be calculated by $\mathbf{B}_{eff} = i\alpha^v[\mathbf{u}^* \times \mathbf{u}]I$ from laser intensity I and the polarization vector $\mathbf{u}$. Differential polarizability $\alpha_e^s - \alpha_g^s$ between ground state $6S_{1/2}$ and excited state $6P_{3/2}$ is presented in the unit of $h \cdot \text{MHz}/(\text{W}/\text{mm}^2)$. Those values will be used later to calculate the trapping potentials from laser beam parameters.

λ (nm)	α_g^s $(k_B \cdot \mu\text{K}/(\text{W}/\text{mm}^2))$	α_g^v $(\text{mG}/(\text{W}/\text{mm}^2))$	$\alpha_e^s - \alpha_g^s$ $(h \cdot \text{MHz}/(\text{W}/\text{mm}^2))$
532	-0.051	-0.017	0.0029
686*	-0.145	-0.131	0.0001
780	-0.383	-0.744	0.0087
935*	0.683	-2.743	0.0001
1064	0.258	-0.333	-0.0057

Table 2.1: Cs atoms ground state scalar polarizability α_g^s, vector polarizability α_g^v and differential polarizability $\alpha_e^s - \alpha_g^s$ for the D2 transition at different wavelengths. The $*$ sign denotes the magic wavelengths.

2.3.2 Magic wavelengths

The expression of light shift in Eqn. 2.13 describes the energy shift of a certain atomic state $|nJF\rangle$ in the presence of external light field. When considering the transition between two states $|nJF\rangle$ and $|n'J'F'\rangle$, any difference in their respective polarizabilities will lead to a differential light shift that modifies the transition frequency. Such effect has been exploited in QGM experiments where tightly focused light field are used to selectively offset energy levels of atoms at certain lattice sites [69]. However, in many other contexts, such differential light shifts can have detrimental impacts on cooling and imaging processes, requiring specialized techniques to mitigate their effects [70]. Common strategies include the

use of *magic-wavelength* trapping, where the polarizabilities of the relevant atomic states are matched ($\alpha_g(\omega) = \alpha_e(\omega)$) to eliminate the differential light shift that depends on local intensity.

For Cs atoms D2 transition, if considering only the scalar polarizability, such magic conditions are met at two wavelengths: one is near 686 nm (blue-detuned) and the other one is around 935 nm (red-detuned), as shown in Fig. 2.1. The polarizabilities around 532 nm and 1064 nm are shown in Fig. 2.2.

In the QMS experiment, we are using a laser at the red-detuned magic wavelength 935nm to form the 2D optical lattice. Magic-wavelength trapping mitigates differential light shifts across the atomic cloud, allowing the optical pumping light to maintain a uniform detuning throughout the sample.

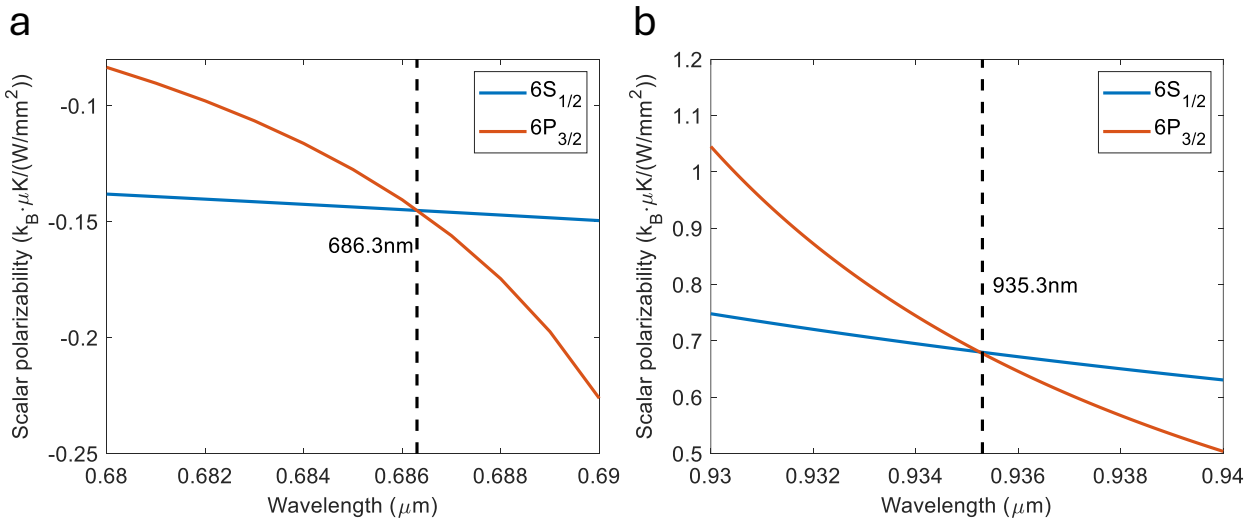

Figure 2.1: Magic wavelengths for Cs D2 transition. The scalar polarizabilities of the ground state $6S_{1/2}$ (blue) and the excited state $6P_{3/2}$ (orange) of the D2 transition are shown in the plot. a. Blue-detuned magic wavelength at 686.3 nm. b. Red-detuned magic wavelengt at 935.3 nm. Plots are reproduced based on data in Ref. [68].

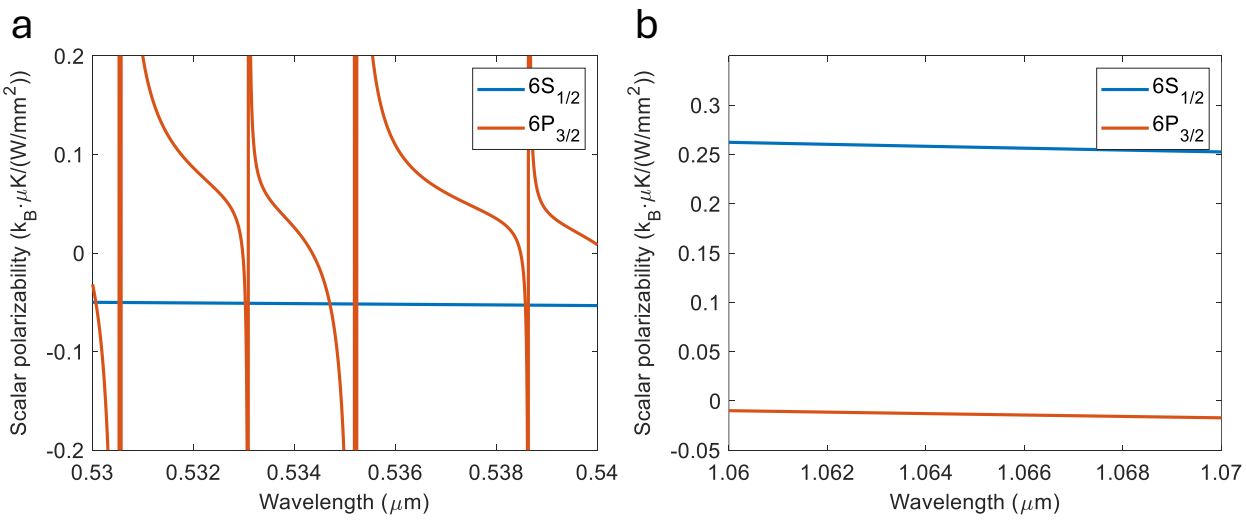

Figure 2.2: Scalar polarizabilities at 532 nm and 1064 nm. The scalar polarizabilities of the ground state $6S_{1/2}$ (blue) and the excited state $6P_{3/2}$ (orange) of the D2 transition are shown in the plot for wavelength range (a) 530 nm to 540 nm and (b) 1060 nm to 1070 nm. Note that there are a few transitions from excited state $6P_{3/2}$ to $14D_{3/2}$ and $14D_{5/2}$ (∼530 nm), $15S_{1/2}$ (∼533 nm), $13D_{3/2}$ and $13D_{5/2}$ (∼535 nm), $14S_{1/2}$ (∼538 nm). Plots are reproduced based on data in Ref. [68]

2.3.3 Optical dipole trap

Optical tweezers are often created as arrays of tightly focused, red-detuned dipole traps where atoms are confined at the intensity maxima. For a dipole trap formed by a single laser beam, the trapping potential can be modeled directly from the beam's intensity profile. For a Gaussian beam propagating along z direction, the intensity distribution follows [71]

$$I(r,z) = I_0 \left(\frac{w_0}{w(z)}\right)^2 \exp\left(\frac{-2r^2}{w(z)^2}\right) \tag{2.14}$$

Here $w(z)$ denotes the beam size and w_0 is the beam waist. At any given location z, the beam intensity profile is a circular Gaussian with a $1/e^2$ radius of $w(z)$. The beam size evolves with z by

$$w(z) = w_0\sqrt{1+\left(\frac{z}{z_R}\right)^2} \tag{2.15}$$

where $z_R = \pi w_0^2/\lambda$ is the Rayleigh range. The peak intensity I_0 can be calculated from the total power P and beam waist w_0 by

$$I_0 = \frac{2P}{\pi w_0^2} \tag{2.16}$$

More generally, for an elliptical Gaussian beam with beam waist w_{x0} and w_{y0} along x and y direction respectively, the intensity distribution is

$$I(x,y,z) = I_0 \left(\frac{w_{x0}}{w_x(z)}\right)\left(\frac{w_{y0}}{w_y(z)}\right) \exp\left[-2\left(\frac{x^2}{w_x(z)^2} + \frac{y^2}{w_y(z)^2}\right)\right] \tag{2.17}$$

Here $w_x(z)$ and $w_y(z)$ follow the Eqn. 2.15 with their corresponding waists w_{x0} and w_{y0}. The peak intensity can be derived from the total power P by

$$I_0 = \frac{P}{\pi w_{x0} w_{y0}} \tag{2.18}$$

Trap depth

If we use an elliptical Gaussian beam with the following parameters to form a dipole trap: wavelength λ, beam waist of w_{x0} and w_{y0} in x and y direction, total power P, the potential geometry for ground state atoms is

$$U(x,y,z) = -\alpha I(x,y,z) \tag{2.19}$$

Here α is the ground state polarizability. If we define *trap depth* as the depth of the confining potential in energy unit, since the intensity goes to zero at infinity, the trap depth of such dipole trap is simply $U_0 = \alpha I_0$.

Trap frequency

Another important parameter of the trapping potential is the *trap frequency*, which is the characteristic oscillation frequency of the atoms confined in the bottom of the trap. The trap frequency along a certain axis can be directly obtained from the curvature of the potential

$$\nu_i = \sqrt{\frac{1}{m}\frac{\partial^2 U}{\partial x_i^2}} \tag{2.20}$$

For a dipole trap with intensity described by Eqn. 2.17, the trap frequencies in the x and y directions are

$$\nu_x = \sqrt{\frac{4U_0}{mw_{x0}^2}} \tag{2.21}$$

$$\nu_y = \sqrt{\frac{4U_0}{mw_{y0}^2}} \tag{2.22}$$

Note that in axial direction z, the intensity profile is not Gaussian and the trap frequency is related to the Rayleigh range in x and y direction

$$\nu_z = \sqrt{\frac{U_0}{m}\left(\frac{1}{z_{Rx}^2} + \frac{1}{z_{Ry}^2}\right)} \tag{2.23}$$

Typically the beam waist is much larger than the optical wavelength, resulting in $z_R \gg w_0$. In this regime, the axial confinement is much weaker than the radial confinement, leading to the smallest trap frequency along the axial direction.

The trap frequency can be measured experimentally by modulating the intensity of the laser that generates the confining potential. When the modulation frequency matches twice the trap frequency, the atoms experience parametric resonance and are resonantly heated. By measuring the atomic temperature after a period of heating as a function of the modulation frequency, one can locate the resonance peak and thereby determine the trap frequency. Multiple resonance features may appear in such measurements, and knowledge of the ex-

pected trap geometry is essential to correctly identify the trap frequencies along different spatial axes.

Lamb-Dicke parameter

When atoms are confined near the bottom of the trapping potential, their motional dynamics can be approximated by that of a quantum harmonic oscillator, with the energy spacing between adjacent motional states determined by the trap frequency ν. The spatial extent of atomic wavefunction in the nth motional state can be estimated as $\sqrt{2n+1}x_0$ where $x_0 = \sqrt{\hbar/m\nu}$ defines the natural length scale of the oscillator and m is the atomic mass. When a trapped atom is tightly confined such that the spatial extent of its wavefunction is much smaller than the transition wavelength, transitions that change the motional quantum number are strongly suppressed. This regime is known as *Lamb-Dicke regime*, and is typically characterized by the condition

$$\eta^2(2n+1) \ll 1 \tag{2.24}$$

Where η is the *Lamb-Dicke parameter*, defined as

$$\eta = kx_0 = k\sqrt{\hbar/m\nu} \tag{2.25}$$

with $k = 2\pi/\lambda$ being the wavenumber of the transition wavelength.

When atoms are outside the Lamb-Dicke regime, photon scattering can readily change the motional state of the atom, thereby reducing the fidelity of state control during cooling cycles. Although techniques have been developed to address higher-order sidebands, enabling motional ground-state cooling even outside the Lamb-Dicke regime [72], in most cases, achieving tight confinement with high trap frequencies remains essential for realizing efficient cooling and maintaining precise control over atomic motional states. As an example, for a transition wavlength of 852 nm and a trap frequency of 75 kHz, the Lamb-Dicke

parameter is $\eta = 0.24$. To remain within the Lamb-Dicke regime, the motional quantum number should be kept below 3 to ensure that recoil-induced transitions to higher states remain suppressed.

2.3.4 Optical lattice

The interference of laser beams creates a periodic intensity landscape known as an optical lattice. To model the optical lattice potential, one begins by considering the electric fields of the individual laser beams and summing them coherently to obtain the total electric field. The resulting intensity profile is then calculated as the square of the total field amplitude, which determines the spatial structure of the trapping potential experienced by the atoms.

1D lattice

One simplest example is the 1D lattice formed by retro-reflecting one laser beam propagating along the x direction. Assuming the incoming beam has an intensity I and an electric field given by the real part of $\mathbf{E}\, e^{ikx}$, and that the reflection beam has an electric field amplitude reduced by a factor of R, the total electric field is $\mathbf{E}_{tot} = \mathbf{E}\, e^{ikx} + R\, \mathbf{E}\, e^{-ikx}$. The resulting intensity is $I_{tot} \sim |\mathbf{E}_{tot}|^2 = |\mathbf{E}|^2 \cdot (1 + R^2 + 2R\cos(2kx))$ which has an interference term with a periodicity of half the incident beam wavelength.

If we assume the incident beam is a circular Gaussian beam (wavelength λ, power P, beam waist w_0) and the reflected beam has the same beam parameter as the incident beam with an reduced amplitude factor R, the trap depth U_{lat} and axial trap frequency ν_{lat} of the resulting 1D lattice can be estimated with the following expressions

$$U_{lat} = \alpha \cdot 4R \cdot \frac{2P}{\pi w_0^2} \tag{2.26}$$

$$\nu_{lat} = \frac{2\pi}{\lambda}\sqrt{\frac{4U_{lat}}{m}} \tag{2.27}$$

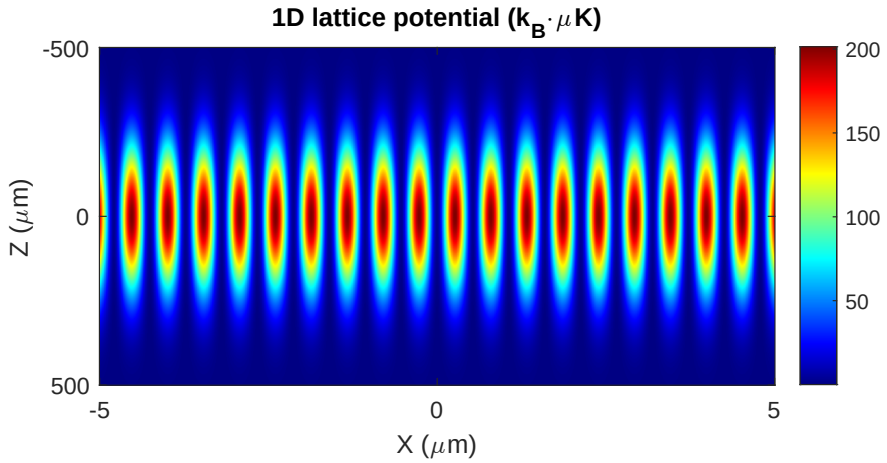

Figure 2.3: 1D lattice potential created by retro-reflecting a Gaussian beam propagating along x direction with a beam waist of 300μm and a power of 35 W at 1064 nm, assuming reflection beam has 60% of incident beam power. The resulting trap depth is about 200 $k_B \cdot \mu$K, and axial trap frequency is 145 kHz. Beams with a similar set of parameters are used for the 1D transport lattice in the QMS experiment.

An example plot of 1D lattice potential for ground state Cs atoms with the beam parameters of the transport lattice used in QMS experiment is shown in Fig. 2.3.

To accurately model the lattice potential, it is necessary to consider not only the intensity profile but also the polarization landscape of the interference pattern, especially at wavelengths where the vector polarizability is significant. In the case of a one-dimensional lattice, if the incident and reflected beams have different polarizations, the resulting intensity interference is weakened due to the reduced polarization overlap, characterized by $\mathbf{E}_{\text{incident}} \cdot \mathbf{E}_{\text{reflected}}$. Additionally, the spatial variation in the relative phase between the two fields leads to a spatially varying polarization, creating a polarization gradient across the lattice. In the case of lin $\perp$ lin configuration where the two beams have orthogonal linear polarization $\mathbf{E}_{\text{incident}} \cdot \mathbf{E}_{\text{reflected}} = 0$, the resulting intensity distribution is uniform, but the local polarization varies spatially across the lattice. Such polarization gradient will introduce a spatially varying light shift that depends on the magnetic sublevel of atoms (see Eqn. 2.13), which is an important mechanism for many sub-Doppler cooling schemes, including optical molasses [73, 74] and degenerate Raman-sideband cooling (dRSC) [75, 76].

The same analysis can be generalized to more complex cases, where the spatial configuration and polarization of the interfering beams are engineered to create optical lattices with different intensity or polarization geometries. For example, a bow-tie lattice with a square geometry [58], or a triangular lattice formed by three interfering beams [33, 34]. Moreover, if the two interfering light fields have different frequencies, the resulting interference pattern will oscillate at the beatnote frequency. If this oscillation occurs on a timescale much faster than the characteristic timescales of atomic dynamics, the interference will effectively average out. In this case, the optical potentials generated by each field can be treated as adding incoherently. By coherently or incoherently superimposing one light field onto another, more exotic lattice geometries can be realized [77].

Simulation of 2D lattice potentials in the QMS experiments

In the QMS experiment, the 2D optical lattice for dRSC is formed by intersecting three symmetrically arranged beams at the origin with a polar angle of 45°. The beams have a wavelength of 935 nm which is the magic wavelength to Cs D2 transition. By adjusting the polarization configurations of the lattice beams, different intensity and polarization geometries can be realized through the resulting interference pattern. Here we summarize the simulation of the lattice potential with three different polarization configurations.

If all three beams are linearly polarized with their polarization vectors confined to the horizontal plane, the resulting interference pattern exhibits intensity maxima arranged in a honeycomb lattice, as shown in Fig. 2.4. The interference pattern also exhibits spatially varying polarization across the lattice, with the strongest effective magnetic field amplitude appearing at the trap centers. The effective magnetic field points along the $+z$ direction at half of the lattice sites and along the $-z$ direction at the other half. Each subset of sites forms a triangular lattice structure. While such a lattice geometry may be of interest for simulating exotic spin models, it is not ideal for imaging with dRSC. The potential near the trap centers

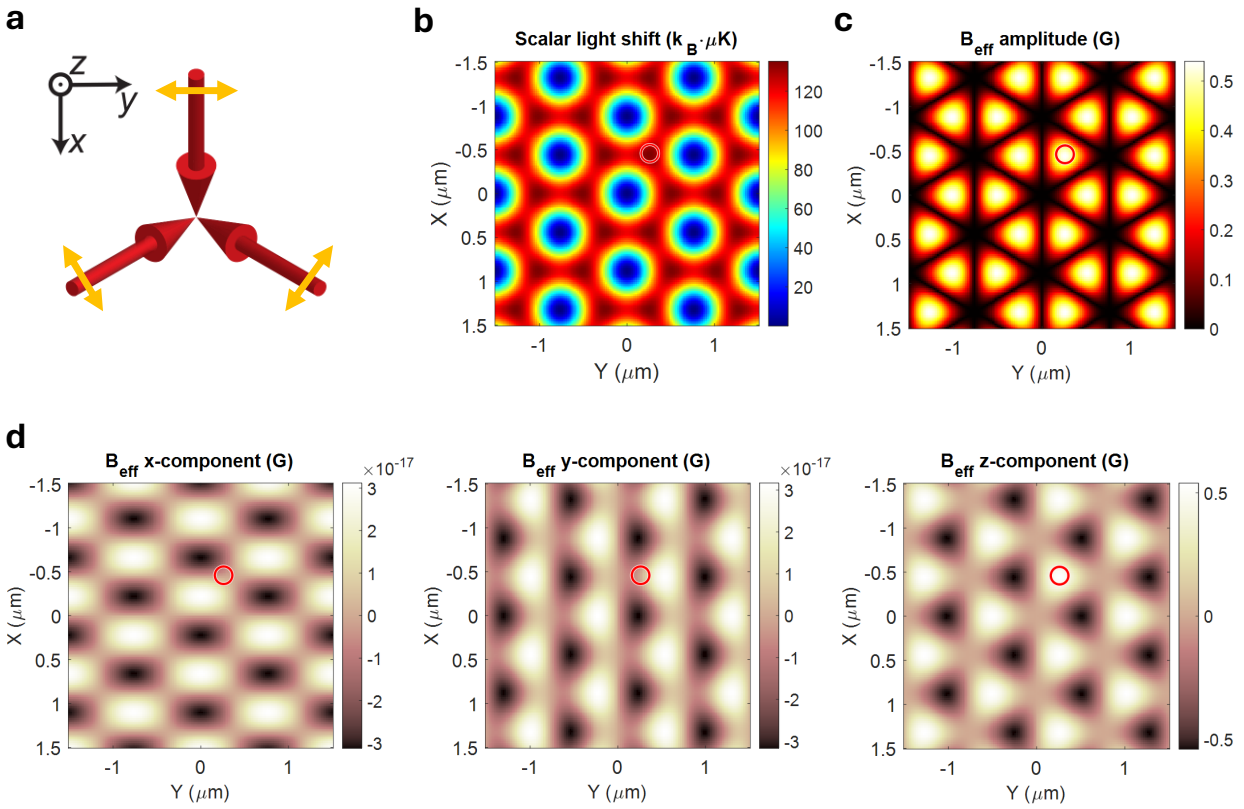

Figure 2.4: 2D lattice potential created by intersecting three lattice beams with linear polarization on the xy-plane. The beams are at wavelength of 935nm, each has a power of 200 mW and beam size of 64μm at the intersection point. Red circle has a radius of 0.1 μm and highlights the position of a site center. The resulting trap depth is about $13k_B \cdot \mu$K, and trap frequency is 48kHz. a. The geometry of the directions (red) and polarizations (yellow) of the three beams. b. The ground state scalar light shift in the lattice. Atoms are trapped at the high light shift area (dark red). c. The amplitude of effective B field in the lattice. d. The x, y, z components of the effective B field in the lattice. Note that the x and y component field is very small compared to z component and may be related to numerical errors in the simulation.

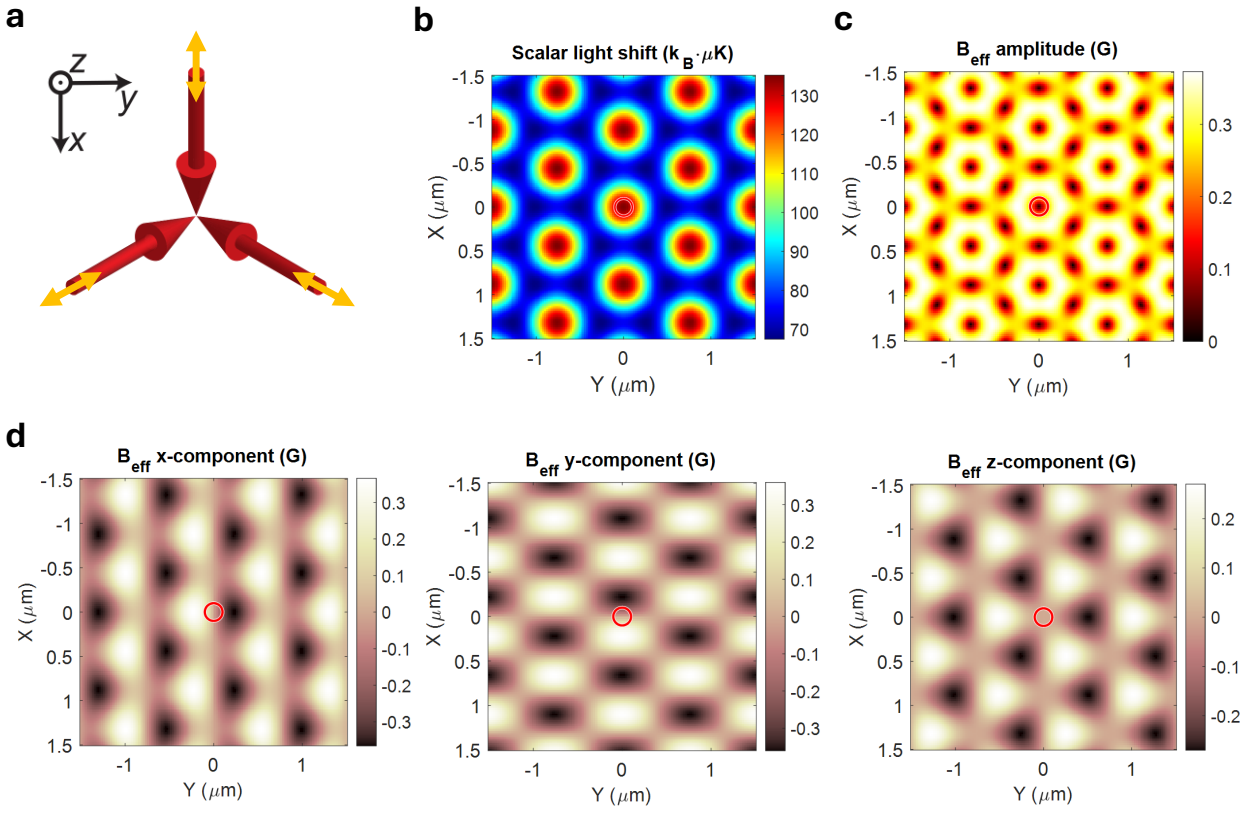

Figure 2.5: 2D lattice potential created by intersecting three lattice beams with linear polarization maximally vertical to xy-plane. The beams are at wavelength of 935nm, each has a power of 200 mW and beam size of 64μm at the intersection point. Red circle has a radius of 0.1 μm and highlights the position of a site center. The resulting trap depth is about $60k_B \cdot \mu$K, and trap frequency is 48kHz. a. The geometry of the directions (red) and polarizations (yellow) of the three beams. b. The ground state scalar light shift in the lattice. Atoms are trapped at the high light shift area (dark red). c. The amplitude of effective B field in the lattice. d. The x, y, z components of the effective B field in the lattice.

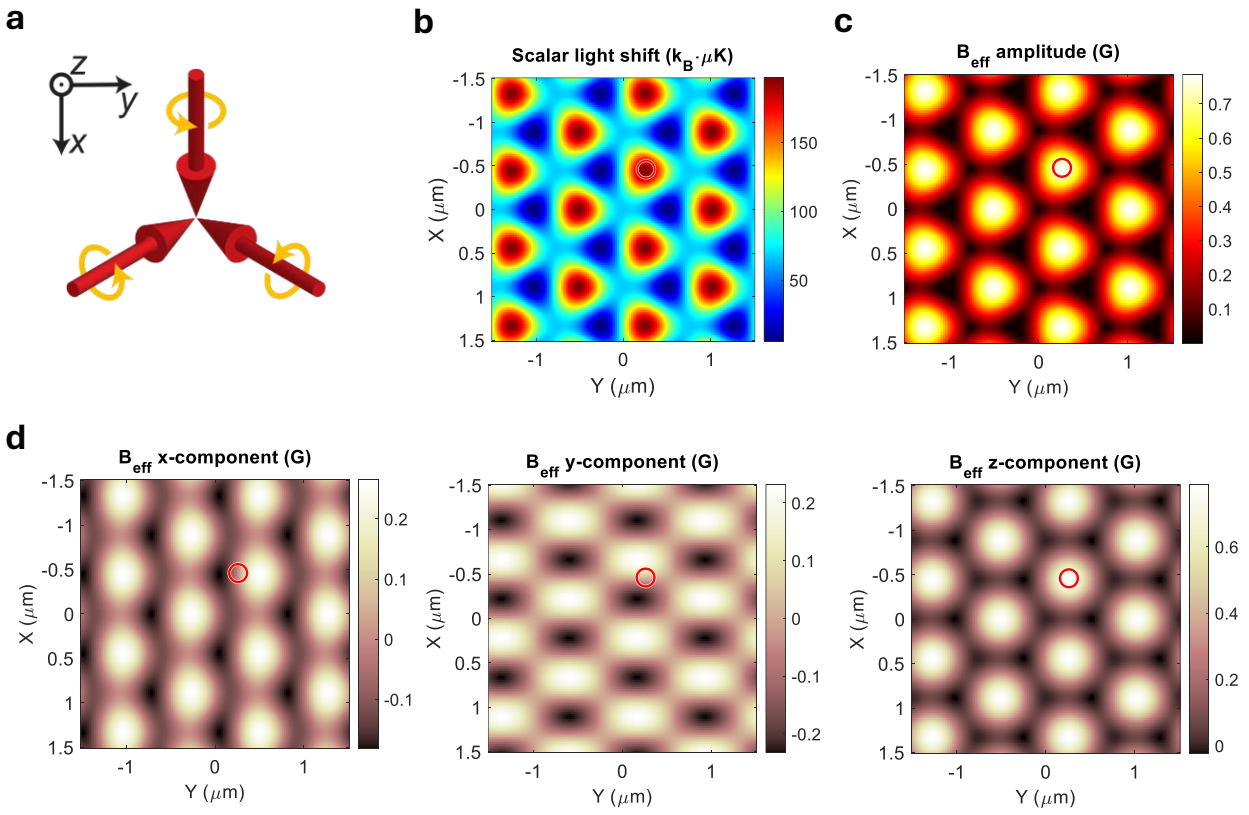

Figure 2.6: 2D lattice potential created by intersecting three lattice beams with circular polarization. The beams are at wavelength of 935 nm, each has a power of 200 mW and beam size of 64μm at the intersection point. Red circle has a radius of 0.1 μm and highlights the position of a site center. The resulting trap depth is about $130 k_B \cdot \mu$K, and trap frequency is 75 kHz. a. The geometry of the directions (red) and polarizations (yellow) of the three beams. b. The ground state scalar light shift in the lattice. Atoms are trapped at the high light shift area (dark red). c. The amplitude of effective B field in the lattice. d. The x, y, z components of the effective B field in the lattice.

is highly anharmonic, the connections between adjacent sites in the honeycomb structure are very shallow, and the presence of a large effective magnetic field with alternating directions further complicates efficient sideband cooling.

If all three beams are linearly polarized with their polarization vectors maximally vertical to the horizontal plane, the resulting interference pattern exhibits intensity maxima arranged in a triangular lattice, as shown in Fig. 2.5. Note that even at the minima, the scalar light shift remains nonzero. This arises from the fact that there is no spatial location where the polarization vectors of all contributing beams perfectly cancel, resulting in a residual intensity and thus a non-vanishing scalar shift. This lattice configuration was used during the early stages of the experiment; however, we were unable to achieve efficient cooling of atoms in this lattice for site-resolved imaging. The challenges are two-fold: first, the limited contrast of the scalar potential reduces the trap frequencies, making sideband less resolvable; second, although the effective magnetic field amplitude vanishes at the trap centers, it rapidly changes in both amplitude and direction over distances of just a few tens of nanometers, comparable to the extent of the atomic wavefunction, thereby introducing significant inhomogeneities that complicates cooling.

The polarization configuration that we finally adopt in the experiment is shown in Fig. 2.6. In this configuration, all three beams are circularly polarized with the same handedness, and the resulting interference pattern exhibits intensity maxima arranged in a triangular lattice. Due to the high polarization overlap between the beams, the trap depth is greater than in the previous two polarization configurations. Near the trap centers, the local polarization remains predominantly circular, resulting in a large and spatially smooth effective magnetic field oriented primarily along the z-axis. The amplitude of this effective field can be compensated by applying an external bias field in the opposite direction. The residual spatial gradient of the effective field then provides the coupling between the atomic spin and motional degrees of freedom, which is essential for efficient dRSC. The cooling and imaging

scheme and its performance will be discussed in detail in a later chapter.

Comments on the current 2D lattice configuration

Although we have achieved site-resolved imaging in the current circularly polarized lattice configuration, as detailed in later chapters, two notable drawbacks remain, namely:

- Presence of a large effective magnetic field in the z direction. Although an external offset field can be applied to compensate for the effective field at the center of the lattice, it cannot fully account for the spatial variation and leaves a significant residual field at the edges of the atomic cloud. This spatially varying field orientation complicates the polarization environment, making it difficult to eliminate unwanted σ^- components in the optical pumping beam and thereby compromising the overall cooling efficiency.

- No independent control of Raman coupling from trapping. The lattice simultaneously serves two purposes: providing confinement and inducing Raman coupling that entangles the spin and motional degrees of freedom. As a result, the Raman coupling cannot be independently tuned, which can be inconvenient in experiments where such spin-motion coupling is undesirable.

A future upgrade will involve implementing a cooling mechanism that does not rely on the trapping lattice to provide Raman coupling, for example, electromagnetically induced transparency (EIT) cooling [43] or non-degenerate Raman-sideband cooling [72, 78, 79]. In addition, the lattice configuration could be modified to a linear polarization scheme to avoid the effective magnetic field at trap centers, for example, as the configuration described in Ref. [80]. Alternatively, it is also possible to set up a separate linearly polarized "science" lattice that provides a simple scalar potential, and use the circular lattice only for imaging, similar to Ref. [81].

CHAPTER 3

OVERVIEW OF THE SYSTEM

The main experimental apparatus consists of three primary sub-systems: the vacuum system, the laser and optical system, and control of microwave and magnetic fields. The ultrahigh vacuum (UHV) environment is essential for maintaining sufficiently low background pressure, thereby minimizing collisions between laser-cooled atoms (typically below 1 mK) and room-temperature background gas, which is essential to obtain long lifetime of the trapped atoms. The laser system serves as the principal tool for manipulating and probing the atoms, enabling cooling, trapping, state preparation, and detection. The magnetic field control provides precisely tunable fields for Zeeman slowing, magneto-optical trapping, and access to Feshbach resonance.

In the following sections, we will give a brief overview of the system's hardware and control software architecture. A more comprehensive description should be found in Ref. [82].

3.1 Vacuum system

The vacuum system consists of four regions: the Cs oven, Zeeman slower, **stainless steel chamber** (also referred as **main chamber**) and **glass cell**. The Cs oven is heated to about 70°C to provide hot Cs vapor, which is subsequently slowed by Zeeman slower and captured by a Magneto-Optocal Trap (MOT) in the stainless steel chamber. After initial pre-cooling in the stainless steel chamber, the atoms are transported to a glass cell through a vacuum tee. On the glass cell side, a dedicated three-layer platform is used to stably mount two high-NA objectives, positioned above and below the glass cell to enable high-resolution imaging and addressing. In addition to site-resolved imaging in the glass cell, atoms can also be imaged in both the stainless steel chamber and the glass cell using a side-view CCD for low-resolution

absorption imaging.

The vacuum system is mechanically separated from the stable mounting structure for microscopes. The early stage of experiments were performed in the main chamber [83]. In the middle of 2019, we installed the glass cell to the main chamber. Shortly after resuming vacuum performance, we translated the entire vacuum system to insert the glass cell in between the two microscopes, as illustrated in Fig. 3.2. It is possible to re-separate the two systems for upgrades if necessary.

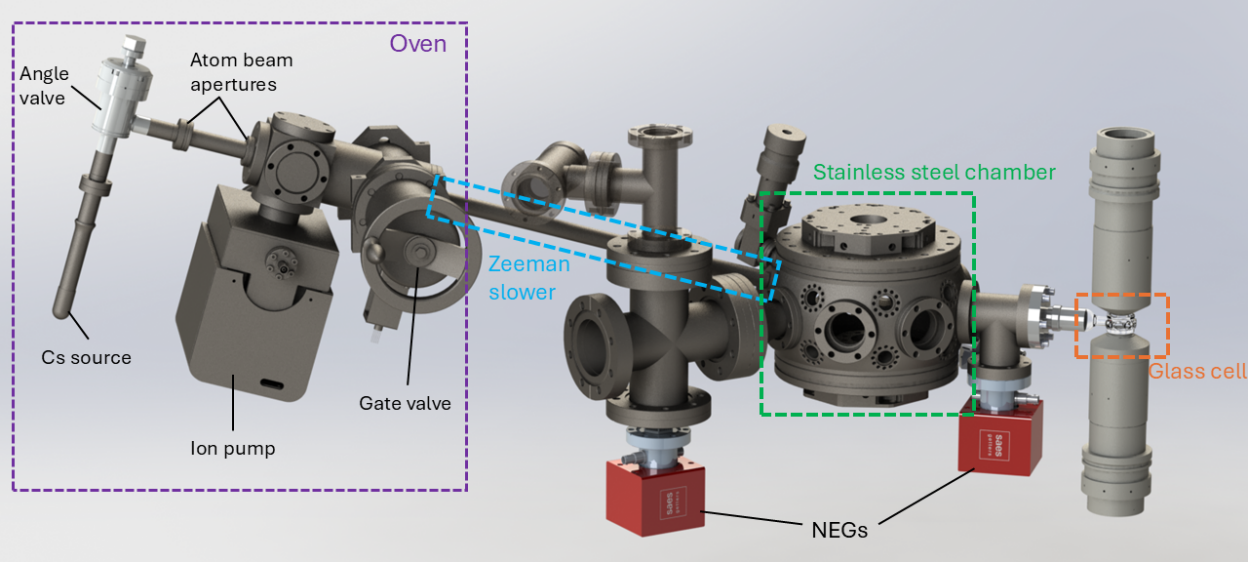

Figure 3.1: Overview of the vacuum system. Figure is modified from Ref. [82].

3.2 Lasers

3.2.1 Near-resonance diode lasers

In our experiment, we employ six frequency-stabilized diode lasers operating near 852 nm, corresponding to the cesium D2 line. These lasers are organized into two groups: "Stanford" (1st generation) and "Photodigm" (2nd generation) with each group containing three diode lasers. To ensure optimal frequency and intensity stability, lasers of the same group are enclosed by an acylic box housed in the quiet room and are coupled to the main experimental

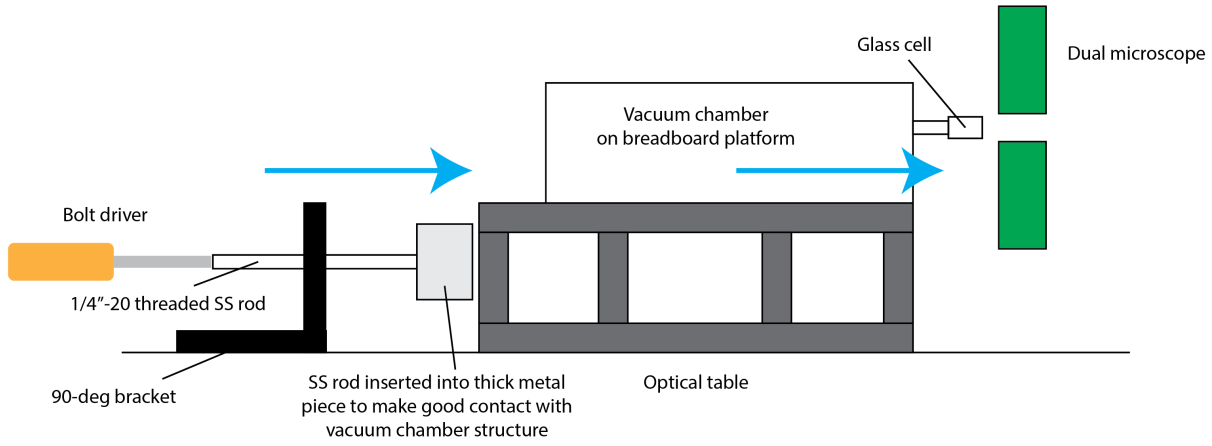

Figure 3.2: Illustration of setup to move glass cell to the middle of two microscopes by translating the entire vacuum system.

setup via optical fibers. The fiber outputs are subsequently directed to the appropriate viewports of the chamber or windows of the glass cell depending on their designated function.

First letter	2nd-4th letters	Usage
S: Stanford	**REF**	Reference laser locked to $4 \rightarrow 5'$ transition
	MOT	Beat-note locked to REF to access $4 \rightarrow F'$
	REP	Beat-note locked to REF to access $3 \rightarrow F'$
P: Photodigm	**REF**	Reference laser locked to $3 \rightarrow 2'$ transition
	MOT	Beat-note locked to REF to access $4 \rightarrow F'$
	REP	Beat-note locked to REF to access $3 \rightarrow F'$

Table 3.1: Diode lasers and their naming conventions. We use a four-letter code to name each diode laser. One example is **PMOT**, which represents **P**hotodigm **MOT** laser that is located in Photodigm box and locked to $F = 4$ to F' transitions. The naming convention is commonly adopted in the channel labels used for analog control of the laser frequency via beat-note locks.

The detailed frequency locking scheme is described in Ref. [82], and the naming convention for the diode lasers are detailed in Tab. 3.1. Briefly, each group consists of a reference (REF) laser locked to a specific cesium transition with polarization spectroscopy, a MOT laser locked to the $F = 4$ to F' transition, and a REP laser locked to the $F = 3$ to F' transition. The REF laser is dedicated solely to frequency locking and does not offer computer-controlled frequency tuning. In contrast, the MOT and REP lasers with frequency

f are locked by first generating a beat note with the REF laser, which has a frequency of $f_{beat} = |f - f_{REF}|$. A phase-locked loop (PLL) is then used to lock the beat frequency to a voltage-controlled oscillator (VCO), whose frequency can be dynamically adjusted by the computer. If the beat frequency is around 9 GHz (when the laser is locked to a different ground state than the REF), it is first mixed with a microwave source at frequency $f_0 =$ 9.18 GHz to down-convert the signal to a lower frequency $|f_{beat} - f_0|$, which is then fed into the PLL. This scheme enables precise and programmable control of the MOT and REP laser frequencies during an experimental sequence.

First letter	Second letter	Third letter
G : Glass cell	**I**: Imaging	**P**: Pumping
M : Main chamber	**C**: Cooling	**R**: Repumping

Table 3.2: Beam path naminig conventions. We use a three-letter code to name each beam path. One example path name is **GCP**, which represents **G**lass cell **C**ooling **P**umping. The naming conventions are commonly adopted in the channel labels used for analog control of the beam intensity via AOM attenuators, as well as digital control of the AOM RF switch and beam shutter state.

Each MOT and REP laser serves multiple beam paths, which are frequency-shifted and amplitude-modulated using acousto-optic modulators (AOMs) and then coupled into optical fibers. We assign an unique name to each beam path. For some of the paths that are used for imaging and dRSC, the naming follows the convention in Tab. 3.2. The usage and accessible transitions of each path is listed in Tab. 3.3. Note that for beam paths derived from the same laser, the frequency differences are set by the AOMs and therefore cannot be independently tuned.

Most near-resonant beam paths operate at low power (<10 mW out of the fibers), with the exception of the paths for Magneto-Optical Trapping (MOT) and Zeeman slowing (ZS), which require higher power. These higher-power beams are derived from the output of a tapered amplifier (TA) seeded by a combined beam from both the MOT laser and REP laser.

Laser name	Path name	Accessible frequency from transition (MHz)	Usage
SMOT	MOT	($f_{4\to5'}$): -208 to +187	MOT
	ZS	($f_{4\to5'}$): -295 to +100	Zeeman slowing
	MCR	($f_{4\to5'}$): -379 to +16	Main chamber dRSC repumper
	MIP/GIP	($f_{4\to5'}$): -129 to +266	Main chamber imaging repumper
SREP	MOT	($f_{3\to2'}$): +147 to +542	MOT repumper
	ZS	($f_{3\to2'}$): +60 to +455	Zeeman slowing repumper
	MCP	($f_{3\to2'}$): -99 to +295	Main chamber dRSC
	GCP	($f_{3\to2'}$): -125 to +269	Glass cell dRSC
PMOT	GCR	($f_{4\to5'}$): -425 to +45	Glass cell dRSC repumper
PREP	GIR	($f_{3\to4'}$): -340 to +2	Glass cell imaging repumper
	MIR	($f_{3\to4'}$): -340 to +2	Main chamber imaging repumper

Table 3.3: List of near-resonance beam paths

3.2.2 High-power far-off-resonance lasers

We operate four major high-power lasers: MOPA (Coherent, Mephisto MOPA), TiSapph (M Squared, SolsTis), Vexlum (Vexlum, VALO SF) and Sprout (Lighthouse Photonics, Sprout-Solo). These high-power lasers are all far-off-resonance and are used to create optical trapping potentials. A list of the high-power lasers is provided in Tab. 3.4.

Laser name	Wavelength	Output power	Usage
MOPA	1064 nm	55 W	1D transport lattice (free space, 30 W) Glass cell light sheet (fiber-coupled, 5 W)
TiSapph*	700 - 1000 nm	2 - 4 W	Glass cell 2D lattice (fiber-coupled)
Vexlum	935 nm	4.3 W	Glass cell 2D lattice (fiber-coupled)
Sprout	532 nm	8 W	Glass cell optical tweezers (free space)

Table 3.4: List of high-power far-off-resonance lasers. *We have noticed a constant output power degradation at 935 nm and replaced it with Vexlum in early 2025.

3.3 Microwave and magnetic fields

In this section we focus on the recent modifications on microwave and magnetic field controls hardwares.

Zeeman slower current driver

In early 2024 we had to replace the old Zeeman slower current driver. In the new setup, the Zeeman slower coils are connected directly to two Tenma power supplies that are running at constant current mode. The Zeeman slower has four sections: front, bias, tapered, end. In the actual setup we are only driving current to the front and tapered sections, with 1.8A and 2.2A current respectively.

Microwave sources

We have two microwave sources that are operating around Cs clock transition of approximately 9.192 GHz. Both of them are referenced to a 10 MHz frequency standard that is synchronized to GPS signal and shared across multiple laboratories within the Chin group.

The first microwave source (CTI XPDRO-9315) is located on the upper shelf above the Stanford laser box and is operating at a fixed frequency of 9.18 GHz. The purpose of it is to down-convert the beat frequency for laser frequency locking.

The second microwave source is Windfreak SynthHD, which is controlled via a USB connection to the main experiment control computer (LabPC1). It has a LabVIEW interface allowing the output frequency to be scanned continuously during experimental runs. Windfreak is used for microwave spectroscopy in both the stainless steel chamber and glass cell to calibrate the magnetic field control. In the current setup, the microwave on/off is controlled via an RF switch, and the signal is subsequently split, amplified, and delivered to two microwave horns positioned near the stainless steel chamber and the glass cell.

3.4 Experiment control software

There are two computers for QMS experiments: LabPC1 and LabPC2. LabPC1 hosts the main LabVIEW-based experiment control program, along with a separate LabVIEW-based

image analysis program. LabPC2 hosts a newly developed MATLAB-based image analysis program. Currently, there is no active synchronization between the LabVIEW control program and the two image analysis programs (LabVIEW and MATLAB). Once started, the image analysis programs continuously monitor and retrieve data from the cameras. Since the camera exposure is externally triggered by the control program, image data only becomes available after the exposure and readout processes, thereby enabling a form of passive synchronization between the control and image analysis systems.

In addition to performing live analysis of the images, both image analysis programs (LabVIEW and MATLAB) support saving the acquired raw image data to files for subsequent post-processing and analysis.

3.4.1 LabPC1: LabVIEW control and analysis program

The experimental sequence is controlled using a main control program hosted on LabPC1. The overall workflow is illustrated in Fig. 3.3. Basically, the LabVIEW control program compiles a series of instructions specifying the timing and output voltages for different channels and sends these instructions to a custom-built bus system that manages the voltage outputs to the experimental hardware. On the data acquisition side, the image analysis program retrieves image data from the cameras and configures the camera settings as needed. The program can also be configured to save raw images for a pre-defined number of acquisitions in CSV format.

The LabVIEW-based image analysis program is specifically designed for absorption imaging in the stainless steel chamber and the glass cell with two Pixelfly CCD cameras. Only one camera can be selected at a time for image acquisition. However, since absorption imaging is inherently destructive and causes atoms to heat up and leave the traps after the imaging pulse, controlling a single camera per experimental run is sufficient for the intended measurements.

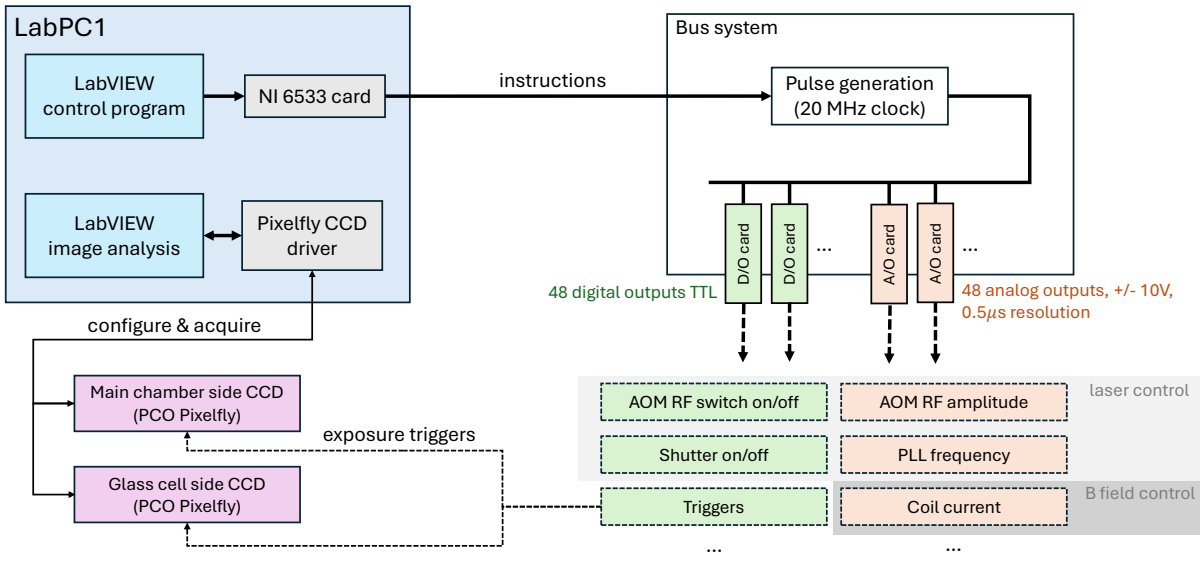

Figure 3.3: Diagram of experiment control and image analysis programs on LabPC1. Bus system diagram is modified from Ref. [82].

3.4.2 LabPC2: MATLAB App for control and analysis

For images taken through the high-NA objectives, the acquisition and live analysis is performed using a newly developed MATLAB-based image analysis program on LabPC2, referred to as "MATLAB App", which is capable of controlling and acquiring from multiple devices and performing more intensive live analysis on the high resolution images.

The MATLAB App features a modular, object-oriented design. Device control is managed through a dedicated class, `CameraManager`, which serves as an interface between the app and different types of devices. The general structure for device control is shown in Fig. 3.4. Other modules include `LayoutManager`, which manages the updates to the front panel plots; `DataStorage`, which supports the storage and export of raw data as MAT file; and `Analyzer` and `LiveData`, which perform live analysis on the images immediately after each acquisition. For designing a sequence, it includes a `AcquisitionConfig` that defines a list of operations to be executed in sequential order as a `SequenceTable`. Typical operations include initiating image acquisition on a camera, reading out acquired images, projecting specified patterns

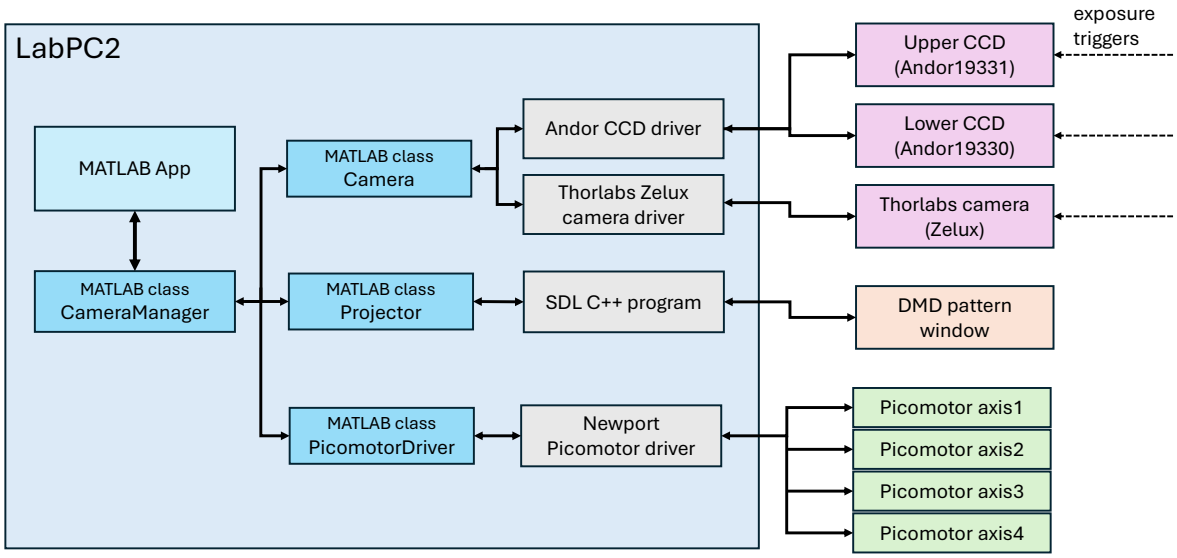

Figure 3.4: Diagram of device control and image analysis program (MATLAB App) on LabPC2. The MATLAB App manages the devices through a class `CameraManager`, which interacts with three classes `Camera`, `Projector` and `PicomotorDriver` to control external devices. Three imaging cameras (Andor19330, Andor19331, Zelux) are under `Camera` class, with each device controlled through its corresponding driver for configuring camera settings and acquiring raw data. All three cameras can be configured to accept external triggers generated from the LabVIEW control program on LabPC1. DMD is under the `Projector` class and the displayed pattern is controlled via a low-level C++ program developed with an open source library SDL [84]. Additionally, the `CameraManager` also has access to `PicomotorDriver` that drives four Newport 8301NF piezo actuators for precision positioning of upper objective and light sheet trapping potential.

onto the DMD, and performing real-time analysis on collected data. People can also create pre-defined sequences with certain label under `SequenceRegistry` class. An example of a pre-defined sequence table is shown in Fig. 3.5. Another important module is `Analyzer`, which is designed for analysis of live images. The `Analyzer` will invoke functions under different sub-modules, packaged by their functionalities. Analyses involving lattice geometry calibration are generally handled by functions defined in the `Lattice` class. Analyses related to point-spread function (PSF) fitting are performed within the `PointSource` class. For site-resolved counts reconstruction and the extraction of occupancy matrices, operations are managed by the `SiteCounter` class. A more detailed description of the algorithms used in each of these analysis steps will be provided in a later chapter. The functional diagram of the modules is shown in Fig. 3.6.

Similar to the LabVIEW-based image analysis program, the MATLAB App is not actively synchronized with the LabVIEW control program, and its operation is not time-referenced to the experimental sequence, so the processing time may vary between experimental runs. However, unlike the LabVIEW image analysis program, which passively acquires data, the MATLAB App also actively controls devices such as the DMD. When programming a sequence that requires coordination between the MATLAB App and the LabVIEW control program, such as updating DMD patterns to address atoms, care must be taken to account for timing uncertainties and to ensure that any temporal mismatch does not compromise the experimental outcome.

The two computers (LabPC1 and LabPC2) are connected via a local network, so in principle, a network-based active synchronization scheme could be implemented as a future upgrade.

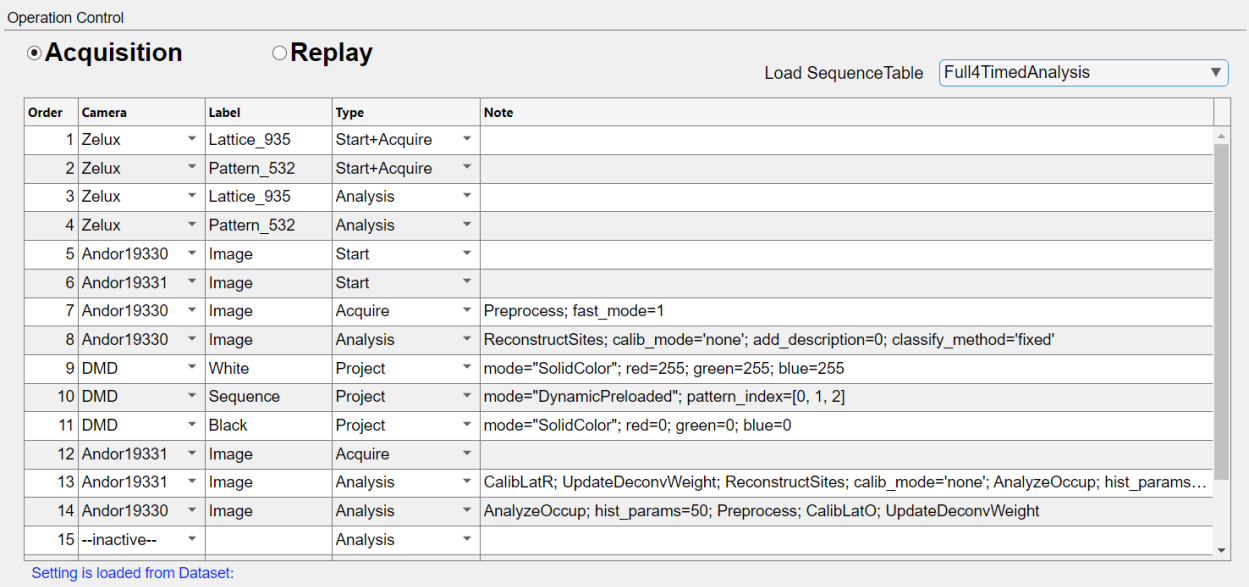

Order	Camera	Label	Type	Note
1	Zelux	Lattice_935	Start+Acquire	
2	Zelux	Pattern_532	Start+Acquire	
3	Zelux	Lattice_935	Analysis	
4	Zelux	Pattern_532	Analysis	
5	Andor19330	Image	Start	
6	Andor19331	Image	Start	
7	Andor19330	Image	Acquire	Preprocess; fast_mode=1
8	Andor19330	Image	Analysis	ReconstructSites; calib_mode='none'; add_description=0; classify_method='fixed'
9	DMD	White	Project	mode="SolidColor"; red=255; green=255; blue=255
10	DMD	Sequence	Project	mode="DynamicPreloaded"; pattern_index=[0, 1, 2]
11	DMD	Black	Project	mode="SolidColor"; red=0; green=0; blue=0
12	Andor19331	Image	Acquire	
13	Andor19331	Image	Analysis	CalibLatR; UpdateDeconvWeight; ReconstructSites; calib_mode='none'; AnalyzeOccup; hist_params…
14	Andor19330	Image	Analysis	AnalyzeOccup; hist_params=50; Preprocess; CalibLatO; UpdateDeconvWeight
15	--inactive--		Analysis	

Figure 3.5: Example of a SequenceTable in MATLAB App. For each experimental run, the app will perform a list of operations as specified by the table. *Camera* column specifies the device to operate for this operation. Currently the available devices are {`Andor19330, Andor19331, Zelux, DMD, Picomotor`}. The design architecture supports adding more devices in the future. *Type* column specifies the type of operations. For cameras {`Andor19330, Andor19331, Zelux`}, the available types are {`Start, Acquire, Start+Acquire, Analysis`}. `Start` prepares camera to receive a trigger (internal/external). `Acquire` will retrieve images from camera. `Start+Acquire` combines the two. For projectors {`DMD`}, the available operations are {`Project, Analysis`}. `Project` operation will communicate to C++ program to control the displayed pattern. It is also possible to add more DMD as projectors under this category. For picomotor driver {`Picomotor`}, the available operations are {`Move, Analysis`}. `Move` operation will communicate to the Newport driver to move the piezo actuator. For all type of devices, `Analysis` operation does not communicate to the device, but to analyze the data stored under the specified device's storage. *Note* column specifies the parameters for the corresponding operation.

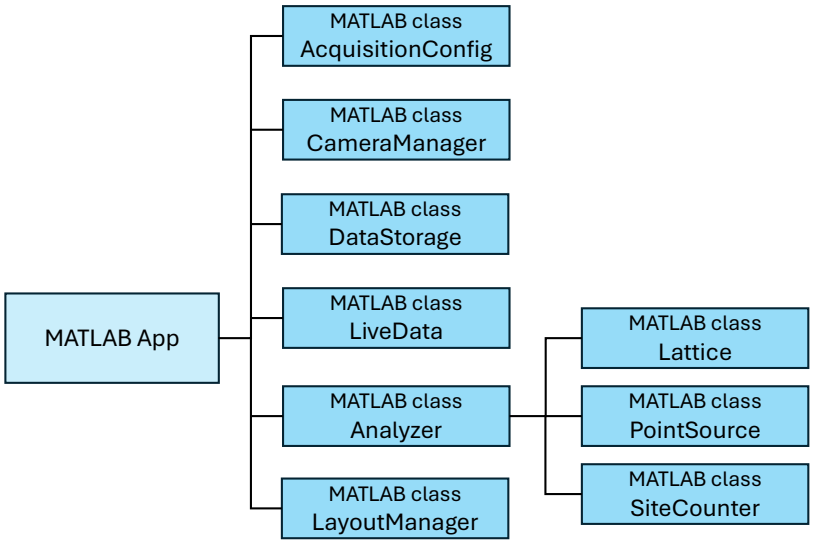

Figure 3.6: Functional diagram of the modules within MATLAB App. `AcquisitionConfig` defines a `SequenceTable` containing the list of commands to execute during a sequence. `CameraManager` manages external devices, as shown in Fig. 3.4. `DataStorage` supports storing and exporting acquired raw images. `LiveData` manages most recent acquired images and associated analysis. `Analyzer` perform specified live analysis on images through sub-modules. `Lattice` module performs lattice vector/offset calibration, cross calibration between different frames. `PointSource` module performs point-spread function (PSF) fitting. `SiteCounter` module performs deconvolution and site occupancy extraction. All the analysis sub-modules are designed to be modular and are accessible independently of the App, enabling post-processing and analysis of previously acquired data.

CHAPTER 4

DESIGN AND CONSTRUCTION OF THE APPARATUS

In this chapter, we present the design and construction of the experimental apparatus. Portions of the text are adapted from Ref. [85].

4.1 Pre-cooling satges in stainless steel chamber

We use a Zeeman slower to decelerate the atomic flux emitted from a heated Cs oven. The Zeeman slower beam is detuned by -106 MHz from $F = 4 \rightarrow F' = 5$ cycling transition, with an additional repumper component detuned by -3 MHz from $F = 3 \rightarrow F' = 4$ to maintain population at $F = 4$. A magnetic field gradient is generated by a set of Zeeman slower coils to provide the spatially varying Zeeman shift necessary to compensate the Doppler shift as atoms are slowed. The deaccelerated atoms are then captured by an MOT in the stainless steel chamber. Under typical conditions, the MOT captures approximately 7×10^6 atoms at a temperature of about 30μK with a loading time of 3 seconds.

For the MOT loading stage, we apply a current of 30 A to the bitter coils to generate the magnetic field gradient. After loading the MOT, we shutter off Zeeman slower beam and rapidly increase the coil current to 60 A to create a stronger field gradient to compress the atomic cloud. We then proceed with an optical molasses by ramping down MOT beams power and simultaneously increasing the detuning to about -100 MHz. After molasses stage, we have about 4×10^6 atoms at a temperature of 8μK. The cooling performance of molasses is sensitive to how well the background magnetic field is compensated. In our current setup, such compensation is compromised to overlap the MOT cloud to the transport lattice, which limits the molasses performance. A more optimized sequence may be implemented in the future.

4.2 Long-distance optical transport

A separate glass cell provides improved optical access for high-NA objectives and has become a standard feature in many QGM experiments. Transferring atoms to the glass cell requires long-distance transport, and the typical approaches include optical transport using a moving dipole trap [86, 87] or optical conveyor belt [88, 89, 90, 91], or magnetic transport using time-varying currents in a series of overlapping coils [92].

In our system we use an optical conveyor belt, also referred to as a 1D transport lattice, to transfer atoms from stainless steel chamber to the glass cell. This setup does not involve any mechanically moving parts and does not require a large number of magnetic coils, offering a mechanically simple and robust solution for long-distance transport.

4.2.1 Optical setup for 1D transport lattice

In some implementations of optical conveyor belts, the lattice is formed by interfering one Bessel beam and one Gaussian beam [89, 90] The purpose of a Bessel beam is to create a more uniform trapping potential over the long transport distance from its non-diffracting nature. In our system, we employ a simpler configuration consisting of two counter-propagating Gaussian beams at $\lambda = 1064$ nm to generate the transport lattice (Fig. 4.1). The incident beam power is about 35 W and the reflection has about 60% of the incident power. The beam waist of the incident beam is positioned at the midpoint between the initial and final locations of the atomic transport path. The size of the beam waist ($\sim 300\mu$m) is chosen to ensure sufficient confinement throughout the entire transport distance, as well as having a relatively long Rayleigh range of $z_R = \pi w_0^2/\lambda = 26.6$ cm such that the intensity variation across the transport distance is below 30%. The 1D lattice has an axial trap frequency of 145 kHz and a trap depth of about $200k_B \cdot \mu$K, as shown in Fig. 2.3.

To transport atoms over the 28 cm separation, we use a "flat-top" frequency profile. The atom cloud first accelerates to a velocity of approximately 0.64 m/s, and then moves at a

constant speed for the majority of the distance, and finally comes to a gentle stop at the center of the glass cell. With such a frequency profile, we are able to transport $20\% \sim 30\%$ of the initial loaded atoms within 500 ms. The typical transported atom number in the glass cell is $2 \times 10^5 \sim 5 \times 10^5$.

We use a multi-channel Direct Digital Synthesizer (DDS) as the RF sources for driving the two AOMs in the retro-reflection path. The device (Novatech, 409B) can store a frequency table and be configured to externally trigger the frequency ramp according to the loaded table, while maintaining phase coherence across different channels. However, the device only updates the frequency every 100 μs, which is slower than the timescale of axial oscillation dynamics ($\sim$ 145 kHz). This limited update rate may lead to excess heating and loss during transport [93], which can be resolved with a future upgrade.

4.2.2 Cooling in the transport lattice

In the previous experiments [83, 85], we used four 852 nm beam which is blue-detuned from $F = 3 \rightarrow F' = 2$ by 10 to 500 GHz to generate a 3D lattice and perform degenerate Raman-sideband cooling (dRSC) in this lattice, with the beam geometry closely follows Ref. [76].

In the current setup, the dRSC lattice has been removed, and the cooling is instead performed directly in the 1064 nm 1D transport lattice. Due to the presence of a $\lambda/4$ waveplate in the incident beam path, the transport lattice is circularly polarized, resulting in an estimated effective magnetic field of about 0.25 G at the trap centers. For dRSC to work, this effective field need to be canceled, and an additional magnetic field must be applied along the optical pumping beam direction to define a stable quantization axis. In the experiment, we set the z-axis magnetic field to its zero field value and scan the x and y field components to identify the optimal cooling conditions. This procedure is carried out in both the stainless steel chamber and the glass cell.

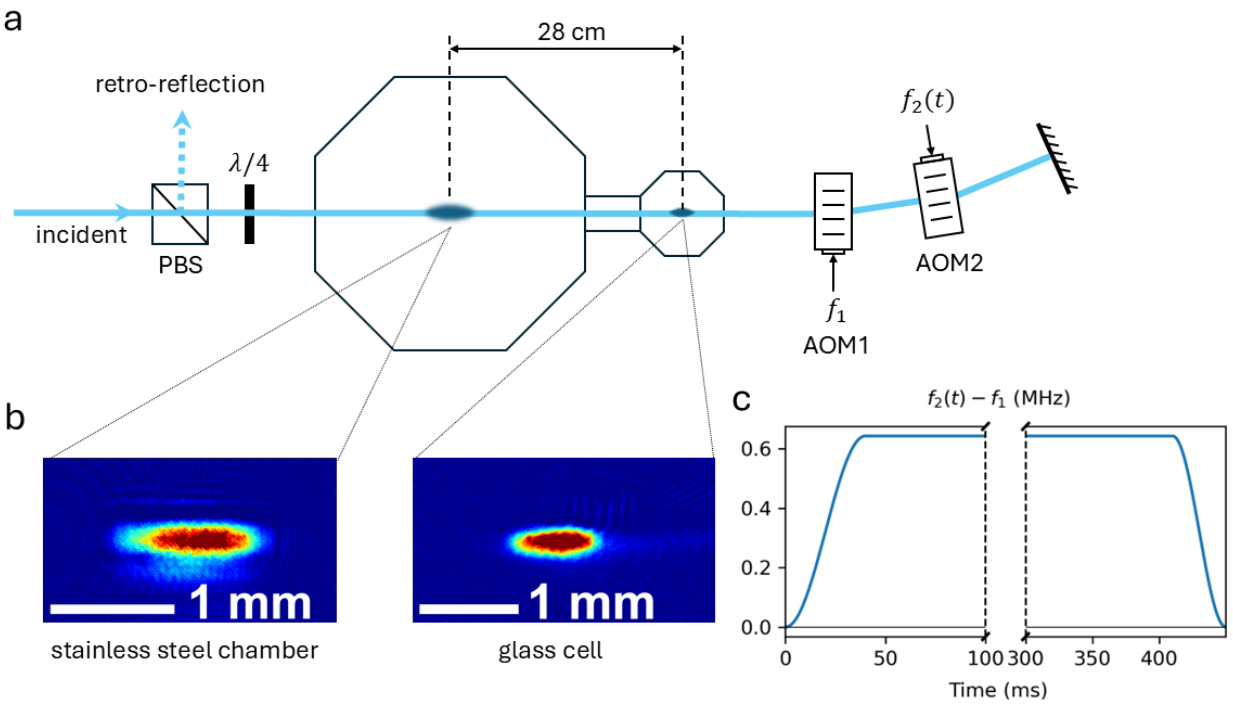

Figure 4.1: Long distance transport of atoms based on a 1D optical lattice. a. Optical setup. An incident beam at $\lambda_0 = 1064$ nm is retro-reflected, passing a pair of acousto-optic modulators (AOMs) twice. The first AOM is driven by a fixed frequency $f_1 = 80$ MHz, while the second AOM operates at a tunable frequency $f_2(t) = 80\text{MHz} + \delta(t)$. We take the $+1$ order from the first AOM and the -1 order from the second AOM, which results in the retro-reflected beam acquiring a frequency shift of $-2\delta(t)$. We vary $\delta(t)$ along a smooth trajectory to translate the lattice sites of 28 cm with speed $\lambda_0\delta(t)$. The incident beam is circularly polarized at the position of the atoms using a $\lambda/4$ waveplate. The retro-reflection maintains the same polarization as the incident beam at the atoms' location, allowing the two beams to interfere and form a 1D lattice. Both the incident and retro-reflected beams have a beam waist of 300 μm near the center of transport, resulting in a long Rayleigh range and good trap uniformity to within 15% for the entire length. b. Images of atoms in the stainless steel chamber and glass cell before and after transport. c. Frequency shift $f_2(t) - f_1$ as a function of time.

4.3 Stable optics for combining lattice and tweezers

4.3.1 Three-layer optical setup

On the glass cell side, the optical paths are arranged on a three-layer breadboard (Fig. 4.2). The optical system is comprised of two identical microscopes placed symmetrically above and below the atom sample, accesible from the upper and lower layer. The objectives (Special Optics, Inc.) are custom-designed to offer diffraction-limited performance at all the relevant wavelengths of 532, 852, and 935 nm. The objectives have a numerical aperture of NA = 0.8 and a working distance of 1.05 cm. This dual microscope configuration allows us to image the tweezer and lattice light using the diagnostic CCD in order to calibrate the tweezer position and analyze the quality of the optical potentials on the atoms.

The objectives are designed to integrate the glass cell window (silica, 5.72 mm thickness) as an optical element within the imaging system, with a nominal spacing of 1 mm between the final lens element of the objective and the outer surface of the glass cell. Both Zemax simulations and empirical alignment experience indicate that the imaging performance remains largely unaffected even when this spacing deviates by up to 50%, provided that the distance between the object plane and the inner surface of the glass cell is adjusted accordingly to compensate. The objective is infinity-corrected, meaning it transforms the optical field at the object plane into its corresponding Fourier components. To form a real-space image, it must be paired with an additional optical element, commonly referred to as an eyepiece or tube lens. In our setup, we employ a tube lens from Special Optics for both the upper and lower imaging paths, with a nominal magnification of 87×. The actual magnification varies with the object distance, and the designed magnification is realized when the distance between the object and the inner surface of the glass cell is set to 3.78 mm, while maintaining a 1 mm spacing between the objective and the outer surface of the glass cell.

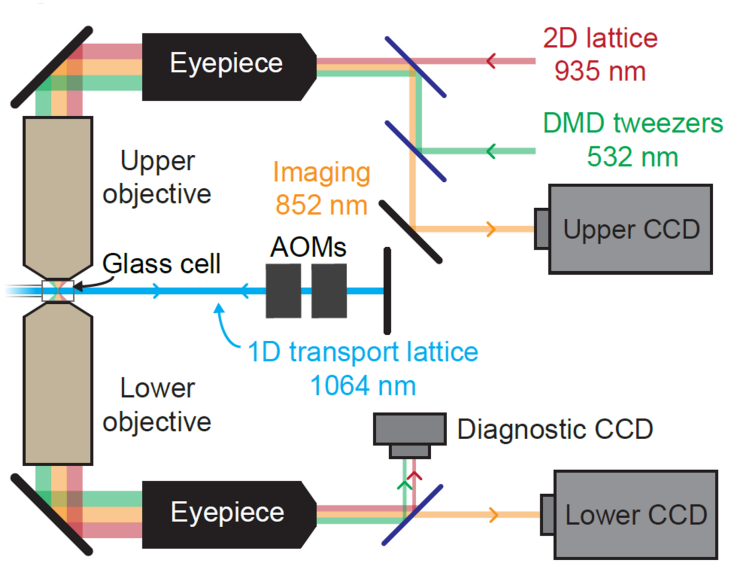

Figure 4.2: Three-layer optical setup. The general optics scheme features two high-NA microscope objectives and three cameras. The 2D lattice beams and the tweezer light are combined on the upper layer and sent through the top objective, which also collects fluorescence from the atoms to image them on the upper CCD. On the lower layer, the lower objective sends the trapping light to a diagnostic CCD, which images the optical potentials in order to diagnose aberrations and positional drift. The emitted photons from atoms are also collected on the lower CCD that serves as a secondary imaging camera. The middle layer hosts optics for the 1D transport lattice.

4.3.2 Stable mounting structure for dual objectives

An ultra-stable stainless steel cage around the glass cell holds the two microscope objectives and other supporting components (Fig. 4.3). By connecting the two objectives via a cage, the relative vibrational noise between these two sensitive optics is greatly reduced. In addition to the objectives, the stainless steel cage also supports auxiliary mirror mounts. A nearby water-cooled Bitter electromagnet is mounted on a separate structure to avoid acoustic noise caused by the water flow or large magnetic field quenches. The design of the Bitter electromagnet closely follows Ref. [94].

We test the relative mechanical stability of the 935 nm optical lattice and the 532 nm tweezers by imaging them on the lower diagnostic CCD at a fast frame rate of 650 Hz. By fitting the recorded images of the lattice sites and the tweezers, we track the variations of their positions x_L and x_D over time with high precision (Fig. 4.3.b). Details about the optical setup of the lattice and the tweezers can be found in later chapters.

We observe that the two optical potentials experience highly correlated motion, indicating the common-mode behavior of the optical paths (Fig. 4.3.c). While x_L and x_D display a root-mean-square instability of 26 nm, their relative instability is only 9 nm (Fig. 4.3.d), smaller than the expected on-site wavefunction extent. Thus, the small relative instability makes the QMS amenable to reliable arrangement of atoms in the lattice using tweezers.

4.3.3 Upgrade the system with motorized control

The objective mounting structure shown in Fig. 4.3 allows full control of x, y, z position, as well as the tip and tilt angles of objectives. For both objectives, the x and y translation degrees of freedom are implemented using an XY translation stage (OWIS, KT150), while the z-axis adjustment and tip-tilt control are provided by a three-axis mirror mount (Newport, U300-AC) mounted onto the XY stage. The entire assembly is securely fixed to the stainless steel cage structure, ensuring stable and repeatable alignment of the objectives.

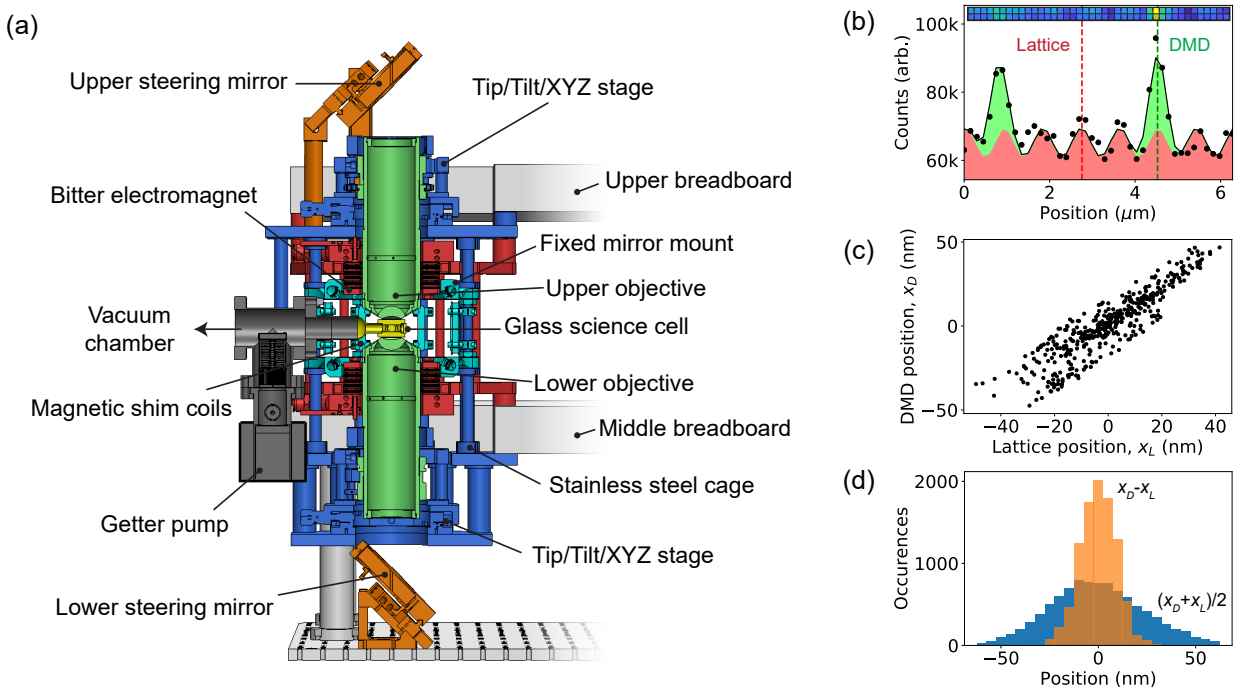

Figure 4.3: Mechanical design and stability of microscope optical system. (a) A thick stainless steel cage (blue) holds the two microscope objectives (green) around the glass cell (yellow). Nearby optics and components are also shown, including 45° steering mirrors (orange), Bitter electromagnets and mounts (red), fixed mirror mounts and magnetic shim coil (cyan), the vacuum chamber (dark gray), and the three-layer breadboard structure (light gray). (b) We analyze the mechanical stability between the tweezer light and the lattice light by imaging both simultaneously on the diagnostic CCD and observing their positions over time. We fit the lattice position (red dashed line) and the tweezer position (green dashed line) using the CCD image (inset). (c) The deviations of the tweezer position x_D and lattice position x_L are highly correlated as a result of their shared beam paths. Data are taken over 1 second at a rate of 650 Hz. (d) The difference in lattice and tweezer positions $x_D - x_L$ (orange) shows a much tighter distribution than the mean position of the lattice and DMD (blue). The RMS noise of $x_D - x_L$ is 9 nm, which is much smaller than their average fluctuation of 26 nm. Data are taken over a 20 s long measurement.

In the early design, alignment of the objectives was performed manually using the translation stage and mirror mount adjustment knobs. However, we observe that continuous transmission of laser power through the objectives could lead to noticeable thermal expansion, which in turn affected the relative alignment between the two objectives, particularly along the z axis (optical axis of both objectives, also the gravity direction). Given the small depth of focus of the objectives ($\sim$ 1 μm), even minor thermal drifts necessitated frequent manual adjustments of all three mirror mount knobs to maintain the alignment. Also, adjusting the z position requires simultaneous and symmetric tuning of all three mirror knobs, which is very difficult to execute precisely by hand and posed significant challenges to experimental stability and repeatability.

To address this issue, in early 2025 we replaced the manual actuators on the mirror mount holding the upper objective with three piezo actuators (Newport, Picomotor 8301NF), which are controlled by a motion controller (Newport, 8742) connected to LabPC2. The three picomotors are assigned to channels 2, 3, and 4 of the controller. An additional picomotor is installed on the vertical axis of one of the light sheet mirrors to control the light sheet height; this actuator is connected to channel 1. The optical configuration for the light sheet setup is described in a later chapter. The picomotor motion can be controlled either with the Newport GUI, or in the MATLAB App (Fig. 3.6).

During the upgrade, the upper objective mirror mount holder was also redesigned to accommodate the three piezo actuators. The updated design is provided in Appendix. E.

4.3.4 Alignment of the dual objectives system

Achieving diffraction-limited imaging performance requires precise alignment of the objectives relative to the rest of the optical system. We found that the alignment of other components is less critical and can usually tolerate minor misalignments without significantly degrading performance.

The geometric alignment procedures based on beam location and retro-reflection described in Ref. [82] is good for an initial alignment, but still result in significant aberration. Additionally, since the floating of optical table to suppress acoustic noise, as described in Section 4.2.1 of Ref. [82], the initial alignment to gravity no longer serves as a reliable reference. This is because the optical table supporting the glass cell can tilt in response to weight imbalances, causing the orientation of the glass cell window surface to deviate from the gravitational vertical. As a result, aligning the objective to gravity does not necessarily ensure alignment with the glass cell surface.

In our experience, to reach close to diffraction-limited resolution, it is necessary to perform the fine alignment of the objectives while actively monitoring the point-spread function (PSF). The important degrees of freedom to adjust are:

- **Focus position (z-axis)**. Defocus is the most dominant aberration when present, typically arising from a mismatch between the focal plane of the objective and the actual object plane. In our system, axial alignment of the upper objective is achieved by simultaneously moving all three piezo actuators to translate the objective along the optical axis. For the lower objective, alignment is performed manually using the three adjustment knobs on the objective mirror mount. This alignment is usually sensitive to displacement of $\sim 1\mu$m.

- **Tip and tilt angle**. Since the glass cell window serves as part of the imaging optical path and is located at a position where the incident rays have a large convergence angle, the relative angle between the objective axis and the window surface becomes critically important. Even a small angular misalignments of 1 mrad can introduce significant aberrations, particularly coma. Therefore the tip and tilt angle of the objectives should be aligned to the glass cell window surface, which unfortunately no longer has any external reference (e.g. gravity) and the alignment can only be inferred from the resulting PSF.

- **XY translation**. Our objectives have a relatively small field of view of about 100μm, meaning that objects positioned outside this region exhibit noticeable optical aberrations. This alignment is performed using the manual XY translation stages on both objectives.

Because we use a mirror mount to adjust the tip and tilt angles of the objectives, such adjustments inherently result in an accompanying displacement in the $x - y$ plane. Given that the lever arm of the tip-tilt adjustment is approximately 150 mm, a tilt of 1 mrad results in a lateral displacement of about 150 μm, which is significant relative to the small field of view of the objectives. Therefore the tip/tilt adjustment needs to be compensated with XY translation.

Another complication in the alignment process is that there is only a single mirror between the upper objective and the upper tube lens, which limits the available degrees of freedom. As a result, it is not possible to align both the angle and position of the objective relative to the tube lens, which has led to a prolonged period of severe optical aberrations in the upper CCD imaging system. To address this issue, we mounted the upper tube lens on a translation stage to provide the necessary degree of freedom. However, each time the tube lens is translated, all the beams entering the tube lens require re-alignment.

After the initial alignment to obtain images of sparsely loaded atoms on both upper and lower CCD, the fine alignment procedure that brought us close to diffraction-limited performance is outlined below:

1. **Alignment of atom cloud to the focus of lower objective.** We adjust the light sheet height with a picomotor (channel 1) to move the atoms to the focal plane of the lower objective by optimizing the sharpness of images from lower CCD.

2. **Alignment of z position of the upper objective.** We fine-tune the z position of the upper objective to optimize image sharpness on the upper CCD by We fine-tune

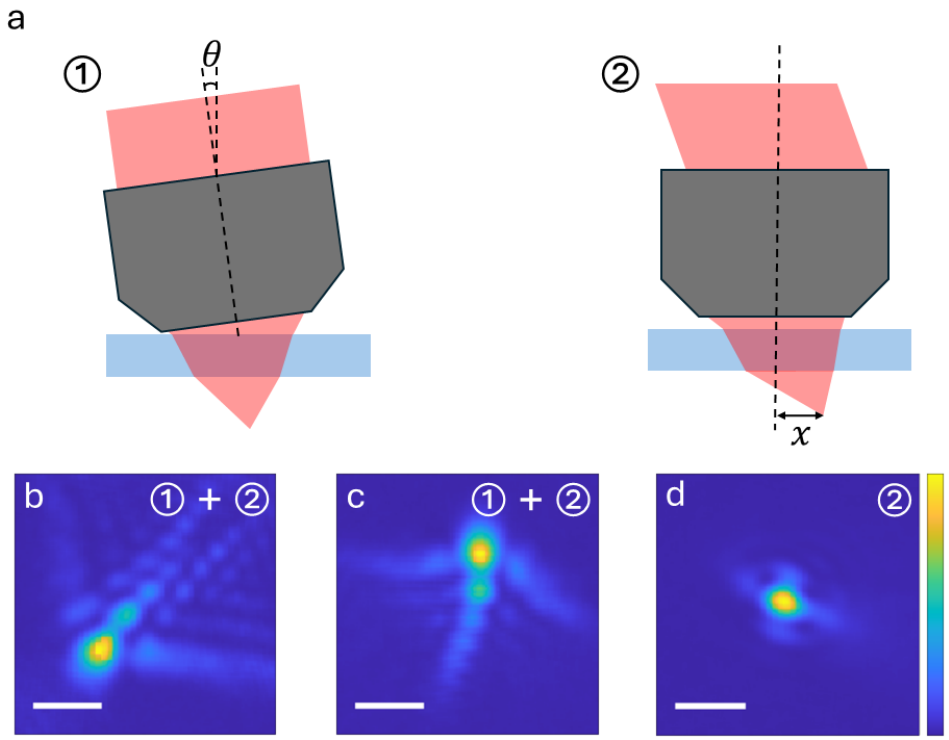

Figure 4.4: Examples of PSF shape due to different types of misalignment. a. Two types of misalignment: ① angular misalignment of θ between objective and the glass cell surface. ② translational misalignment of x caused by imaging outside of field of view. b. and c. severe coma-shaped aberrations resulting from a combination of angular misalignment and translational misalignment. The orientation of the tail indicates the direction of angular misalignment. d. cross-shaped aberration that arises from translational misalignment when the angular misalignment is small. A more comprehensive Zemax simulation of aberrations is provided in Appendix. D. The scalebar corresponds to 2μm in b, c, d.

the z position of the upper objective to optimize image sharpness on the upper CCD by simultaneously adjusting the three picomotors (channels 2, 3, and 4) by the same amount. With the precision of the picomotors, such adjustment primarily affects the z-position and results in negligible horizontal displacement of the focal point.

3. **Alignment of upper objective tip and tilt angle.** Once the images are brought into focus, the type and shape of optical aberrations can be identified. An illustration of the different types of aberrations is shown in Fig. 4.4. If the observed aberration exhibits a coma-like feature, we proceed by aligning the upper objective angle through

differential adjustment of the individual axes of the mirror mount. Each adjustment typically corresponds to an angular tilt of approximately 1 mrad. Given the 80 mm separation between the mirror mount axes, this tilt requires a differential displacement of about 40 μm, or 1000 picomotor steps, between the actuators. We may also repeat Step 2 to ensure that the upper objective remains in focus following the angular adjustment.

4. **Compensating the horizontal displacement on the upper objective.** The angular adjustment performed in Step 3 introduces a horizontal displacement of the focal point, which will shift the position of atom cloud on the lower CCD. To compensate for this displacement, we translate the upper objective using the XY translation stage to restore the atom cloud to its original location. This process is iterated in conjunction with Step 3 to optimize the PSF observed on the upper CCD, until the residual aberration appears to be dominated by a pure translational misalignment from Fig. 4.4.

5. **Alignment of upper objective XY translation.** After identifying the translational misalignment, we correct it by adjusting the upper objective position using the XY translation stage. This correction, however, also results in a shift of the atom cloud position on the upper CCD images. To compensate for this shift, we fine-tune the Fourier space angle by adjusting the 45-degree steering mirror located before the upper objective. This modification alters the propagation direction of the beam, effectively shifting the focus position in object space and restoring the atom cloud to its original location.

6. **Alignment of lower objective** Once the upper objective is aligned, we proceed with similar method to align the lower objective by optimizing the PSF from atom images on lower CCD.

This procedure empirically aligns both objectives relative to the glass cell. A more

systematic approach involves decomposing the observed PSF into Zernike polynomials, which can reveal the specific types of optical aberrations present in the system. These aberrations can then be corrected through appropriate optical alignment or compensation strategies [95].

The alignment between each objective and its corresponding tube lens, as well as between the tube lens and the camera, is performed separately with geometric methods (e.g. beam retro-reflection, reference target) that do not require active monitoring of the PSF.

CHAPTER 5

COOLING AND SITE-RESOLVED IMAGING

5.1 Optical trapping potentials

After being transported to the glass cell, atoms are loaded into a thin plane of lattice sites located at the focal plane of the objectives. Horizontal confinement is provided by a two-dimensional triangular lattice, while vertical confinement is achieved using an elliptical light sheet beam. The corresponding optical setup is illustrated in Fig. 5.1.

5.1.1 2D triangular lattice

The 2D triangular lattice is formed by the interference pattern of three circularly polarized lattice beams at 935 nm that are sent off-axis through the upper objective. The fiber output is sent to a vertical breadboard, where the beam is split into three paths using polarization optics. The three lattice beams reflect upon a curved convex mirror at the back of the setup, pass through a convex lens, and then steered by two mirrors to direct to the upper tube lens. A diagram showing the setup is in Fig. 5.2. The detailed design is also provided in Appendix. A.

We notice that the polarization of the lattice beams has a significant impact on both cooling and imaging performance, as the resulting trap geometry and the spatial polarization profile are strongly influenced by the specific polarization configuration of the lattice beams. Currently, all three lattice beams are configured to be circularly polarized immediately before entering the upper objective, as illustrated in 2.6.a. The polarization states are characterized using a polarimeter placed between the upper tube lens and the 45-degree steering mirror. In this measurement, the phase shift between the S- and P-polarized components introduced by the dielectric coating of the 45-degree mirror is also taken into account, based on a separate bench-top measurement performed under a similar configuration.

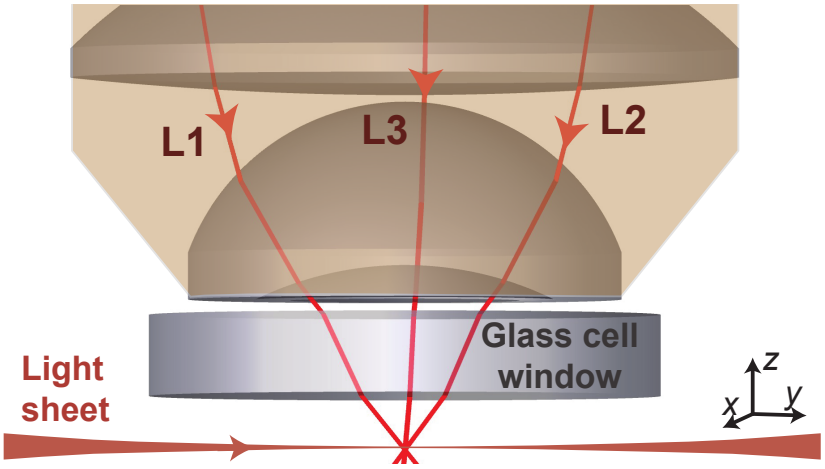

Figure 5.1: Optical potentials in the glass cell. We generate a 2D triangular lattice by intersecting three beams (L1, L2, and L3) sent from the upper objective (light brown shaded area). The light sheet propagating along the y-axis provides a tight confinement in the vertical z-direction.

The 2D lattice has a triangular geometry and a lattice spacing of 0.882μm. The estimated beam size at atom plane is 64 μm and each beam has a power of 200 mW. At full power, the trap depth is estimated to be 130 $k_B \cdot \mu$K (equivalent to 660 E_R, where $E_R = k_B \cdot 0.198\mu$K is the recoil energy), and the horizontal trap frequency is 75 kHz at sites close to the center of trapping region (Fig. 2.6). We measured the trap frequency with modulation spectroscopy and found that it is consistent with the estimation (Fig. 5.4). In the z direction, the 2D lattice also provides a weak confinement due to the limited overlap volume of interfering beams, resulting in a trap frequency of about 0.5 kHz. Because the lattice beams are at the magic wavelength, the differential light shift on the D2 transition is small compared to the excited state linewidth across the trapping region. The alignment procedure of lattice beams is provided in Appendix. B.

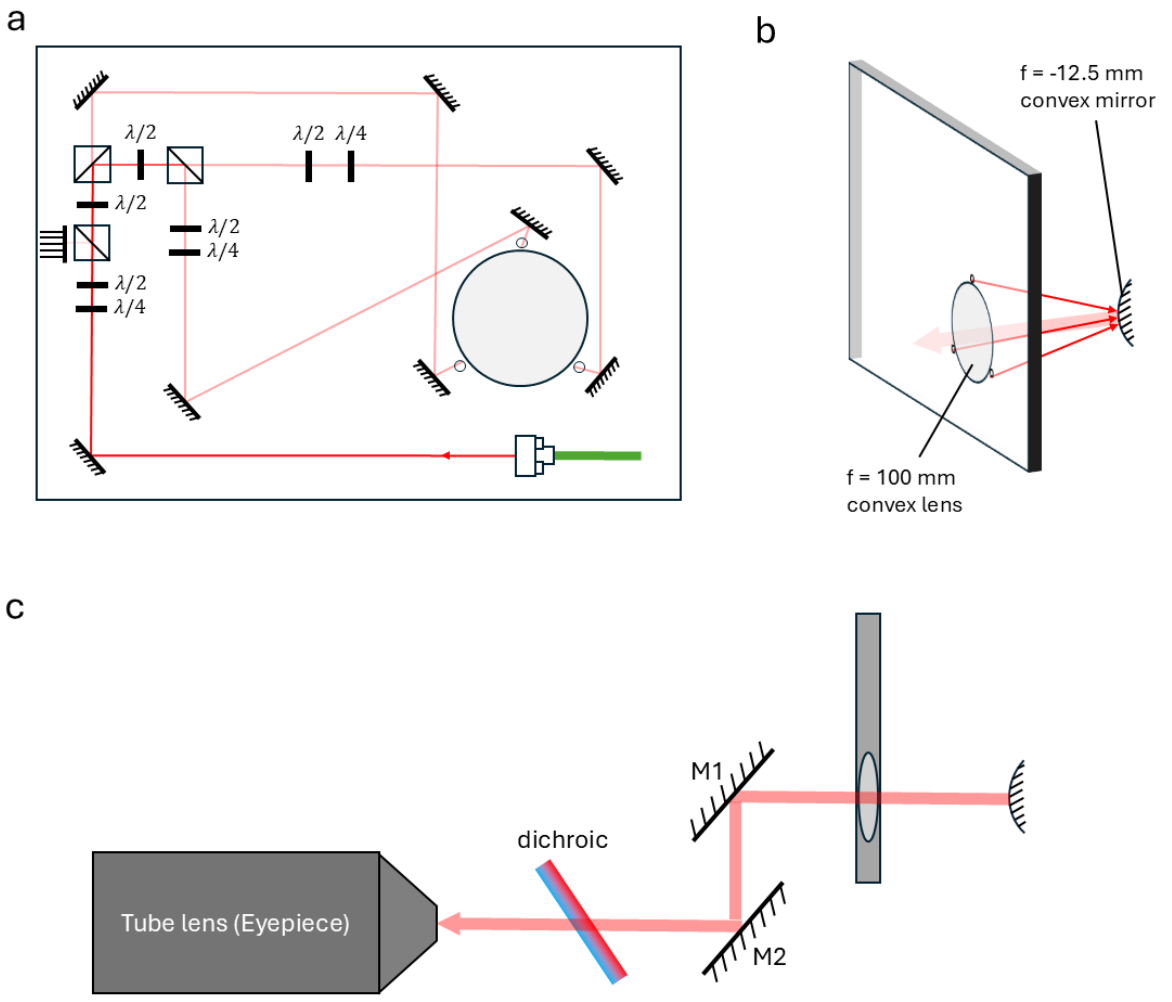

Figure 5.2: Optical configuration on a custom vertical breadboard for generating three lattice beams. a. Front view of the vertical breadboard. The fiber output, collimated using a Thorlabs C280TMD-B collimator, is split into three paths of approximately equal power using polarization optics. The darkness of the color indicates the relative optical power in each beam path. Each path includes two mirrors for beam alignment and two waveplates for polarization control. The beam geometry is designed to maintain nearly equal path lengths across the three lattice arms, minimizing relative phase drift due to thermal expansion. b. Side view of the vertical breadboard. The three lattice beams (red) are reflected to the back side of the breadboard through three cutouts positioned around an embedded convex lens (f = 100 mm, Edmund Optics, 33410). The beams converge near each other and are reflected by a convex mirror (f = -12.5 mm, Edmund Optics, 87688) located at the back of the setup. The reflected beams (light red), now with increased beam diameters and closely bundled propagation paths, pass through the embedded convex lens, which shapes them to the desired size and orientation. c. The output beams are then directed to the rest of the system using two 2-inch mirrors (M1, M2).

5.1.2 Light sheet

The light sheet comes from a linearly polarized elliptical Gaussian beam at 1064 nm, with a designed beam waists of 3.7μm along the z-axis and 60μm along the x-axis and power of 2.7 W at atom position. Those beam parameters are chosen to produce a near circular trapping potential in the $x-y$ plane while producing a strong confinement in z direction. We measured the trap frequencies with modulation spectroscopy, which yields a z-axis trap frequency of 15 kHz (Fig. 5.4) and x-axis trap frequency of about 1 kHz. We also observed a differential light shift of about 28 MHz for the D2 transition by scanning the probe beam frequency while performing absorption imaging. This results in an estimated peak intensity of $\sim$ 5000 W/mm^2 and a trap depth of about 1.2 $k_B \cdot$ mK according to Tab. 2.1. Those measurements suggest that assuming a Gaussian beam profile, the actual beam sizes are likely closer to 5.4 μm in z direction and 65 μm in x direction. The deviation from the designed beam parameters results in an elliptical trapping potential, elongated along the propagation direction, as shown in Fig. 5.3. An elongated atom cloud trapped by the light sheet is also observed in the experiments, which confirms that the beam waist in z is indeed larger than the designed value. The deviation may come from the presence of the glass cell side window in the beam path, which is not considered during the original design.

The optical setup to create the light sheet is detailed in Ref. [82]. Basically, the collimated fiber output is first set to linearly polarized in the horizontal direction, and then shaped to different horizontal and vertical beam sizes with cylinderical optics. The shaped beam is then directed by two steering mirrors before being focused onto the atomic plane by an aspherical lens (f = 100 mm, Thorlabs, AL50100H-B). The vertical axis of the last steering mirror is motorized with a piezo actuator, allowing precise and remote alignment of the z position of the atom cloud.

The last optics to focus the light sheet is an aspherical lens. In practice, such choice is important to minimize the spherical aberration when focusing the beam at a large numerical

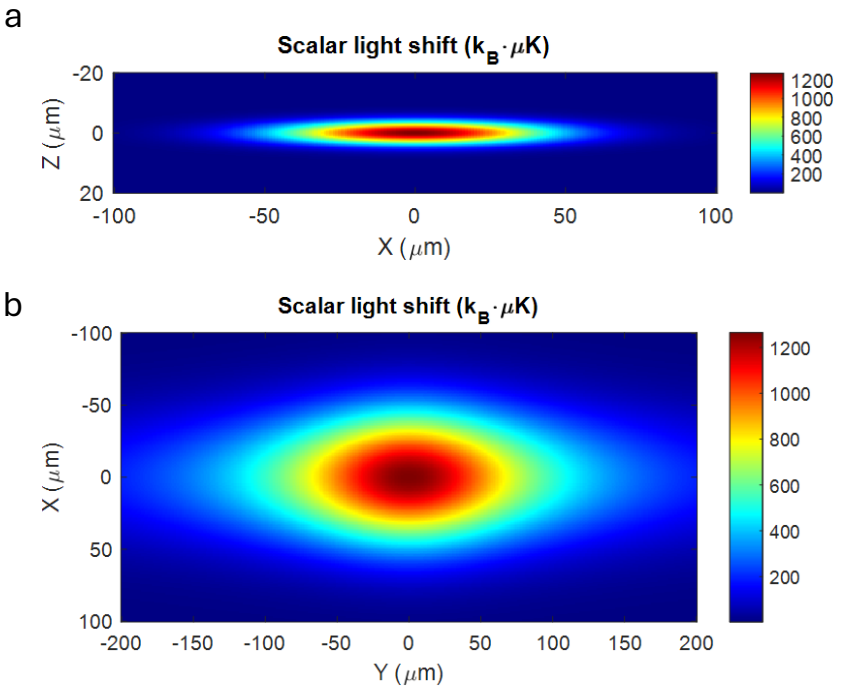

Figure 5.3: Simulated optical potentials from light sheet. The calcualtion is based on 2.7 W beam power at 1064 nm with a waist of 5.4 μm along z-axis and a waist of 65 μm along x-axis. The resulting trap depth is 1.26 $k_B \cdot$ mK and the trap frequencies are $(\nu_x, \nu_y, \nu_z) = 2\pi \times (1.3, 0.7, 16)$ kHz. a. Scalar light shift of the ground state energy on $x - z$ plane. b. Scalar light shift of the ground state energy on $x - y$ plane. The trap is elongated along y-axis, which is the beam propagation direction.

aperture. In fact, in an early design with all spherical optics, we noticed a significant aberration on the beam profile at focal plane. Generally, the spherical aberration for a plano-convex lens at infinite-conjugate can be estimated as [96]

$$\text{spot diameter } (3^{\text{r}}\text{d order spherical aberration}) = \frac{0.067f}{(\text{f}/\#)^3} \tag{5.1}$$

where f is the focal length and f/# is the f-number of the optics. This formula assumes a uniform illumination, but can still provide a reasonable estimate for focusing a Gaussian beam. Given a beam radius of about 10 mm at the position of the lens which has f = 100 mm, f-number can be estimated by f/D where D is the beam diameter. The resulting aberration-induced spot diameter is 53 μm which is much larger than the diffraction-limited spot size, therefore an aspherical optics is required for focusing the light sheet to the atoms.

5.2 Degenerate Raman-sideband cooling and imaging

Single atom detection is one of the most essential capabilities of a QGM. To achieve the necessary signal-to-noise ratio, fluorescence imaging is typically employed over absorption imaging. Reliable identification of the initial site occupancy generally requires each atom to scatter between 10^3 and 10^5 photons while being tightly localized to lattice sites. To stay sufficiently pinned in place during this process, atoms must maintain a low temperature relative to the depth of the trapping potential, even after repeated photon scattering. As a result, efficient cooling is critical for realizing high-fidelity single-atom imaging in an optical lattice.

Various cooling techniques have been developed to enable single-atom imaging in QGMs, including bright optical molasses, non-degenerate Raman-sideband cooling, and electromagnetically induced transparency (EIT) cooling [97]. In our experiment, we implement a less conventional method known as degenerate Raman-sideband cooling (dRSC), where the trap-

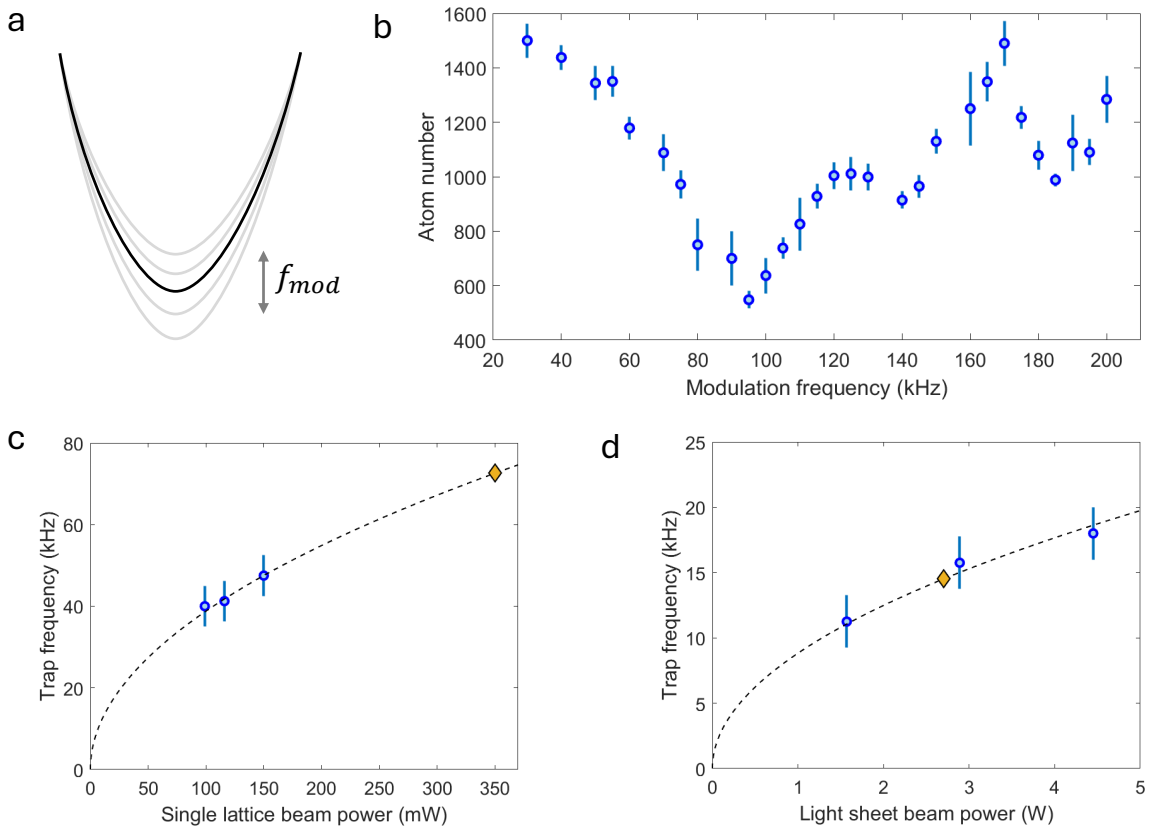

Figure 5.4: Trap frequency measurement. a. Illustration of trap amplitude modulation. Such modulation will lead to strong parametric heating when the modulation frequency f_{mod} is twice of the trap frequency. b. The remaining atom number after modulating the lattice beam power at varying modulating frequency. This measurement is performed with single lattice beam power of 150 mW. The strongest parametric heating occurs at 95 kHz which suggests the trap frequency is about 47.5 kHz. c. Measured lattice trap frequency with varying single lattice beam power (blue circle). Black dashed line is the curve $y = 3.88\sqrt{x}$. Yellow diamond corresponds to the expected trap frequency of about 73 kHz at current operating single beam power (350 mW). The single beam power is measured before upper objective, and the power at atom position is about 60% of the measured value, d. Measured light sheet vertical trap frequency with varying beam power (blue circle). Black dashed line is the curve $y = 8.83\sqrt{x}$. Yellow diamond corresponds to the expected trap frequency of about 15 kHz at the current operating light sheet beam power of 2.7 W. The power is measured at fiber output.

ping lattice simultaneously provides Raman coupling for the cooling.

5.2.1 Cooling mechanism of dRSC

Degenerate Raman-sideband cooling (dRSC) was first demonstrated in a 1D lattice to [75] and was later used to cool atoms to their motional ground states in a 3D lattice [76]. Its ability to simultaneously reduce the temperature and spin-polarize atoms in optical traps has since made it a widely adopted technique as a pre-cooling stage to increase phase-space density in many cesium BEC experiments [66, 98]. A comprehensive analysis on the cooling mechanism can be found in Ref. [99]. Briefly, the cooling cycle begins with a coherent coupling between the motional states of atoms in a harmonic trap and their internal spin states, mediated by degenerate Raman transitions driven by the trapping potentials. This is followed by optical pumping, which preferentially returns the atoms to the lowest vibrational state, thereby reducing the overall motional energy, as illustrated in Fig. 5.5.

For this cooling scheme to be effective, there are two key conditions: first, the trapping potential must induce a strong Raman coupling between the spin and motional state; second, the optical pumping process must be engineered such that the $|F = 3, m_F = 3\rangle$ state is the only dark state. For the first condition, the cooling lattice should have a spatially varying degree of circular polarization that gives rise to an effective magnetic field gradient across the lattice site centers. For example, for a 1D harmonic trap with trap frequency μ, the trapping potential is $V(x) = \frac{1}{2}m\nu^2x^2$. If there is a field gradient of $\nabla B = \partial B/\partial x$ around the trap center, it creates a spin-dependent Zeeman shift of the form $H_B = \mu_B g_F m_F(\nabla B \cdot x)$, which is linear to x, This field gradient leads to displacement of trap centers of different spin states and thereby enables a coherent coupling between motional and spin degree of freedom. Although an external magnetic field could in principle also provide a gradient across one lattice site, to have the necessary field gradient on every site, it must originate from the polarization of the lattice potential. We can estimate the magnetic field gradient required to maximize the

overlap between motional wavefunctions of different spin states. This condition yields:

$$\nabla B \sim \frac{\sqrt{m\nu^3\hbar}}{g_F\mu_B} \tag{5.2}$$

For $\nu = 2\pi \times 75$ kHz, the value is about 6.7 G/μm. With this field gradient, the Raman coupling can attain a Rabi frequency on the order of trap frequency $\Omega_R \sim \hbar\nu$.

To bring the Raman coupling into resonance, the magnitude of the total magnetic field, given by the vector sum of the effective field from the lattice and the applied external field, $|\mathbf{B}| = \mathbf{B}_{eff} + \mathbf{B}_{ext}$, must be tuned such that the Zeeman splitting between adjacent m_F levels matches the motional energy splitting

$$\hbar\nu = g_F\mu_B|\mathbf{B}| \tag{5.3}$$

Under this condition, the $|m_F = 3, \nu = 0\rangle$ state becomes detuned from the Raman coupling and thus effectively decoupled, forming the dark state under the cooling dynamics.

Another essential component of the cooling scheme is optical pumping, which continuously polarizes the atomic population into the stretched state $|m_F = F\rangle$. In the absence of optical pumping, the atoms will undergo Rabi oscillations between $|m_F, \nu\rangle$ and $|m_F - 1, \nu - 1\rangle$ without net energy dissipation. To obtain the lowest equilibrium temperature, it is important to avoid any σ^- components in the optical pumping polarization. This ensures that the stretched state $|m_F = F\rangle$ is dark to the optical fields such that the ground-state atoms will not be heated through photon scatterings. Typically, if there is no tight confinement in the direction of the optical pumping, it should be retro-reflected to balance the radiation pressure from photon scatterings.

Additionally, since the g-factor of the other ground state $F = 4$ has opposite sign, the Raman coupling will couple $|F = 4, m_F, \nu\rangle$ to $|F = 4, m_F - 1, \mu + 1\rangle$, which will introduce heating when atoms are pumped back. Therefore, a strong repumping field is necessary to

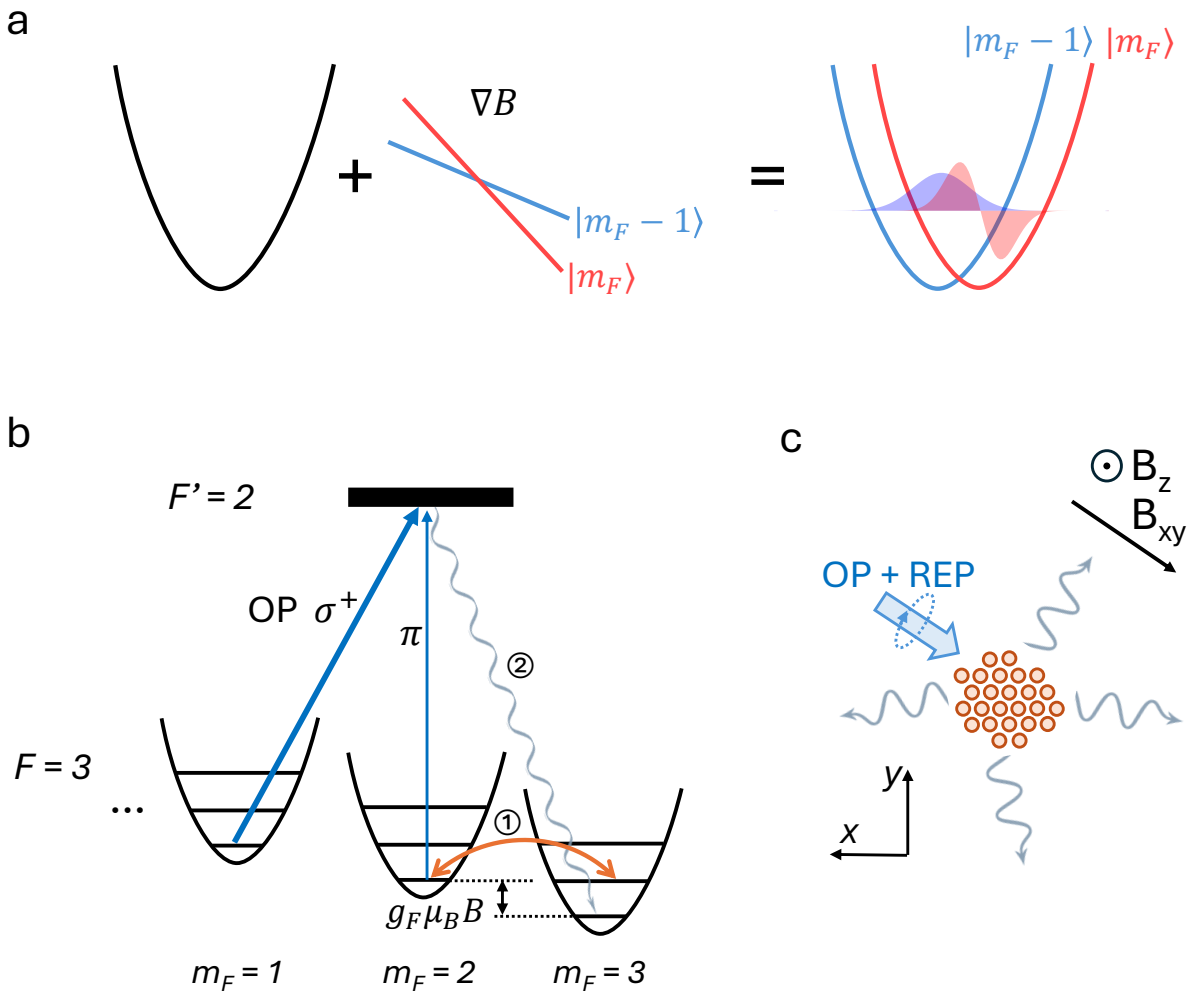

Figure 5.5: Cooling mechanism of dRSC. a. Origin of the trap-induced Raman coupling. The magnetic field gradient ∇B, arising from the polarization gradient of the lattice potential, leads to position-dependent Zeeman shifts that displace the trap centers for atoms in different magnetic sublevels. This introduces non-zero spatial overlap between the motional wavefunctions corresponding to different spin state. b. General scheme for dRSC. In step ①, the lattice potential provides a coherent Raman coupling that transfers the atoms from $|m_F, \nu\rangle$ to $|m_F - 1, \nu - 1\rangle$. In step ②, assuming the system operates within the Lamb-Dicke regime, optical pumping returns the atoms to the initial $|m_F\rangle$ spin state without changing its motional state, thereby completing one cooling cycle. OP: optical pumping beam, tuned near $3 \to 2'$ transition with both σ^+ and π polarization components. c. Optical pumping (OP), repumping beam (REP) and magnetic field configuration. Optical pumping and repumping beams are both circularly polarized and propagate collinearly toward atoms. We apply a B_z field in z direction to compensate the effective field at trap centers, and another transverse B_{xy} field to define a quantization axis close to OP/REP direction. The fluorescence photons during cooling are collected to form images.

rapidly return $F = 4$ atoms back to the $F = 3$ manifold, thereby keeping them within the cooling cycles.

5.2.2 Optical pumping and magnetic field configuration

In our system, the polarization configuration of the 2D lattice results in a strong effective magnetic field at the trap centers (see Fig. 2.6) predominantly oriented along the z-axis with an amplitude of 0.7 G. In the absence of an external bias field, this effective field alone introduces a Zeeman splitting of roughly 245 kHz between adjacent m_F states. This large splitting prevents the system from reaching the Raman resonance condition (Eqn. 5.3) unless the effective field is properly compensated. In our system, as shown in Fig. 5.5.c, we apply a z-direction field of about 0.7 G to almost fully compensate the effective field at the site centers, and another transverse field B_{xy} in the $x - y$ plane to define a quantization axis close to the optical pumping beam direction. The amplitude of the B_{xy} field is set to about 0.2 G to bring the Raman coupling into resonance. With this configuration, the estimated total field gradient $\nabla(\mathbf{B}_{eff} + \mathbf{B}_{ext})$ is about 1.3 G/μm at the center of the lattice sites (Fig. 5.6).

The cooling performance is sensitive to the magnitude of the compensation field B_z and transverse field B_{xy}, as well as optical pumping beam polarization, frequency and power. In our experiment, we obtain the lowest temperature when the optical pumping beam intensity is much lower than saturation intensity $I_{OP} \ll I_{sat}$. However, under these conditions, the photon scattering rate is significantly reduced, making it difficult to collect enough photons for high-fidelity imaging. As a compromise, the imaging parameters are optimized based on the retention probability between two back-to-back fluorescence images, as detailed later. The lowest temperature achieved after cooling with TOF measurement is about 10 μK in both horizontal and vertical directions, corresponding to average motional quantum numbers of $n_{xy} \simeq 2$ and $n_z \simeq 12$, respectively.

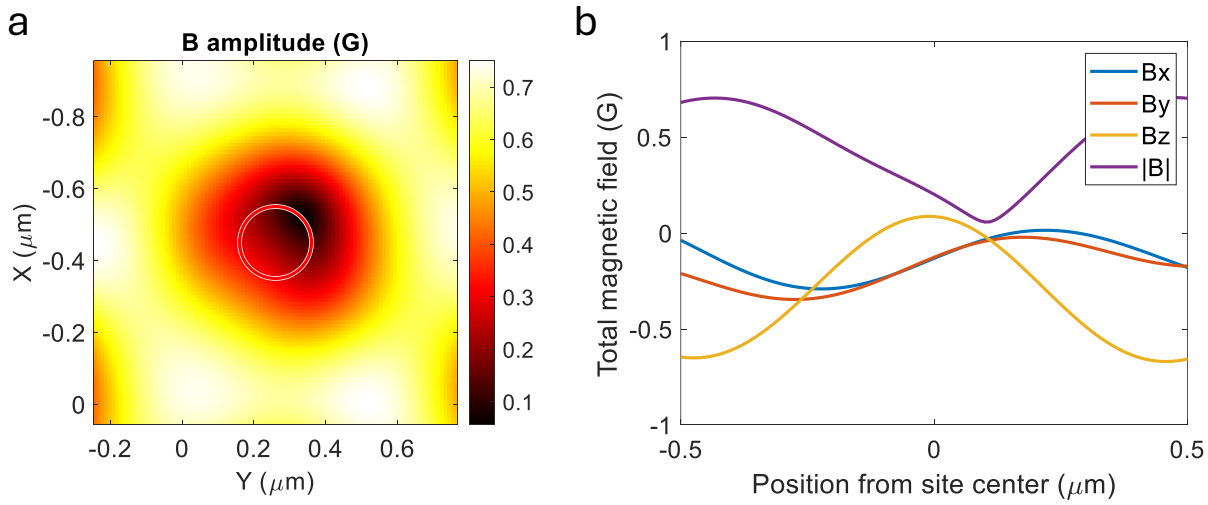

Figure 5.6: Simulated total magnetic field across a lattice site with the compensation field B_z and transverse quantization field B_{xy} configured as described in the main text. a. Total magnetic field amplitude across a lattice site. Red circle highlights the lattice site center with a radius of 0.1μm. b. Magnetic field across a line cut along (-x, y) direction through the site center. The amplitude gradient $\nabla|\mathbf{B}|$ is about 1.3 G/μm around the trap center.

Since the Raman lattice is two-dimensional and does not introduce strong Raman coupling along the z-axis, the worse cooling performance in the vertical direction is expected. In the lab, we observe that there is a weak reflection [1] of the lattice beams from the lower tube lens that propagates back to the glass cell. This stray reflection interferes with the incoming lattice beams and creates a weak vertical lattice, The resulting polarization gradient along the z-axis introduces a small Raman coupling, which contributes to additional cooling and helps lower the vertical temperature.

5.2.3 Modulating light sheet with optical pumping

When at full power (2.7 W at atoms position), the light sheet introduces a large differential light shift of about 28 MHz on the D2 transition frequency at its intensity peak. This leads

1. Most optical elements within the tube lens assembly have curved surfaces, except for the first surface facing the objective, which has a nearly zero curvature. Lattice beams are parallel to the optical axis and a small fraction of the power can be retro-reflected by this surface.

to a detuning variation across the atomic cloud on the order of excited state linewidth. Additionally, at 1064 nm, the excited state atoms experience slightly anti-trapping potential (Tab. 2.1). To mitigate the effect of the inhomogeneous detuning and anti-trapping induced heating, we modulate the light sheet out of phase with optical pumping light at 1 MHz. This scheme is similar to the work in Ref. [70].

5.2.4 Limitations for reaching ground-state cooling

The current dRSC scheme allows us to maintain relatively low atomic temperature while achieving high photon scattering, which is suitable for fluorescence imaging. However, for the ultimate goal of QMS, which is the preparation of a low-entropy atomic ensemble in the Hubbard regime, the current cooling performance is insufficient. One likely limitation arises from the residual σ^- component of the optical pumping light, which can inadvertently couple atoms in the intended dark state $|F = 3, m_F = 3\rangle$ to the excited states, thereby compromises the cooling efficiency. Although the polarization state of the optical pumping beam can be carefully adjusted, the key complication comes from the presence of a strong effective magnetic field, whose amplitude and direction vary significantly across a lattice site. In principle, applying a strong external quantization field $\mathbf{B}_{ext}$ such that $|\mathbf{B}_{ext}| \gg |\mathbf{B}_{eff}|$ would suppress the magnetic sublevel mixing and stabilize the spin quantization axis. However, due to the large amplitude of $\mathbf{B}_{eff}$ relative to the trap frequency, this configuration prevents the Raman coupling being tuned into resonance, which will still result in ineffective cooling and the presence of multiple dark states. Ideally, an improved cooling with dRSC would be achieved in a lattice geometry that provides a strong and spatially smooth effective field gradient while maintaining a small effective field amplitude across the site centers. In such configuration, an external field can reliably define the quantization axis and the optical pumping beam can retain higher polarization purity, which is the key for selective pumping into the desired dark state.

5.3 Site-resolved imaging in a triangular lattice

5.3.1 Diffraction-limited imaging from dual high-NA objectives

By collecting photons emitted during the cooling cycles, we obtain the site-resolved fluorescence images on both upper and lower CCD cameras (Fig. 5.7). With a typical image exposure time of 0.2 s, we collect about 2200 photons per atom. Given the numerical aperture and transmission loss of the imaging system, the estimated photon collection efficiency is 10%, which implies a photon scattering rate of around $\Gamma_{sc} \simeq 2\pi \times 17.5$ kHz under the imaging conditions. During imaging, the presence of near-resonance optical pumping light induces light-assisted collisions between atoms confined in the same lattice site [100]. These collisions lead to a rapid pairwise loss, resulting in a parity projection of the initial atom number. Therefore, the observed lattice occupancy is either zero or one atom per site.

By varying the MOT loading time, we control the initial atom density and thereby tune the filling fraction of the atoms in the lattice. To characterize the imaging resolution, we extract and overlay isolated single-atom fluorescence signals from sparsely loaded lattices to evaluate the PSF of both the upper and lower systems (Fig. 5.8). Currently, the images from lower CCD exhibit slightly more aberration compared to those from the upper CCD, which in principle can be improved with more careful alignment of lower objective. Nonetheless, both systems demonstrate imaging performance that approaches the diffraction limit. Since the current resolution is well below the lattice spacing (882 nm), the lattice site structures are clearly resolved.

We extract the lattice spacing in the unit of camera pixels from both upper and lower images and cross-calibrate the coordinate systems between the two CCD cameras. The extracted lattice vectors have lengths of 5.94(5.88) and 5.89(5.79) pixels on upper(lower) CCD, with an inter-vector angle of $59.9^\circ(59.8^\circ)$, consistent with the expected triangular lattice geometry.

With the calibrated lattice coordinates and the extracted PSF, we reconstruct the signal counts at each lattice site from the fluorescence images. The resulting counts distribution shows a clear separation between the occupied and unoccupied sites. By applying a threshold to this distribution, we determine the site occupancies across the lattice. A detailed description of the lattice calibration, PSF extraction and occupancy reconstruction algorithm will be provided in later sections.

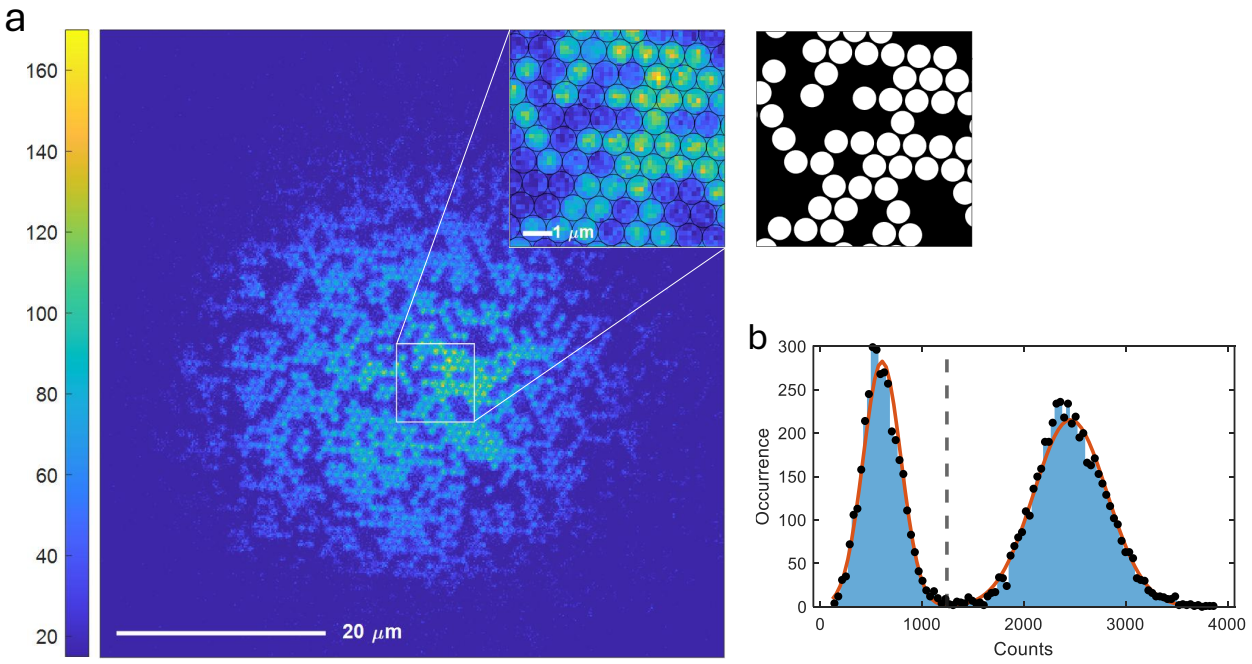

Figure 5.7: Site-resolved imaging in the triangular lattice. a. An example image obtained from the upper CCD. The filling fraction in the center of the cloud is 59%. The image next to the inset shows the reconstructed site occupancy. b. Histogram of reconstructed counts, accumulated from a hexagonal region with a radius of 8 lattice sites over 20 images. The dashed line indicates the threshold used to classify unoccupied and occupied sites. The orange curve represents a two-Gaussian fit to the data (black dots).

5.3.2 Optimizing imaging performance

To evaluate the imaging performance, we first configure the cameras to fast kinetic mode, which is a specialized acquisition mode that minimizes the delay between consecutive exposures by rapidly shifting each captured frame into a masked storage region of the CCD. We

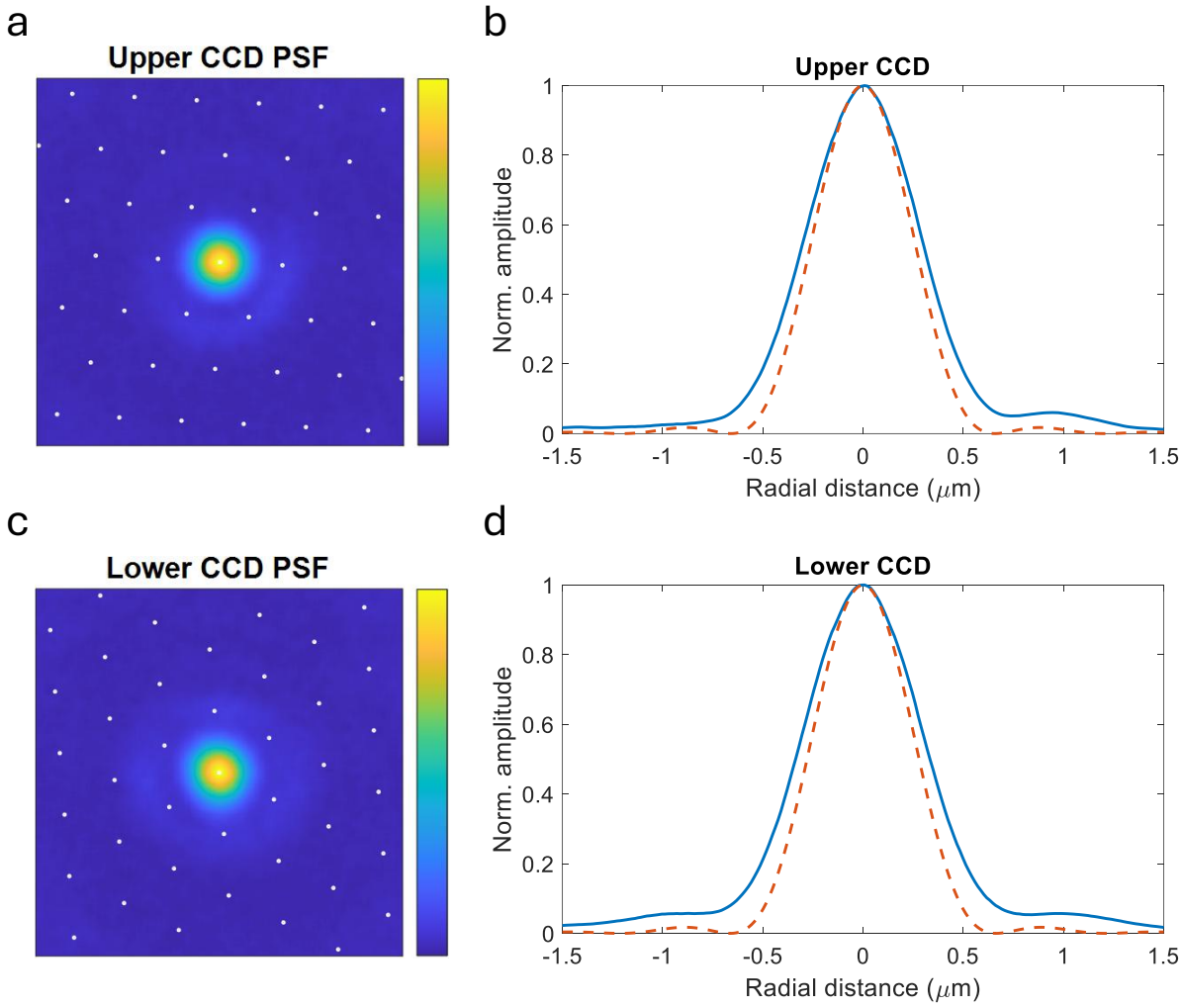

Figure 5.8: Characterization of imaging resolution. a. PSF of upper CCD images, extracted from single atom signals. b. Radial average of upper CCD PSF (blue), with a width approximately 16% larger than the ideal airy disk. c. PSF of lower CCD images, extracted from single atom signals. d. Radial average of lower CCD PSF (blue), with a width approximately 21% larger than the ideal airy disk. The white dots in panel a. and c. indicates the position of lattice sites. The dashed line in panel b. and d. (orange) indicates the radial profile of a ideal airy disk with a width of 650 nm according to Rayleigh criterion.

then acquire two fluorescence images separated by 5 ms on the same atomic sample. The 5 ms interval is limited by the vertical shift speed of the pixel of the CCDs.

To study atom hopping and loss due to the imaging, we compare the reconstructed atom occupancies of the two images and identify the fraction of atoms that are not pinned to their sites as error fraction f_{error}, the fraction of atoms that are lost from the region-of-interest (ROI) as loss fraction f_{loss}, and the fraction of atoms that emerges from a previously empty site as hopping fraction $f_{hopping}$

$$f_{error} = \frac{\#(1 \to 0)}{\#(1 \to 0) + \#(1 \to 1)} \tag{5.4}$$

$$f_{loss} = \frac{\#(1 \to 0) - \#(0 \to 1)}{\#(1 \to 0) + \#(1 \to 1)} \tag{5.5}$$

$$f_{hopping} = \frac{\#(0 \to 1)}{\#(1 \to 0) + \#(1 \to 1)} \tag{5.6}$$

where $\#(a \to b)$, $a, b \in \{0, 1\}$ is the number of sites that have a atom in the first image and b atom in the second image. Those relations also yield $f_{error} = f_{hopping} + f_{loss}$.

The error fraction f_{error} is sensitive to imaging parameters, including the amplitude of the transverse magnetic field B_{xy} and the compensation magnetic field B_z, and the frequency, power and polarization of the optical pumping and repumping beams. The error fraction with varying experimental parameters is shown in Fig. 5.9.

The most important parameter is the compensation field B_z, which has a dramatic effect on the shape of the cloud, as shown in Fig. 5.10. When B_z is small compared to the effective field at the center of the lattice, atoms in the center region experience a total field which has a large z component. Relative to this quantization axis, the optical pumping beam can acquire a significant σ^- polarization component, which drives unwanted transitions that leads to heating and atom loss. As B_z increases, the local quantization axis becomes more aligned across the lattice, improving the cooling conditions near the center and gradually eliminating

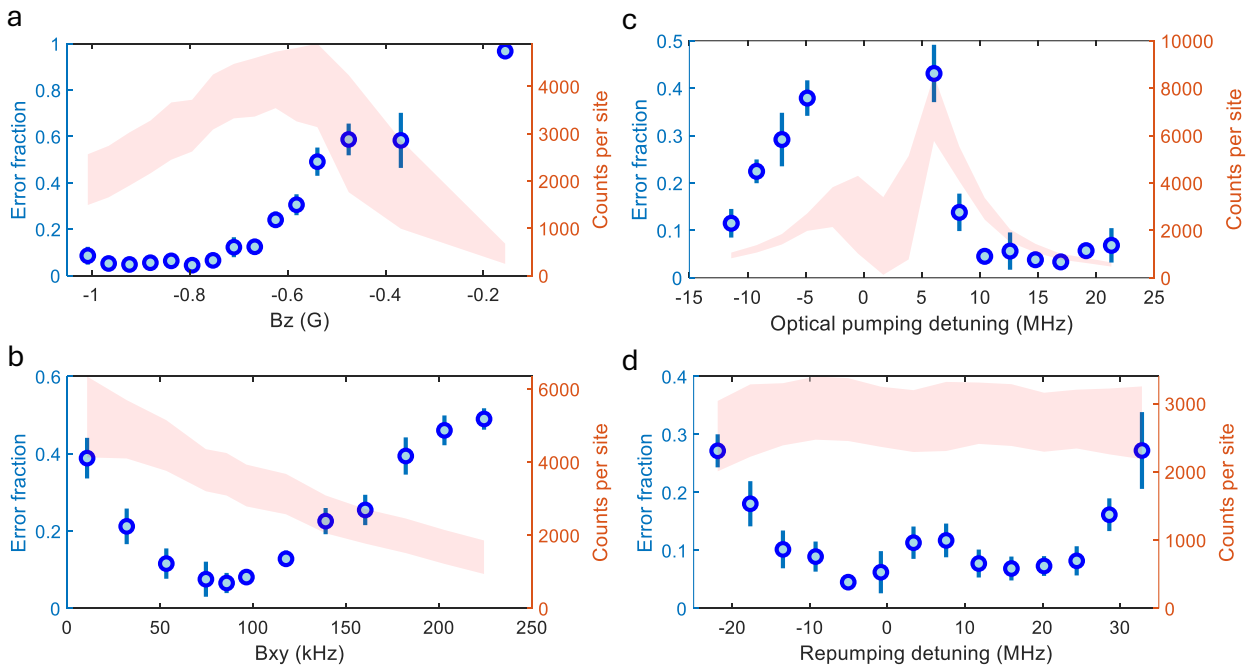

Figure 5.9: Optimization of imaging performance by varying experimental parameters. a. compensation field B_z, in the unit of G. b. transverse magnetic field B_{xy}, in the unit of the resulting Zeeman splitting between adjacent Zeeman sublevels $g_F \mu_B B/h$. c. optical pumping beam detuning. d. repumping beam detuning. Error fraction is shown as blue circle, with error bar representing one standard deviation across 20 image pairs. The signal level is indicated by the red shaded region, representing the mean counts per site from a Gaussian fit to the occupied site count distribution. The shaded area spans the 1-σ width of the fitted Gaussian at each parameter.

the central depletion. If B_z becomes significantly larger than the effective field, the cooling efficiency is also compromised due to misalignment of the quantization axis. Additionally, B_z also affects the signal level, represented by the averaged counts per occupied site, as it modifies both the Raman detuning and the polarization projection of optical pumping beam. We typically optimize B_z to obtain a low error fraction around the center region (radius of 8 sites) of the lattice. Within the range where f_{error} remains similar, B_z is set to the value that maximizes the signal level. The typical range of B_z is between 0.7 G to 0.9 G.

The transverse field B_{xy} is optimized by minimizing the error fraction. As shown in Fig. 5.9, f_{error} is minimized when B_{xy} is set such that the Zeeman splitting between adjacent

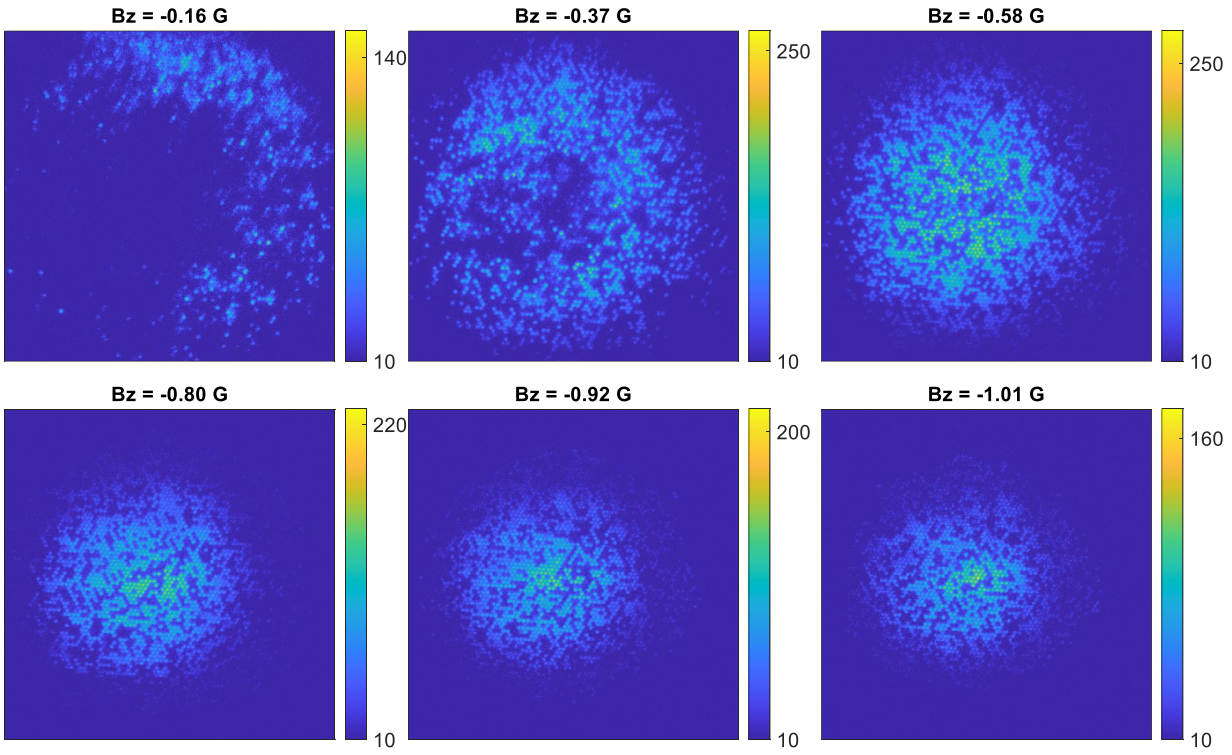

Figure 5.10: Example images at different compensation field B_z. At low B_z, atoms near the center of the lattice experience significant heating due to the presence of a strong σ^- component in the optical pumping polarization. This heating leads to atom loss, resulting in a "hole" at the center of the atomic distribution in the fluorescence image. As B_z increases, the size of this central "hole" diminishes and eventually disappears.

sublevels $g_F \mu_F B$ is close to 75 kHz, which matches the Raman resonance condition (Eqn. 5.3). B_{xy} also influences the signal level through a combined effect on the Raman detuning and the polarization projection of the optical pumping beam.

We typically set the optical pumping intensity such that $I_{OP} \gtrsim 10 I_{sat}$, corresponding to a saturation parameter $s \sim 10$. This results in an off-resonance scattering rate for excitation from $F = 3$ to $F' = 3$ given by $\frac{\Gamma}{2} \frac{s}{1+s+(2\Delta/\Gamma)^2} \sim 2\pi \times 8$ kHz. This scattering rate, which is proportional to I_{OP}, serves as the control knob for driving atoms initially in the dark state $|F = 3, m_F = 3, \nu = 0\rangle$ into bright states, therefore enables continuous fluorescence

imaging of the sample [2]. This intentional heating enhances the fluorescence signal but must be carefully balanced by efficient cooling to prevent excessive heating that could cause atoms to hop from their original lattice sites. In fact, the unwanted σ^- polarization component of the optical pumping beam can also excite atoms out of dark states through excitation to $|F' = 2, m_F = 2\rangle$. However, unlike the off-resonance heating which can be easily controlled by adjusting the laser power, this process involves near-resonance coupling and therefore more sensitive to the local polarization and magnetic field environment. Based on our experience, minimizing the σ^- component while introducing controlled heating via a high-power optical pumping beam is so far the most reliable approach for achieving effective cooling and high-fidelity imaging.

Under the condition $I_{OP} \gg I_{sat}$, we vary the optical pumping detuning to minimize the f_{error}. The detuning is usually adjusted such that the we obtain both low error fraction and also a reasonable signal level. The typical setting is blue-detuned to $3 \rightarrow 2'$ transition by $+10 \sim +15$ MHz.

Among all parameters, the repumping beam settings are the least critical for the experiment. We operate the repumping beam at an intensity well above the saturation threshold, $I_{REP} \gg I_{sat}$ to quickly repump atoms back to $F = 3$. Unlike the optical pumping beam, which is modulated out of phase with the light sheet, the repumping beam remains continuously on during imaging. The error fraction is lower when the repumping beam frequency is detuned from the resonance. As shown in Fig. 5.9, two frequency settings yields relatively low error fraction: one corresponds to the free-space resonance of the $4 \rightarrow 4'$ transition, and the other to the light-shifted resonance in the presence of light sheet. The light-shifted resonance yields a higher error fraction compared to the free-space resonance. This is because the optical pumping beam, which can transfer population into the $F = 4$ state, is active when

2. It should be noted that for $|F = 3, m_F = 3\rangle$, the coupling to the excited state $|F' = 3, m_F = 3\rangle$ requires the π-polarized component of the optical pumping beam, therefore the saturation parameter estimated using the total beam power overestimates the effective coupling strength for this transition.

atoms are not trapped by light sheet. If the repumping beam is tuned to the light-shifted resonance, it is effectively off-resonant during the free-space interval when optical pumping is on, then atoms transferred to $F = 4$ must wait until the next light shifted interval to be repumped, thereby increasing the error fraction. The signal level is not sensitive to the repumping beam frequency, which suggests that most photons collected are from the cooling cycles. We typically set the repumping beam frequency to the free-space resonance.

The optimization of imaging parameters is to find the balance between achieving a strong signal level with high scattering rate while maintaining a low error fraction, which is limited by atomic temperature. Under the optimized conditions, the error fraction for a center region with a radius of 8 lattice site is approximately 4.5(5)%. The dominant contribution arising from the thermal hopping during imaging. To quantify contribution from misclassfication errors in the occupancy reconstruction algorithm, we estimate the overlap between two fitted Gaussian in the site-wise count distribution. This analysis results in a misclassification error 0.1% error with the current signal level, which suggests the observed error fraction is limited by atom loss and hopping.

5.4 Image analysis

This section will detail the algorithms developed to process the site-resolved images.

5.4.1 Image pre-processing

We use two Andor M-934 iKon low-noise CCD cameras for single-atom imaging (Fig. 4.2). Each camera features a 1024×1024 pixel sensor with a pixel size of 13 μm. The cameras support multiple horizontal shift speed: 50 kHz, 1 MHz, 3 MHz, and 5 MHz. Higher readout speeds enable faster data acquisition but introduce increased readout noise. In addition, the camera can operate in a cropped mode that reads only a specified region of the sensor. In our experiment, we typically use a 1 MHz readout speed when no in-sequence feedback

operation is required. If faster data acquisition is required, the cameras are set to 3 MHz and cropped to readout only the bottom 100 rows of pixels.

When no photons are incident on the camera sensor, each pixel exhibits a nonzero background count. This background level can vary slightly with sensor temperature and across different camera readout settings. In the experiment, we acquire a series of raw images with the camera temperature stabilized and the sensor fully blocked from light, in order to characterize the background counts for each readout speed configuration. For each setting, the background images are averaged and subsequently smoothed by filtering out high-frequency noise in Fourier space. The resulting smooth background is then used for background subtraction in image pre-processing.

Each time a new image is acquired, we perform the following pre-processing steps:

1. **Background subtraction:** The raw image is corrected by subtracting a pre-recorded background image obtained under the same acquisition settings.

2. **Ambient offset compensation:** A linear plane is fitted to the peripheral regions (the leftmost and rightmost 100-pixel-wide columns), under the assumption that these regions contain no signal. This fitted plane is then subtracted to remove any residual offset due to ambient light.

3. **Outlier removal:** Bright pixels are identified and removed from the images.

For live analysis, the pre-processing can be configured in a fast mode that performs only basic background subtraction to minimize computation time.

5.4.2 Lattice geometry calibration

To extract lattice vectors from atom images, we apply the following steps on the pre-processed image $\mathbf{I} \in \mathbb{R}^{M \times N}$, where I_{ij} denotes the signal counts at pixel position (i, j) and M and N are the number of pixels per row and column:

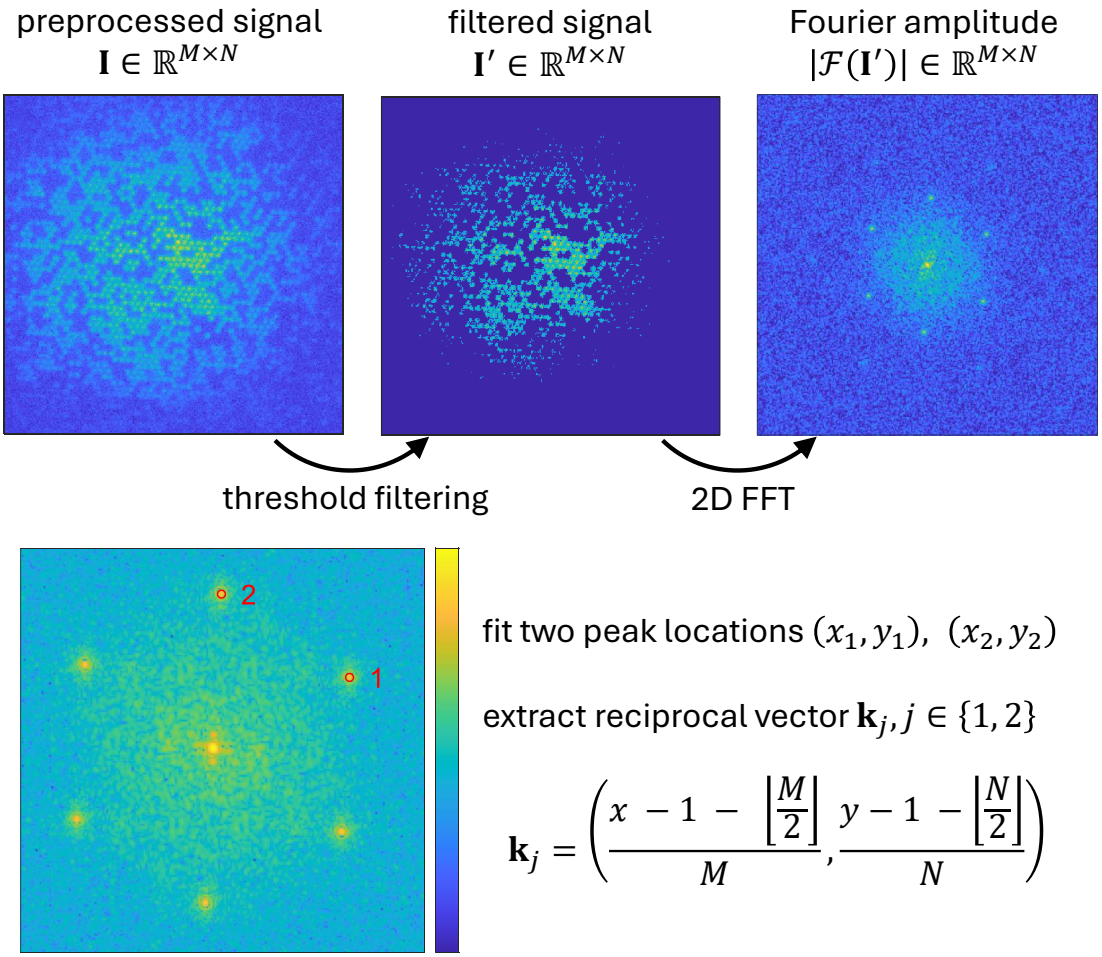

Figure 5.11: Procedure to extract reciprocal vectors from images with periodic structure. Starting from a preprocessed image $\mathbf{I} \in \mathbb{R}^{M \times N}$, first, obtain a filtered image $\mathbf{I}'$ by applying a threshold filter. Next, obtain the Fourier amplitude spectrum $|\mathcal{F}\{\mathbf{I}'\}|$. The reciprocal lattice vectors $\mathbf{k}$ can be extracted from the fitted peak positions and the size of original image (M, N).

1. **Threshold filtering.** We apply a threshold filter T to suppress background noise in the image (Fig. 5.11). The threshold T is usually set to $T = 0.5 \max(\mathbf{I})$.

$$I'_{ij} = \begin{cases} I_{ij}, & \text{if } I_{ij} \geq T \\ 0, & \text{otherwise} \end{cases} \tag{5.7}$$

After the filtering, the residual non-zero elements in $\mathbf{I'}$ is mostly coming from actual signal. By using a relatively high threshold, the spatial spread of each point source to its neighboring sites sites is also suppressed, which improves the precision of determining the lattice site centers.

2. **Extracting lattice vectors.** We apply a 2D discrete fast Fourier transform (FFT) on the filtered image $\mathbf{I'}$ to obtain the complex Fourier space image $\tilde{\mathbf{I}} = \mathcal{F}\{\mathbf{I'}\}, \tilde{\mathbf{I}} \in \mathbb{C}^{M \times N}$ and its amplitude spectrum $|\tilde{\mathbf{I}}| \in \mathbb{R}^{M \times N}$. In $\tilde{\mathbf{I}}$, there are six peaks corresponding to six reciprocal lattice vectors (Fig. 5.11). In practice, we usually fit two 2D Gaussian functions to the amplitude spectrum to identify the locations of two peaks, from which we extract two linearly independent reciprocal vectors $\mathbf{k}_1, \mathbf{k}_2 \in \mathbb{R}^2$. We then compute the corresponding real-space lattice vectors in the camera pixels coordinate system as row vectors forming the matrix $\mathbf{V} \in \mathbb{R}^{2 \times 2}$:

$$\mathbf{V} = \begin{bmatrix} \mathbf{v}_1 \\ \mathbf{v}_2 \end{bmatrix} = \left(\begin{bmatrix} \mathbf{k}_1^T & \mathbf{k}_2^T \end{bmatrix} \right)^{-1} \tag{5.8}$$

The norm of the lattice vectors $\mathbf{v}_1, \mathbf{v}_2$ determines the lattice spacing along their respective directions.

3. **Extracting lattice center.** Due to the periodic nature of the lattice, there is no absolute definition of a "center" coordinate. However, it is often convenient to define a specific lattice site near a given pixel position $\mathbf{R}_0 = (i_0, j_0)$ as the origin/center of the

lattice coordinate system. To determine the center of the lattice, we first extract the lattice phase angles along the two reciprocal vectors. The phase angle ϕ_l associated with $\mathbf{k}_l$ (for $l \in \{1, 2\}$) is computed as:

$$\phi_l = \arg\left\{ \sum_{1 \le i \le M} \sum_{1 \le j \le N} I_{ij} \exp\left(-2\pi i \mathbf{k}_l \cdot (i, j)\right) \right\} \tag{5.9}$$

where $\mathbf{k}_l$ is a reciprocal lattice vector and $(i, j) \in \mathbb{N}^2$ is the pixel coordinates. Using the extracted phase, we can then "snap" to the nearest lattice site center around $\mathbf{R}_0$ and define it as the lattice origin $\mathbf{R}$, corresponding to the site labeled $(0, 0)$ in lattice coordinates:

$$\mathbf{R} = \left(\text{round}\left(\mathbf{R}_0 \cdot \begin{bmatrix} \mathbf{k}_1^T & \mathbf{k}_2^T \end{bmatrix} + \frac{1}{2\pi}(\phi_1, \phi_2) \right) - \frac{1}{2\pi}(\phi_1, \phi_2) \right) \mathbf{V} \tag{5.10}$$

Combining the lattice origin $\mathbf{R}$ with the lattice vectors $\mathbf{V}$, the lattice coordinate system is fully defined. The mapping from the lattice coordinate (x_{lat}, y_{lat}) to pixel coordinates (x_p, y_p) is given by an *affine transform*:

$$(x_p, y_p) = (x_{lat}, y_{lat})\mathbf{V} + \mathbf{R} \tag{5.11}$$

The integer lattice coordinates $x_{lat}, y_{lat} \in \mathbb{N}$ correspond to the center of the lattice sites.

The above analysis steps can be reliably performed on a single atom image. In principle, the lattice vectors $\mathbf{V}$ and $\mathbf{R}$ can be re-calibrated in each experimental run. However, based on our experience, the lattice vector calibration of $\mathbf{V}$ remains stable across runs unless there is a significant change in system alignment. Therefore, we typically re-calibrate only the lattice center $\mathbf{R}$ while keeping the lattice vectors $\mathbf{V}$ fixed.

5.4.3 Site occupancy extraction

When the inter-site distance is large compared to the PSF, the photoelectron count per site can be accurately extracted using simple binning methods [101]. However, in most quantum gas microscope (QGM) experiments, the lattice spacing is comparable to or smaller than the PSF width, resulting in significant overlap between fluorescence signals from adjacent sites. In such cases, more sophisticated deconvolution techniques are often employed to accurately resolve site occupancies. Typical atom detection algorithms include local least-squares estimation [24], iterative deconvolution methods such as Richardson–Lucy or Wiener filtering [102, 103, 104], and deep neural network-based approaches [105, 98, 106, 107]. Among these methods, there is generally a trade-off between detection accuracy and computational speed. In our system, the imaging resolution is better than the lattice site spacing, and the in-sequence tweezer re-arrangement requires fast feedback from the acquired image. Therefore, we develop an algorithm using a linear estimator similar to recent work in Ref. [103], which provides sufficient performance and superior computational speed.

Our occupancy extraction algorithm follows three steps. First, a deconvolution kernel is constructed using the calibrated lattice vectors and the measured PSF. Second, the accumulated photoelectron counts at each lattice site are computed by applying this kernel to the image data. Finally, each site is classified as either occupied or unoccupied by applying a threshold to the extracted site-wise counts.

Calculation of a deconvolution kernel

Assume there are C_{ij} counts on the image that originate from atoms at site $(x_{lat}, y_{lat}) = (i, j)$, where $i, j \in \mathbb{N}$. In this step, we aim to find a deconvolution kernel $p(x, y)$ such that the convolution between the kernel located at this site and the image data $I(x, y)$ produces an estimate of C_{ij}:

$$\int \mathrm{d}x\, \mathrm{d}y\; I(x, y) p(x_{ij} - x, y_{ij} - y) \simeq C_{ij} \tag{5.12}$$

where $(x_{ij}, y_{ij}) = (i, j)\ \mathbf{V} + \mathbf{R}$ is the pixel-space coordinate of the center of lattice site (i, j).

We start with a forward model of the imaging process. If we know C_{ij} at all possible lattice sites (i, j), the expected count intensity at a position (x, y) on the image is modeled as:

$$I(x, y) = \sum_{i,j} C_{ij} f(x - x_{ij}, y - y_{ij}) \tag{5.13}$$

where $f(x, y)$ is the normalized PSF such that $\int \mathrm{d}x\, \mathrm{d}y f(x, y) = 1$.

In the actual system, the image is discretized and there is noise associated with photon shot noise and camera readout. If we use $\mathbf{I} \in \mathbb{R}^P$ to denote the observed image flattened into a vector of P pixels, $\mathbf{C} \in \mathbb{R}^S$ to denote the vectorized counts on the S lattice sites, $\mathbf{A} \in \mathbb{R}^{P \times S}$ to denote the system spread matrix, where each column corresponds to the PSF shifted to a specific lattice site and sampled at all P pixel positions, the forward model then becomes a linear system

$$\mathbf{I} = \mathbf{AC} + \mathbf{n} \tag{5.14}$$

Here, $\mathbf{n} \in \mathbb{R}^P$ is the random noise on the pixels. An estimation of $\mathbf{C}$ can be obtained from solving the least-square problem:

$$\hat{\mathbf{C}} = \arg\min_{\mathbf{C}} \|\mathbf{AC} - \mathbf{I}\|^2 \tag{5.15}$$

This problem has a closed-form solution

$$\hat{\mathbf{C}} = \left(\mathbf{A}^T\mathbf{A}\right)^{-1} \mathbf{A}^T\mathbf{I} = \mathbf{WI} \tag{5.16}$$

Here $\mathbf{W} = \left(\mathbf{A}^T\mathbf{A}\right)^{-1} \mathbf{A}^T \in \mathbb{R}^{S \times P}$ is the *Moore–Penrose pseudoinverse* of the spread matrix $\mathbf{A}$.

From Eqn. 5.16, it is evident the estimated count C_i at the lattice site i is a weighted sum of the image pixel value I_j, with weights given by the elements W_{ij} of the matrix $\mathbf{W}$. This

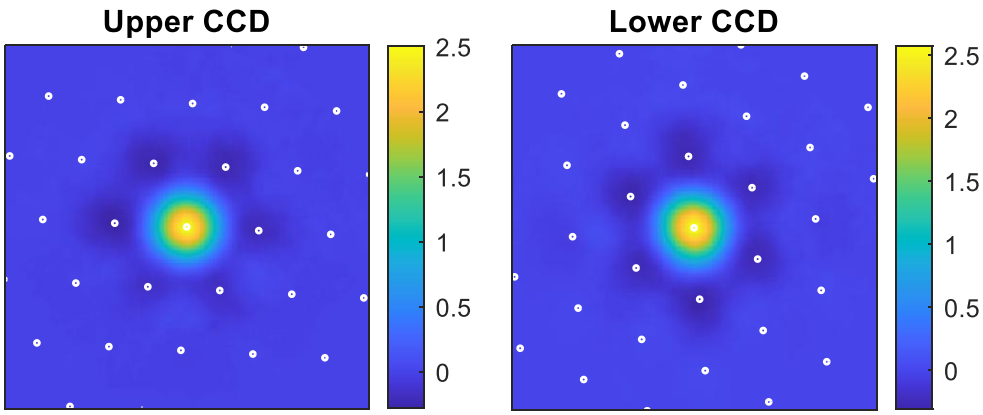

Figure 5.12: Deconvolution kernels computed for both the upper and lower CCD images. White dots indicate the positions of lattice sites in each image. Both kernels assign localized positive weights near the site centers, with slightly negative weights distributed over neighboring sites.

formulation is mathematically equivalent to the discrete form of the deconvolution kernel introduced in Eqn. 5.12. Assuming that the weights decay rapidly with the distance, the numerically computed pixel weights at a lattice site, including contributions from the site itself and its nearest neighbors, can be interpreted as a discrete realization of the deconvolution kernel $p(x, y)$. To obtain a smooth representation of the kernel, we typically calculate the weight matrix with an over-sampled pixel grid. The computation remains efficient even for a large number of sampling pixels, as the evaluation only need to include a small number of nearby lattice sites, typically less than 20. An illustration of the computed deconvolution kernel is shown in Fig. 5.12.

Site-wise count reconstruction

To estimate the site-wise counts from an image, we first shift the deconvolution kernel $p(x, y)$ computed in the previous step to the center of each target lattice site (x_{ij}, y_{ij}) to obtain the corresponding weights of its surrounding pixels. This results in a sparse weight matrix $\mathbf{M}$ which is then multiplied by the image pixel data $\mathbf{I}$, expressed as a column vector, to obtain

the reconstructed counts, also as a column vector $\mathbf{C}$.

$$\mathbf{C} = \mathbf{MI} \tag{5.17}$$

Since the matrix weights depend only on the lattice calibration parameters $\mathbf{V}, \mathbf{R}$ and the measured PSF $f(x, y)$, the pixel weight matrix $\mathbf{M}$ does not need to be updated as long as these quantities remain stable. Moreover, because the reconstruction involves only a multiplication between a sparse matrix and a vector, the computation is highly efficient: reconstructing the site-wise counts for approximately 1000 sites typically takes only a few milliseconds in the current computation environment. The rapid deconvolution is essential for fast in-sequence feedback control of tweezer patterns.

Classification based on the site-wise counts

From the extracted site-wise counts, each lattice site can be classified as either occupied or unoccupied. The current classification algorithm applies a single threshold, which is determined by fitting a two-component Gaussian mixture model (GMM) to the distribution of site-wise counts. The GMM models the probability density function of the counts c as [108]

$$P(c) = \pi_0 \mathcal{N}(c|\mu_0, \sigma_0^2) + \pi_1 \mathcal{N}(c|\mu_1, \sigma_1^2) \tag{5.18}$$

where π_0 and $\pi_1 = 1 - \pi_0$ are the mixture weights representing the probability of a site being unoccupied and occupied, (μ_0, σ_0^2) and (μ_1, σ_1^2) are the means and variances of the unoccupied and occupied site counts distributions, respectively. The classification threshold is set at the intersection point of the two Gaussian components, where their posterior probabilities are equal.

Due to spatial inhomogeneity in the current system, atoms near the center of the lattice tend to have higher fluorescence counts. To account for this variation, we have developed

a rolling threshold method that assigns different classification thresholds to lattice sites in different regions. This spatially adaptive approach improves reconstruction fidelity across larger regions of interesst.

5.4.4 Cross calibration between upper and lower CCDs

To maintain a consistent lattice coordinate system between the upper and lower CCD images such that the lattice site (i, j) corresponds to the same physical location in the atom plane on both cameras, we first align their lattice basis vectors $\mathbf{V}_{\text{upper}}$ and $\mathbf{V}_{\text{lower}}$ by intentionally selecting the lattice vectors that correspond to the same physical orientation. Then we cross-calibrate the lattice origins by mapping the lattice center of one camera to that of the other, typically aligning $\mathbf{R}_{\text{lower}}$ to $\mathbf{R}_{\text{upper}}$ (Fig. 5.13). This is achieved by imaging the same atomic sample on both CCDs and identifying the value of $\mathbf{R}_{lower}$ (from a set of candidate lattice site centers) that maximizes the similarity between the two images after transforming into the same coordinate frame. The similarity metric is the cosine angle between two vectors:

$$\text{similarity}(\mathbf{I}_1, \mathbf{I}_2) = \frac{\mathbf{I}_1 \cdot \mathbf{I}_2}{\|\mathbf{I}_1\|\|\mathbf{I}_2\|} \tag{5.19}$$

Here $\mathbf{I}_1, \mathbf{I}_2 \in \mathbb{R}^P$ are flattened vectors of transformed image data.

Once lattice origins are cross-calibrated, the upper and lower CCD images can be used interchangeably to extract atom occupancies. An example pair of images from the two cameras, transformed into the same coordinate frame, is shown in Fig. 5.14.

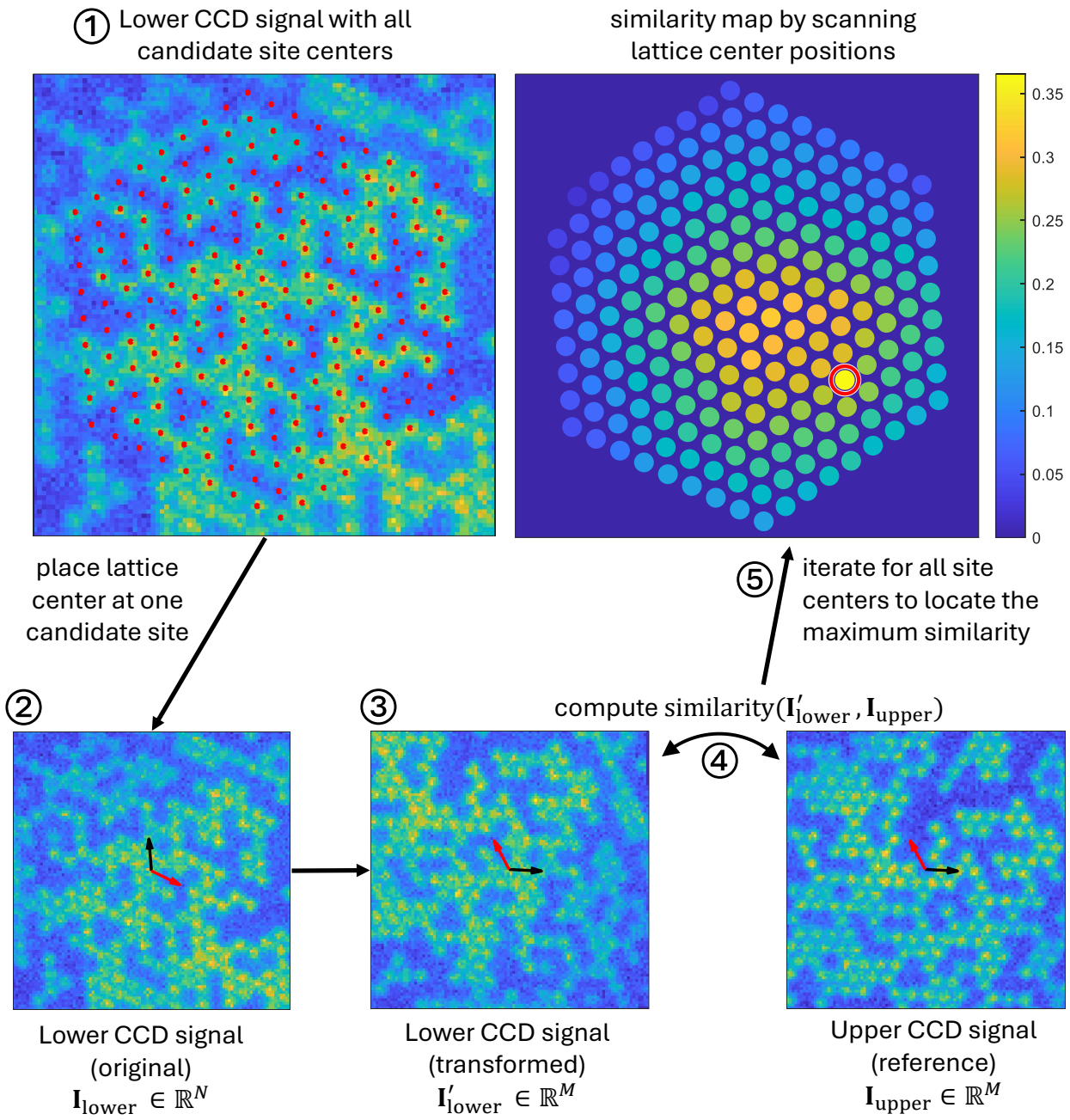

Figure 5.13: Cross calibration procedure to align lower CCD lattice origin to upper CCD. ①. Start with preparing a list of candidate sites positions (red dots) on lower CCD image data. ②. Place the lower CCD lattice origin at one candidate site. ③. Transform the lower CCD image to upper CCD frame. ④. Compute the similarity between the reference upper CCD image and the transformed lower CCD image. ⑤. Iterate the process ① to ④ for all candidate sites and locate the site that results in highest similarity (red circle). In ② to ④, black arrow and red arrows indicate orientations of the lattice vectors in each frame.

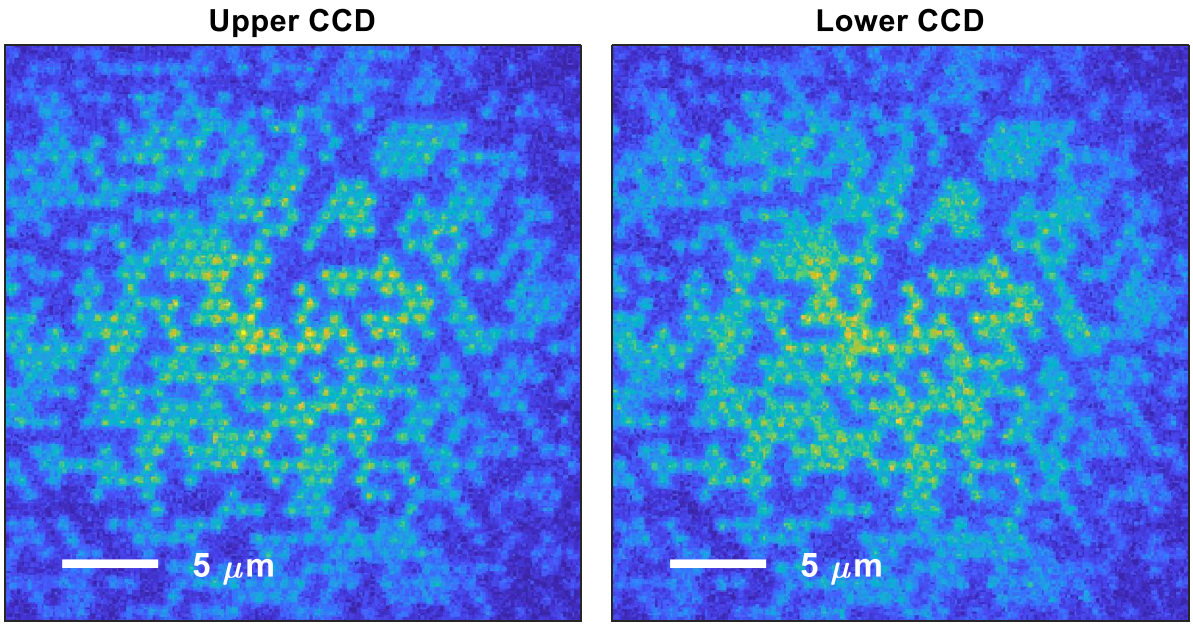

Figure 5.14: Transformed images after cross-calibrating lattice coordinates. The right image (upper CCD) and the left image (lower CCD) exhibit strong similarity after aligning their lattice bases and transforming both to a common coordinate frame.

CHAPTER 6

MOVING ATOMS WITH DMD-BASED OPTICAL TWEEZERS

6.1 Introduction to dynamic tweezers technologies

The integration of dynamic optical tweezers has revolutionized the field of cold atom research. Over the past decade, two general approaches have been developed to enable dynamic control over individual optical microtraps. The most widely adopted method is based on acousto-optical deflectors (AODs), which dynamically steer the direction of laser beams to control the positions of optical tweezers [21, 22, 109, 110, 53, 52]. Another approach employs spatial light modulators (SLMs), in which the spatial phase or intensity profile of the light field is modulated to reposition the microtraps [111, 112, 113, 114, 115, 116, 117].

AOD-based dynamic tweezer arrays typically employ two crossed AODs oriented at 90° to one another to steer a laser beam propagating through the system. By tuning the frequency of the radio-frequency (RF) signal driving the AOD crystal, the deflection angle of the laser beam along the two axis can be precisely and rapidly adjusted. Such systems can achieve update rates ranging from 10 kHz to several hundred kHz, which is limited by the acoustic propagation time in the crystal and the bandwidth of the RF electronics. However, due to the sequential XY control of beam steering in AOD-based architectures, the system provides only $2N$ degrees of freedom to control N^2 traps, making it challenging to implement fully parallel rearrangement of multiple atoms. Although appropriate algorithmic designs that take hardware constraints into account can enhance the degree of parallelism in atom rearrangement [110, 118], assembling a defect-free $L \times L$ atomic array requires a rearrangement time that scales as L^2 [118], presenting significant challenges for scaling to very large arrays within this architecture.

On the other hand, SLM-based dynamic tweezers have been attracting increasing attention in recent years. An SLM operates by modulating the phase or intensity of the incident

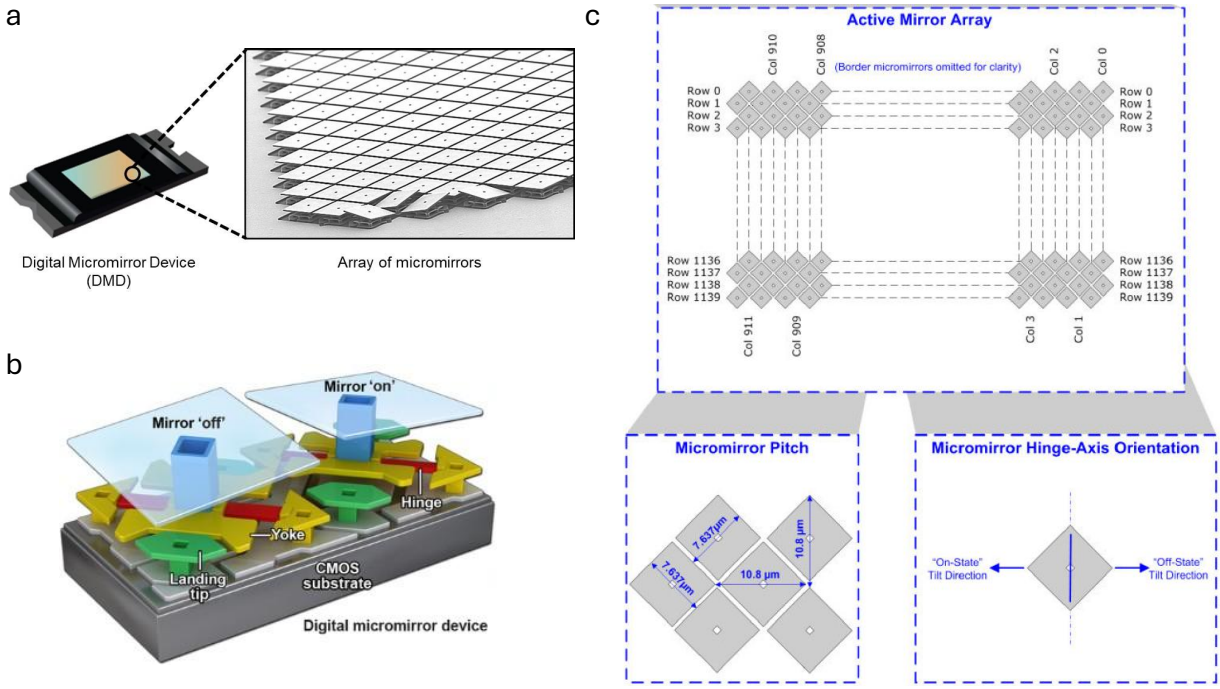

Figure 6.1: Illustration of Digital Micromirror Devices (DMD). a. A DMD comprises a large-scale array of micromirrors. b. Each micromirror can be individually toggled between ON and OFF states, enabling binary pattern projection. c. Diamond pixel arrangement of micromirrors in the Texas Instruments DLP4500 DMD. Panels a and b are adapted from online sources; panel c is modified from Ref. [119], Figure 8-1.

light across a planer pixelated device, enabling the dynamic generation of nearly arbitrary light patterns for trap formation. This architecture provides flexible and parallel control over multiple tweezers and supports the implementation of more efficient rearrangement algorithms with constant time overhead [116]. Moreover, the flexibility to arbitrarily shape the tweezer array makes SLM-based systems particularly well suited for rearrangement tasks in non-conventional lattice geometries, such as the triangular lattice used in the QMS system. A key challenge, however, is that although SLMs offer individual control over typically millions of pixels, they exhibit relatively slow update rates, typically on the order of 60 to a few hundred Hz, as they are primarily designed for display applications. These limited update rates imposed significant constraints on SLM-based dynamic tweezer experiments in the early years. More recently, however, the development and application of high-speed

SLMs with $\geq$ 1 kHz update rate have demonstrated the potential of this architecture for broader and more dynamic applications in cold atom experiments [116, 115, 120].

The most widely employed spatial light modulators (SLMs) in cold atom experiments can be broadly classified into two categories: liquid crystal on silicon SLMs (LCOS-SLMs) and digital micromirror devices (DMDs). LCOS-SLMs function by applying a voltage across a liquid crystal layer, thereby inducing local variations in the refractive index to modulate the phase of transmitted or reflected light. These devices offer high optical efficiency (typically exceeding 80%) and enable high-resolution phase modulation with bit depths ranging from 8 to 16 bits. However, their refresh rates are typically limited from 60 Hz to the lower kilohertz range due to the inherently slow response time of the liquid crystal medium. In contrast, DMDs modulate reflected light using millions of independently addressable micromirrors, each capable of rapidly switching between binary ON and OFF states by tilting between discrete angles. Modern DMDs support refresh rates exceeding 40 kHz, making them well-suited for high-speed dynamic optical applications.

Currently implemented SLM-based dynamic tweezer systems utilize a LCOS-SLM positioned at the Fourier plane of the microscope system, where it shapes the trapping light field using computer-generated holograms. DMDs, on the other hand, are primarily employed to project static intensity patterns [38, 121, 122, 123], or to display preloaded sequences of patterns without real-time adaptability [124, 125]. Their fast switching speed, combined with the absence of frequency shifts between tweezers, has also motivated applications such as optical gate controllers for quantum information processing [126]. However, it's important to note that while feedback has been used to optimize static or quasi-static patterns, the implementation of real-time control of DMD where patterns are adjusted on-the-fly based on immediate measurements, remains a developing area in the field.

6.2 Streaming dynamic patterns on DMD with fast feedback

6.2.1 High-speed real-time control with RGB bit-packing

As part of the QMS experiment, we are developing a new dynamic tweezer technology based on the direct projection of binary patterns using a DMD. We use an evaluation module (Texas Instruments, DLPLCR4500EVM), which is based on the DLP4500 DMD and the DLPC350 controller. The device features a resolution of 912×1140 micromirrors arranged in diamond pattern, as illustrated in Fig. 6.1.

As shown in Fig. 6.2, we place DMD at the image plane of the microscope system. We use a Gaussian beam at 532 nm with a power of 5.2 W to illuminate the DMD, and the spatial modulated reflection is directed through the upper imaging path to project patterns onto the atomic plane. Due to the periodic microstructure of the DMD, the incident light is diffracted into multiple orders. Maximum diffraction efficiency is achieved when the incident angle satisfies the blazed grating condition, as discussed in Ref. [127]. Empirically, we find that an incident angle of 24° relative to the normal of the DMD micromirror ON state surface yields an optimized diffraction efficiency of approximately 55%. The diffracted beam propagates through the upper imaging optics and forms a Gaussian intensity envelope at the atom plane with a $1/e^2$ radius of 15 μm, as measured from diagnostic images acquired using a camera (Thorlabs, Zelux CS165MU1) placed in the lower imaging path to re-image the projected optical potentials.

Since the incident angle on the DMD is selected to maximize diffraction efficiency, the normal to the DMD substrate is intentionally tilted by 12° with respect to the optical axis of the system. The tilt angle of the DMD will result in a tilted focal plane at the atom position. To estimate the effect of such tilt, we notice that a change in the object distance will result in a change in the image distance multiplied by a factor of M^2, where $M \sim 87$ is the magnification of the imaging system. The focus of the edge of DMD (500 pixels away

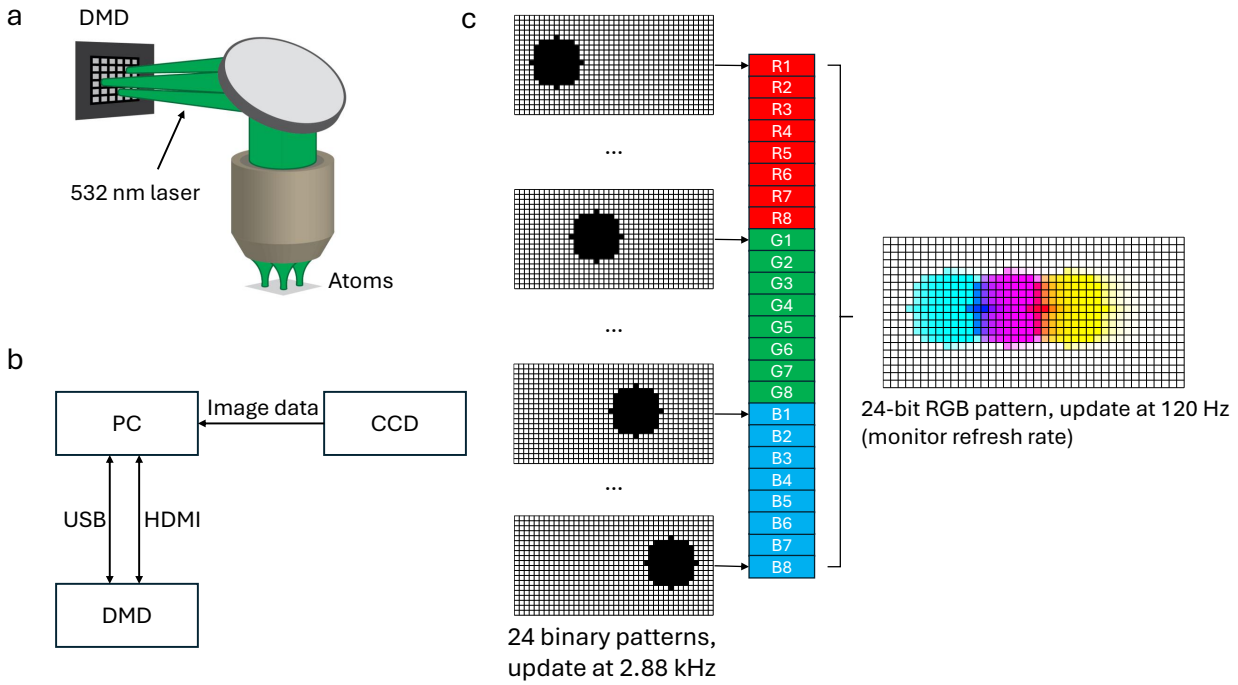

Figure 6.2: Scheme for real-time control over tweezer position with a DMD. a. Direct projection of DMD patterns onto the atom plane. We place the DMD at the image plane of our microscope and direct the reflected beam through the upper imaging system to project the binary patterns onto the atoms. b. The control architecture of the DMD. The DMD is connected to a control computer via USB for configuration and HDMI for pixel data streaming. The same computer also receives fluorescence images from CCD cameras and uses the image data to inform the generation of projected patterns. c. High-speed real-time pattern streaming using RGB bit-packing. A set of 24 binary patterns is encoded into a single RGB video frame, which is streamed to the DMD at a refresh rate of 120 Hz. The DMD is configured to sequentially display the individual bit planes, achieving a binary pattern refresh rate of 2880 Hz.

from the center) will be shifted vertically by $500 \times 7.637\mu\text{m} \times \sin(12^\circ)/M^2 \simeq 0.1\mu\text{m}$ at the atom plane, which is small compared to $\sim 1\mu$m depth of focus of our objective. Therefore, we believe that the 12° tilt angle should not compromise the resolution of the projected patterns.

Using a DMD to directly project binary amplitude patterns in real space is conceptually simpler than placing the DMD in the Fourier plane for holographic phase modulation. In the real-space configuration, patterns can be updated with minimal computational overhead, making it well-suited for applications requiring fast and flexible control, as demonstrated in experiments such as Ref. [41]. However, this simplicity comes at the expense of a reduced ability to correct for optical wavefront aberrations, which can be addressed more effectively in holographic configurations [38, 115]. In the case of a DMD, which typically functions as a binary amplitude mask, phase modulation in the Fourier plane can be implemented by tilting the micromirror substrate and using shifted pixel positions to sample specific phases of the incoming wavefront. Although such a scheme enables control over both the amplitude and phase of the optical field, it suffers from low diffraction efficiency (typically on the order of 1% of the incident beam power), making it impractical for high-power applications such as optical tweezers. On the other hand, the limited ability to compensate for wavefront errors in a real-space projection configuration can be partially mitigated through careful optical design and precise alignment of the imaging system.

To generate tweezers with real-time feedback from atom images, the DMD is connected to the same computer that acquires images from the upper and lower CCDs (LabPC2, as in Fig. 3.4). The DMD is controlled via a USB connection to the computer, while pattern data specifying the state of individual micromirrors is streamed through a High Definition Multimedia Interface (HDMI) connection. We configure the DMD in "Pattern Sequence" mode, using the video port as the input source and the vertical synchronization (VSYNC) signal as the trigger. In this configuration, the DMD decodes the RGB format video frame

into 24 binary patterns, one for each bit plane of the RGB frame, and sequentially displays them. As the DMD is recognized by the computer as an external display with a resolution matching the number of micromirrors, the pattern data is streamed as a standard RGB video signal at a refresh rate of 120 Hz. These data are directly mapped to the micromirror states and result in a binary pattern refresh rate of $24 \times 120 = 2880$ Hz.

6.2.2 Pattern update timings

To reach the highest supported 24-bit RGB frame refresh rate of 120 Hz on our DMD model, it is necessary to configure the video source to a certain format to avoid overclocking the DMD controller. Previous configuration mentioned in Ref. [82] Tab. 6.1 supports up to 105 Hz, and here we provide a modified timings configuration that supports 120 Hz frame rate in the Tab. 6.1. The video timing requirements can also be found in the DMD controller datasheet Table 4 [128]. There are other DMD and controller models that support higher pattern rates. For example, the DLP9000 DMD paired with the DLPC910 controller can achieve a 1-bit pattern rate of $>$ 13 kHz when driven by an FPGA-based pattern source [129]. Such configurations may be of interest as a future upgrade for experiments requiring faster update rates for dynamic, real-time control of optical potentials.

	Horizontal (pixels)	Vertical (lines)
Active	912	1140
Front porch	56	17
Sync width	64	10
Back porch	8	3
Total	1040	1170
Pixel clock		146 MHz
Refresh rate		119.986 Hz

Table 6.1: Video source timings configuration for 120 Hz

We characterized the refresh rate of the DMD in streaming mode by measuring the reflected beam power using a photodiode. The DMD pattern was set to a uniform gray

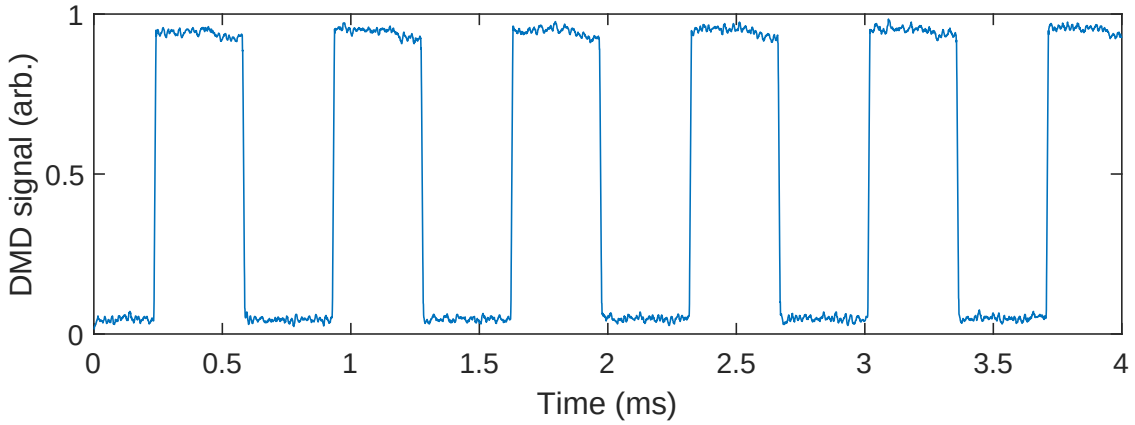

Figure 6.3: Measurement of DMD pattern refresh rate under streaming mode. The measurement is consistent with 2880 Hz binary pattern refresh rate.

pattern, with an 8-bit encoding of 10101010 on all three RGB color channels. Under this configuration, the reflected power is expected to oscillate between the fully ON and fully OFF states at the binary pattern refresh rate of 2880 Hz, which is confirmed by the photodiode signal (Fig. 6.3).

When streaming patterns from a video source, the DMD introduces a finite latency between the time a frame is transmitted and the time it is actually displayed. To estimate this latency, we first configure the DMD to display a solid black pattern, with all micromirrors in the OFF state. Immediately after reading out an image on the lower CCD, we send a solid white pattern to the DMD. The transition from black to white is monitored using a photodiode, and the rising edge of the photodiode signal confirms the moment the white frame is projected. From the timing difference between the command to update the display and the photodiode response, we measure a latency in the range of 28 ms to 50 ms. The variation in delay arises from the absence of active synchronization between the video source clock (120 Hz) and the LabVIEW control program (as described in Fig. 3.3). As a result, the command to send a new frame may align with different phases of the video frame cycle, leading to latency fluctuations of approximately ± 1 video frame, corresponding to about $\pm$ 8.3 ms given the 120 Hz refresh rate.

We estimate the total time required to complete a full rearrangement feedback cycle. The image readout step takes approximately 38 ms, using the Andor CCD configured with a 3 MHz readout speed and a cropped region of 100 pixels in height. Subsequent image analysis, including identification of occupied lattice sites and generation of the corresponding tweezer patterns, takes less than 5 ms using a vectorized algorithm. Given the current imaging magnification, approximately 10 DMD pixels correspond to one lattice site. Therefore, moving an atom across 10 lattice sites, assuming a one-pixel shift per frame, requires 100 binary pattern updates. At a binary pattern refresh rate of 2880 Hz, this sequence takes approximately 35 ms to finish. Including the display latency of about 40 ms, the total time for a complete feedback cycle is approximately 120 ms. This estimate suggests that sub-100 ms rearrangement cycles may be achievable with further upgrade, particularly by reducing camera readout time, atom transport duration, and display latency. Such improvements can be realized through the use of more advanced hardware, namely, EMCCD or CMOS cameras with faster readout capabilities, and high-speed DMD systems driven by FPGA-based pattern sources.

Ref. [82] noted that the DMD model employed in our experiment does not exhibit micromirror flickering commonly observed in other models [130]. However, upon closer examination, we observed that our DMD model does exhibit switching noise, which appears either at the binary frame refresh interval (when the RGB frame refresh rate is shorter than two internal clock interval of around 460 μs) or at the internal clock interval of 230 μs. This flickering is accompanied by a mirror clocking pulse that periodically resets all the micromirrors to a "flat" state in preparation for updating their positions based on the underlying CMOS memory. Such switching noise is ubiquitous in DMDs and is technically challenging to eliminate. We characterize the flickering timescale of the DMD by projecting a uniform white pattern and recording the temporal signal using a fast photodiode. The measurement indicates that the flickering lasts for approximately 1–2 μs, during which the projected pattern is

temporarily disturbed. In our application involving heavy cesium atoms, such microsecond-scale disturbances are expected to be insignificant. For example, in the experiment with Rb atoms in Ref. [131], the DMD was modulated at a few kilohertz to produce time-averaged trapping potentials.

6.3 Single-site addressing with projected potentials

6.3.1 Calibration of frame transformation

To project a pattern targeted at specific lattice sites, it is important to establish a consistent frame transformation between the pixel spaces of the imaging devices (upper and lower CCDs, and the diagnostic Zelux camera) and the DMD. The following sections will detail the full calibration procedure.

Coordinate system based on physical lattice

We define a common coordinate system anchored to the physical lattice, as illustrated in Fig. 6.4. The frame calibration is defined by the lattice vectors $\mathbf{V} \in \mathbb{R}^{2\times 2}$ and the lattice origin $\mathbf{R} \in \mathbb{R}^{1\times 2}$, both expressed in the pixel units as row vectors. In each physical frame (e.g. CCD or DMD pixel space), the coordinate (x, y) in pixel units are related to the lattice-space coordinates (x_{lat}, y_{lat}), expressed in units of lattice sites, via the affine transformation in Eqn. 5.11. The coordinate transformation from frame 1 to frame 2 for a point (x, y) can be performed by first mapping the coordinate from frame 1 into the lattice space (x_{lat}, y_{lat}), and then transforming it from the lattice space into coordinates (x', y') in frame 2.

DMD diamond-oriented pixel mapping

As shown in Fig. 6.1.c, our DMD model features a diamond array orientation; as a result, the row and column indices are not linearly mapped to spatial coordinates. To ensure

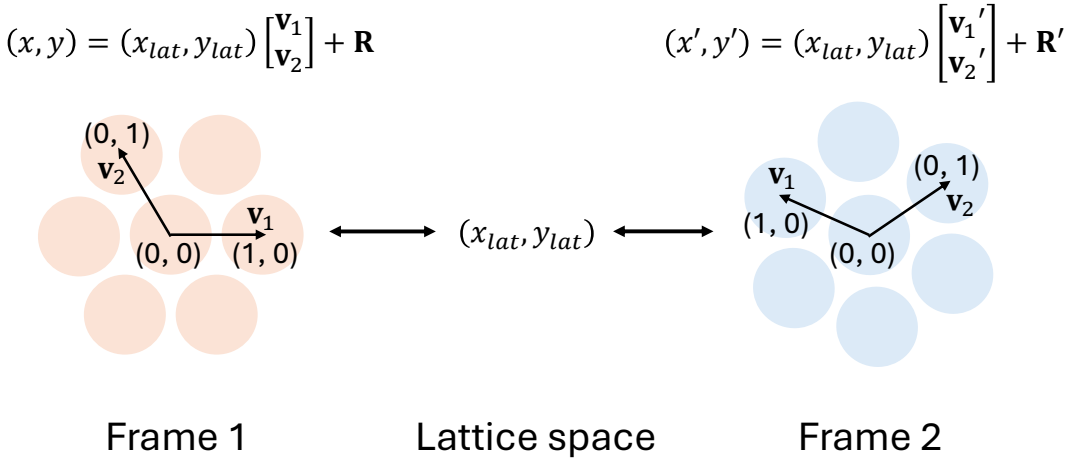

Figure 6.4: Illustration of coordinate system defined based on the physical lattice. The frame calibration $\mathbf{V} = \begin{bmatrix} \mathbf{v}_1 \\ \mathbf{v}_2 \end{bmatrix}$ specifies the lattice vectors and $\mathbf{R}$ specifies the lattice origin (the position of site labeled as (0, 0) in lattice coordinates) on a physical frame. Coordinate transformations between different frames are performed by mapping coordinates through the intermediate lattice space.

compatibility with the linear coordinate system defined earlier, we adopt a 45° rotated Cartesian coordinate system, referred to as the *real-space* coordinates, on the DMD frame.

To display a pattern on the DMD, the real-space coordinates must be converted back into the native row-column indexing scheme, hereafter referred to as the *index space*. If denote the index space coordinates as $(i, j), 1 \leq i \leq M, 1 \leq j \leq N$, where M and N are the number of rows and columns, the real space coordinates (x, y) are:

$$x = \left\lfloor \frac{M - i + 1}{2} \right\rfloor + j \tag{6.1}$$

$$y = \left\lfloor \frac{M - i}{2} \right\rfloor + N - j + 1 \tag{6.2}$$

In the following sections, references to the "DMD frame" specifically denote the real-space coordinate system defined on the DMD, rather than its native index space. The transformation from real space to index space is assumed to be applied implicitly prior to sending patterns to the DMD for projection.

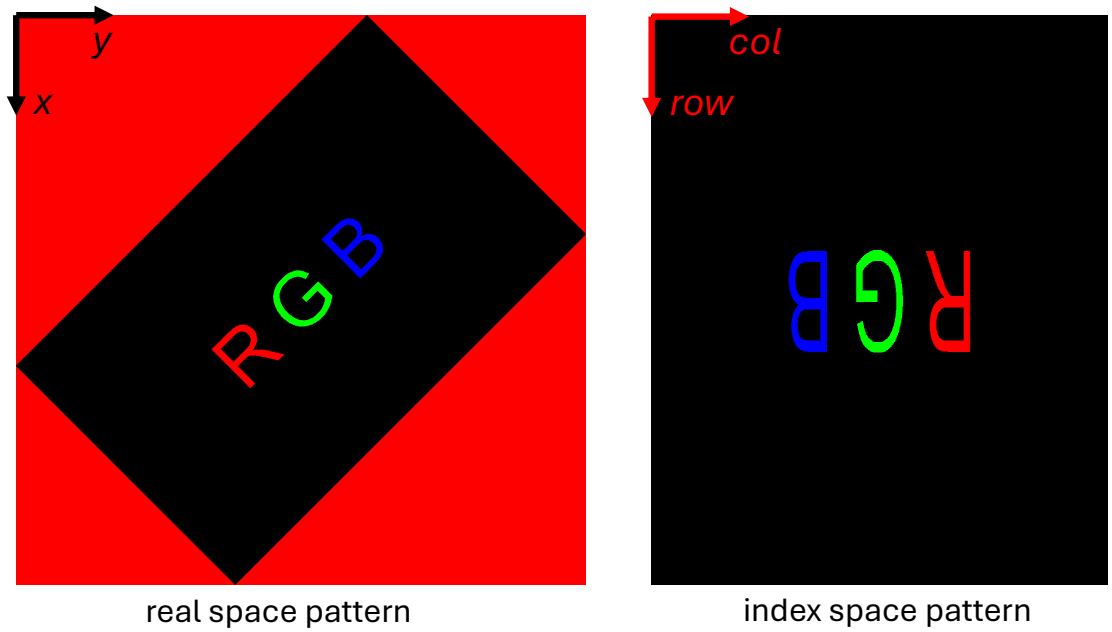

Figure 6.5: Diamond-oriented pixel mapping between real space and index space. The real space is defined as a Cartesian coordinates system rotated by 45°. The real space coordinates are arranged linearly and can be easily transformed to other coordinate systems. The red pixels in the outer part of the real space pattern are not mapped to valid DMD micromirror pixels. The index space corresponds to the native row and column indices of the DMD, which uniquely identify each micromirror but are not linearly arranged with respect to physical space.

Angle and scale calibration with direct imaging of optical potentials

To calibrate the angles and lengths of the lattice vectors $\mathbf{V}_{\mathrm{DMD}}$ in the DMD frame, we use the Zelux camera to acquire two reference images of the optical potentials. The first image (labeled as `Lattice_935`) captures the 2D triangular lattice formed by the lattice beams, while the second image (labeled as `Pattern_532`) records a calibration pattern projected by the DMD. From the first image, we perform Fourier analysis (as shown in Fig. 5.11) to extract the lattice vectors $\mathbf{V}_{\mathrm{Zelux}}$ in the Zelux camera pixel space. From the second image, we determine the affine transformation parameters $\mathbf{V}_t$ and $\mathbf{R}_t$, which define the linear mapping from the DMD frame to the Zelux camera frame. By combining this transformation with the lattice vector calibration from the first image, we obtain the lattice vectors $\mathbf{V}_{\mathrm{DMD}}$ expressed in the DMD real-space coordinate system (Fig. 6.6).

Offset calibration by imprinting patterns on atoms

To determine the position of the lattice origin $\mathbf{R}_{\mathrm{DMD}}$ in the DMD frame, we use the atoms as an absolute spatial reference. Before taking a site-resolved image, we apply a pulsed 532 nm laser modulated using an acousto-optic modulator (AOM) at a frequency of 80 kHz, thereby selectively heating and removing atoms. During the laser pulse, the DMD is set to the same calibration pattern as shown in Fig. 6.6, so that atoms located in the white (bright) regions of the pattern experience a modulated potential and are preferentially removed. Due to the stochastic nature of atom loading, the resulting images from a single experimental run varies depending on the initial distribution. However, by averaging over 20 repetitions, we can usually see a clear contrast between the modulated region and the unaffected areas. This measurement is sensitive to the spatial resolution of the projected pattern and therefore must be performed with the DMD properly positioned at the image plane of the upper objective. The detailed alignment procedure is described in Appendix C.

The calibration of $\mathbf{R}_{\mathrm{DMD}}$ takes two steps. First, from the averaged image of the atom

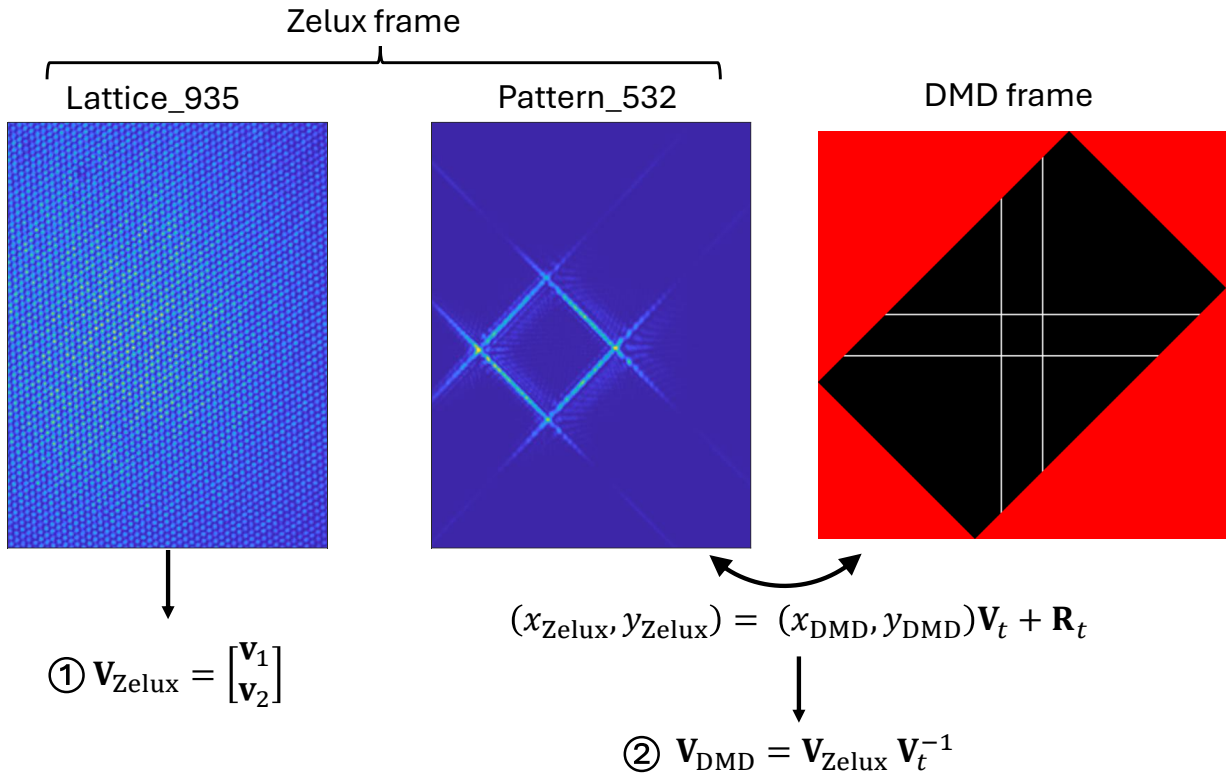

Figure 6.6: Procedure to calibrate DMD frame angle and scale. ①. From the `Lattice_935` image of the triangular lattice pattern, we extract the lattice vectors $\mathbf{V}_{\text{Zelux}}$ in the Zelux frame. ②. From the `Pattern_532` image of the calibration pattern (two horizontal and two vertical lines with a width of 5 pixels, separated by 150 pixels), we extract the transformation matrix $\mathbf{V}_t$ and offset $\mathbf{R}_t$ between the DMD frame and Zelux frame, and calculate the DMD frame lattice vector calibration $\mathbf{V}_{\text{DMD}}$ with the extracted $\mathbf{V}_{\text{Zelux}}$ from step ①. The lattice vectors in DMD frame $\mathbf{V}_{\text{DMD}}$ contains the angle and scale information.

distribution (typically acquired using the upper CCD) and the DMD pattern imaged on the Zelux camera (`Pattern_532`), we infer the absolute alignment of the Zelux camera frame by extracting the lattice origin $\mathbf{R}_{\text{Zelux}}$ (Fig. 6.7). This involves calculating the similarity between the transformed Zelux pattern image and an inverted version of the averaged atom image at various candidate positions of $\mathbf{R}_{\text{Zelux}}$. This procedure is similar to the cross-calibration between the upper and lower CCDs; however, a key difference arises due to the presence of an achromatic shift between 532 nm, 852 nm, and 935 nm. As a result, the list of candidate lattice origin positions for this calibration is not restricted to the previous calibrated lattice site centers. In practice, the calibration is typically performed in two stages: first, using a coarse grid of candidate positions aligned with the lattice site centers; and second, using a finer grid with 0.1 site step that provides sub-site resolution to account for potential achromatic shifts (Fig. 6.8).

In the second step, given the calibrated lattice origin in the DMD frame $\mathbf{R}_{\text{Zelux}}$, the corresponding position in the DMD frame $\mathbf{R}_{\text{DMD}}$, can be computed using the previously extracted affine transformation matrix $\mathbf{V}_t$ and translation vector $\mathbf{R}_t$ as:

$$\mathbf{R}_{\text{DMD}} = (\mathbf{R}_{\text{Zelux}} - \mathbf{R}_t)\,\mathbf{V}_t^{-1}. \tag{6.3}$$

Together with the angle and scale calibration matrix $\mathbf{V}_{\text{DMD}}$, this establishes a complete geometric calibration of the DMD coordinate frame.

6.3.2 Long term drift monitoring

To characterize the system's stability, we monitor the drift of the lattice origin position over time across different camera frames (Fig. 6.9). We begin by projecting a static pattern which consists of an array of white spots on a black background onto the DMD, and capture its image using the Zelux camera during MOT loading in the stainless steel chamber. We also

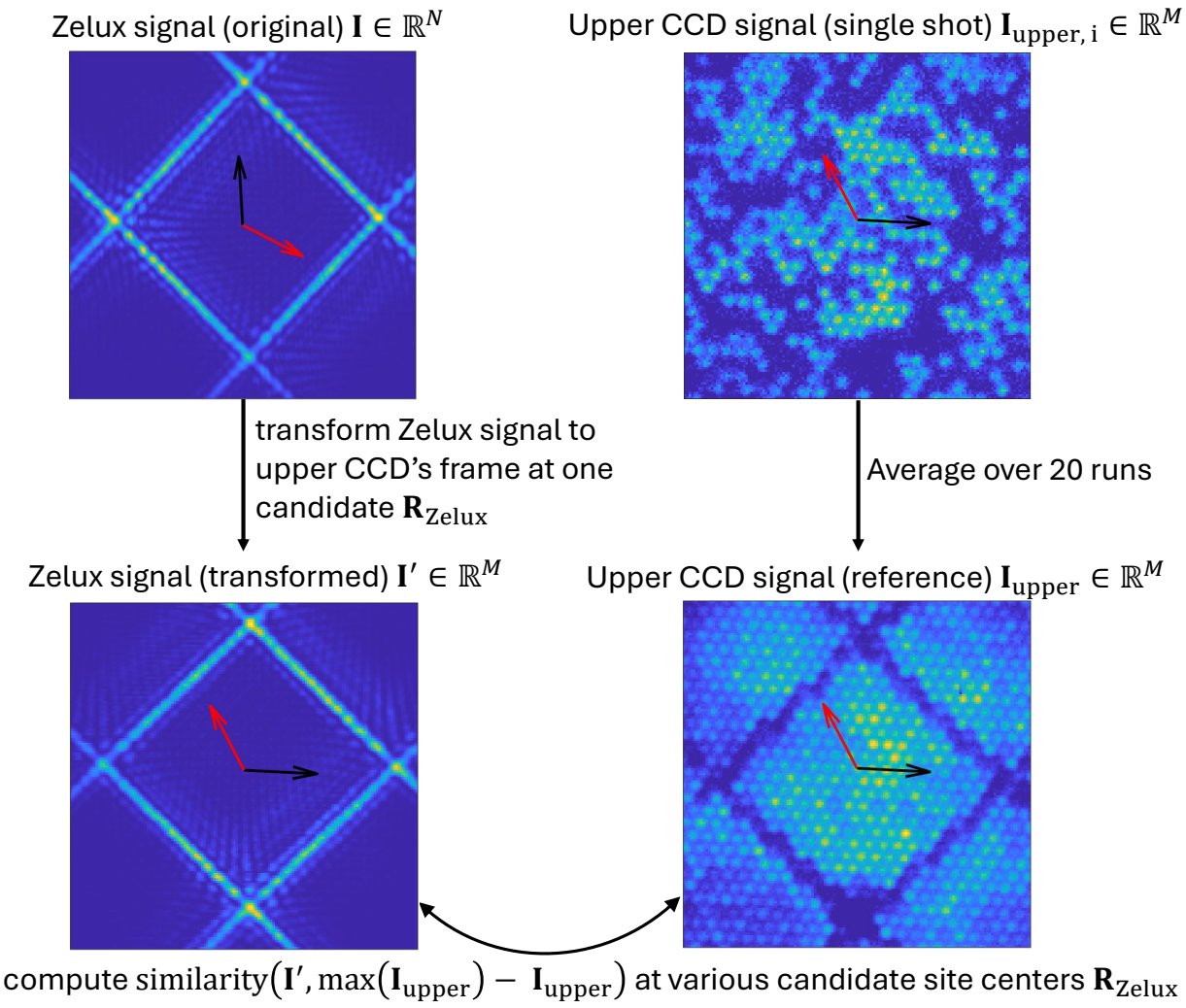

Figure 6.7: Procedure to calibrate Zelux frame lattice origin $\mathbf{R}_{\mathrm{Zelux}}$. Similar to the cross-calibration process described in Fig. 5.13, the Zelux frame lattice origin is scanned across a list of candidate positions to maximize the overlap to the inverted atom signal $\max(\mathbf{I}_{\mathrm{upper}}) - \mathbf{I}_{\mathrm{upper}}$. Black arrow and red arrows indicate orientations of the lattice vectors in each frame.

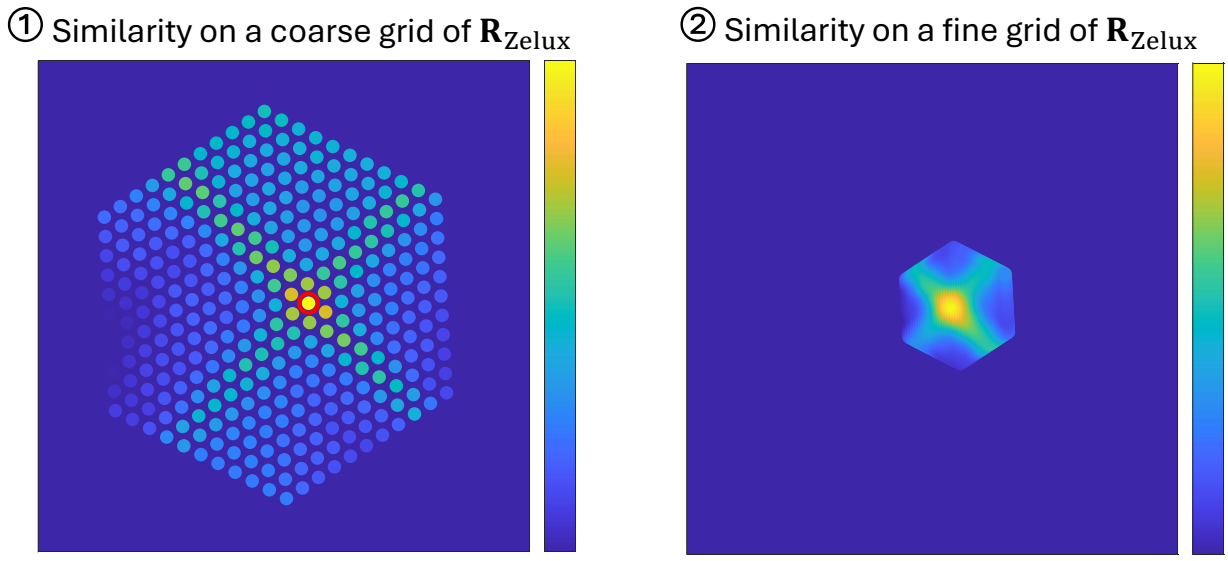

Figure 6.8: Two-stage offset calibration of the Zelux frame lattice origin. To accommodate potential achromatic shift, the candidate positions of $\mathbf{R}_{\text{Zelux}}$ is first scanned at the lattice site centers in stage ①, and at each position, a similarity score is computed. After the first scan, $\mathbf{R}_{\text{Zelux}}$ is set to the position which results in maximum similarity (red circle). Then the position is scanned across a finer grid with spacing of 0.1 lattice site around the current $\mathbf{R}_{\text{Zelux}}$ in stage ② and the position with maximized similarity score is used as the final $\mathbf{R}_{\text{Zelux}}$.

record the lattice pattern on the Zelux camera to monitor the lattice phase. After the atoms are transported to the glass cell, fluorescence images of atoms trapped in the triangular lattice are acquired using both the upper and lower CCDs. From these images, we extract the lattice site positions in all three imaging frames: upper CCD and lower CCD from atom fluorescence images, and Zelux from the direct image of the lattice pattern. From the static DMD pattern image, we determine the positions on the Zelux camera corresponding to specific DMD tweezer pixels. By tracking these reference points and mapping all measurements to a common lattice coordinate system, we quantify the relative position drift over the course of approximately three hours.

This characterization indicates that the lattice phase observed in the upper CCD atom images remains stable to within <0.1 lattice site over the course of several hours. This level of passive stability is expected, as the lattice is projected through the same objective used for imaging; thus, any mechanical drift of the objective does not result in relative motion between the lattice and the upper CCD image. Therefore, we expect that after warming up the system, a full calibration is necessary only on a daily basis. For images obtained from the lower optical paths, we observed a drift of approximately 0.5 lattice site over the course of three hours. Moreover, the drifts measured on the lower CCD and the Zelux camera are highly correlated, suggesting that the dominant source of drift is the relative motion between the two objectives.

6.3.3 Single-site addressing with DMD

Once the DMD coordinate frame has been fully calibrated, it becomes possible to design and project patterns that precisely address specific lattice sites. Using the same modulation sequence employed for atom removal during the calibration procedure (Fig. 6.7), we demonstrate selective removal of atoms along lattice vectors or at individual sites, as shwon in Fig. 6.10. While projecting a modulated pattern provides information about the effective

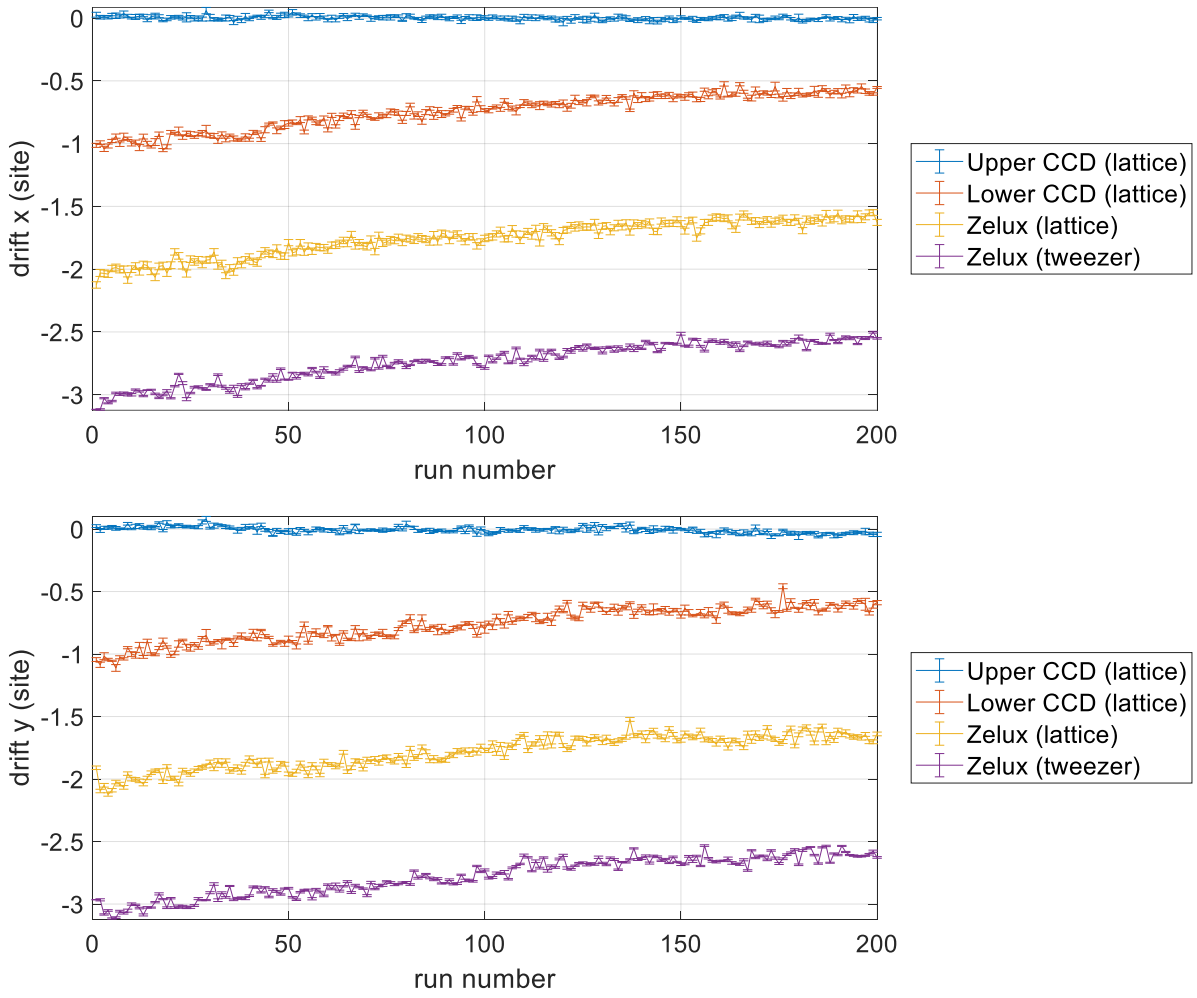

Figure 6.9: Monitoring the relative drift of optical traps. The lattice phase is extracted via Fourier analysis from atom images acquired by the upper and lower CCDs, as well as from a direct image of the lattice captured by the Zelux camera. The projected tweezer positions are independently tracked using additional images from the Zelux camera. Both lattice and tweezer positions are monitored over 200 experimental runs, with approximately one-minute intervals between successive runs. For visual clarity, the initial trap positions are vertically offset for each camera. For the lattice phase, the error bars represent the standard deviation of fitted positions across four quadrants of the image. For the tweezer positions, the error bars indicate the standard deviation across all tweezers within the image frame.

projection resolution on the atoms, it can also induce excess heating and atom loss outside the intentionally illuminated ("bright") regions, thereby degrading the observed pattern fidelity.

The site-resolved atom removal sequence can also be used to assess the precision of the DMD frame calibration. To do this, a series of line patterns aligned along a lattice vector are generated and offset by varying pixel amounts. These patterns are then projected onto the atoms while modulating the intensity. The resulting atom distributions are analyzed to extract the effective projection resolution. When the projected line is precisely aligned with the underlying lattice, the modulation effect on the atoms is expected to be the most spatially localized.

6.3.4 Single atoms loading into DMD trapping patterns

In addition to removing atoms at selected lattice sites, we have also made preliminary attempts to load single atoms into arrays of projected optical tweezers located at lattice sites (Fig. 6.11). Since the DMD tweezers are blue-detuned which applies repulsive forces on atoms, the trapping pattern is an array of black holes on a white background. The current sequence to load single atoms involves three steps:

1. **Transfer atoms from lattice and light sheet to blue-detuned tweezers**. We begin by projecting a static trapping pattern on the DMD, consisting of an array of black filled circles with a radius of 5 DMD pixels (approximately half the width of a lattice site), and spaced by 5 lattice sites. To transfer atoms into the blue-detuned DMD tweezers, we ramp up the tweezer intensity to full power and shortly after the intensity reaches the maximum, we ramp down the lattice and light sheet intensities to zero.

2. **Remove excess atoms by lowering tweezers trap depth**. Because atoms outside the intended tweezer sites can still be trapped by intensity ripples in the bright (white)

regions of the projected pattern, it is necessary to lower the overall trap power to remove these residual atoms. In the sequence, we lower the tweezwers trap depth and hold for about 30 ms to let the excess atoms escape from the potentials.

3. **Load atoms from tweezers back to the lattice for site-resolved imaging**. We ramp up the lattice and light sheet to full power and then ramp down the tweezers to zero to transfer atoms back to the lattice for site-resolved imaging.

We observed that when projecting larger trapping patterns, such as black filled circles with radii spanning more than one lattice site, the resulting tweezers are not sufficiently strong to support atoms against gravity. This is attributed to the reduced axial confinement in broader traps, as tightly focused tweezers provide stronger confinement along the beam's propagation direction. Under the current procedure, the atom loading probability across the array is highly inhomogeneous, with a maximum observed probability of 25% at specific sites. This inhomogeneity likely arises from a combination of the Gaussian intensity profile of the trapping laser on the DMD and spatial variations in cooling and imaging efficiency within the lattice.

To address this, a modified trapping design based on "donut"-shaped tweezers projected on a dark background may be employed. This configuration reduces confinement in the interstitial regions between traps, facilitating more effective removal of unwanted atoms without requiring a significant reduction in trap depth during the loading sequence. Such an approach may help preserve loaded atoms across a broader range of tweezer sites and improve overall loading uniformity.

6.4 Transporting atoms with moving patterns

With the real-time pattern streaming protocol described in Fig. 6.2, we can project a series of moving patterns to transport atoms. An example of transporting a cluster of atoms using

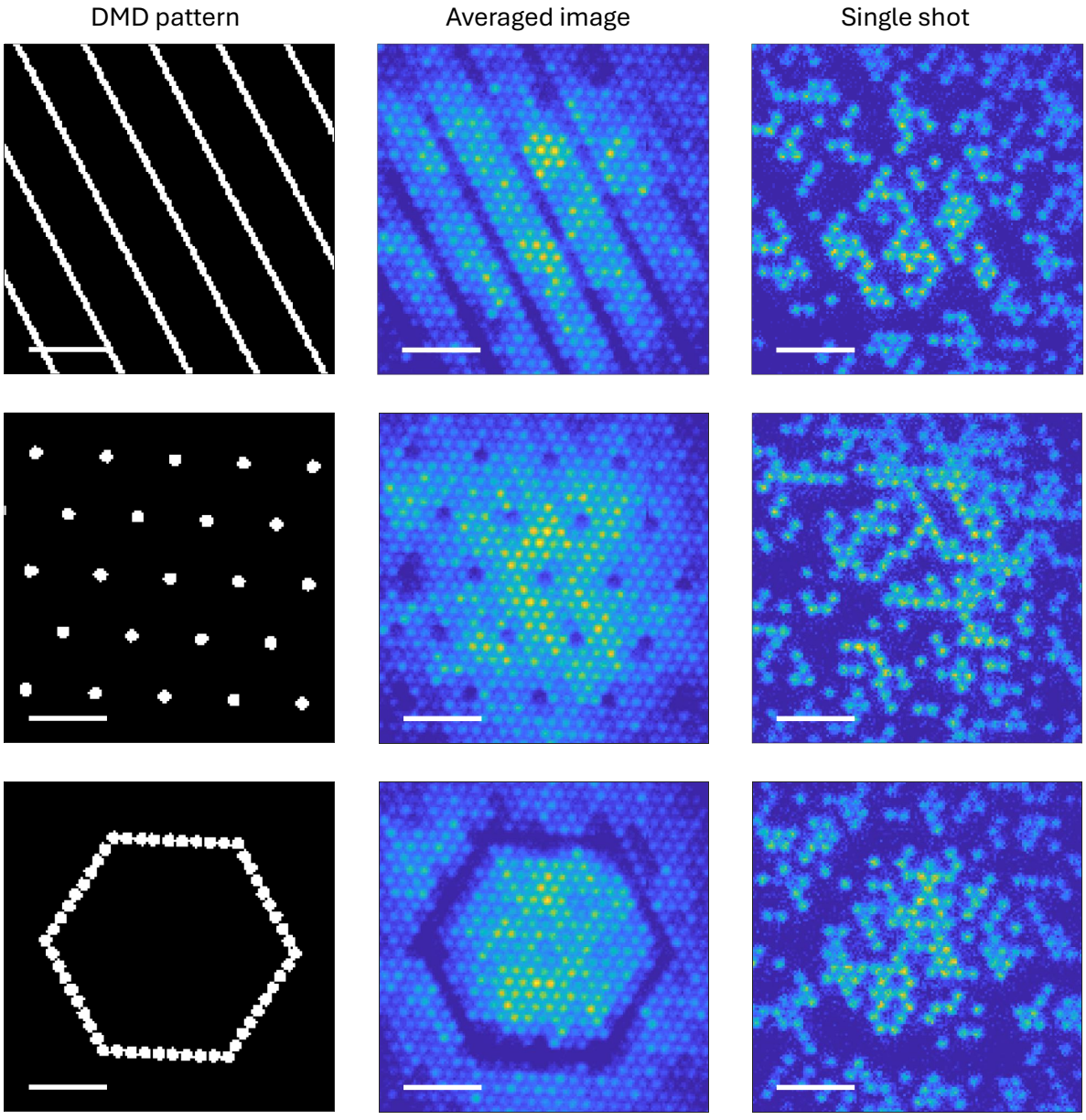

Figure 6.10: Removing atoms in the lattice with DMD projected pattern. The DMD pattern images (first column) are transformed into the coordinate system of the atom images shown in the second and third columns. Scale bar is 5 μm in all images.

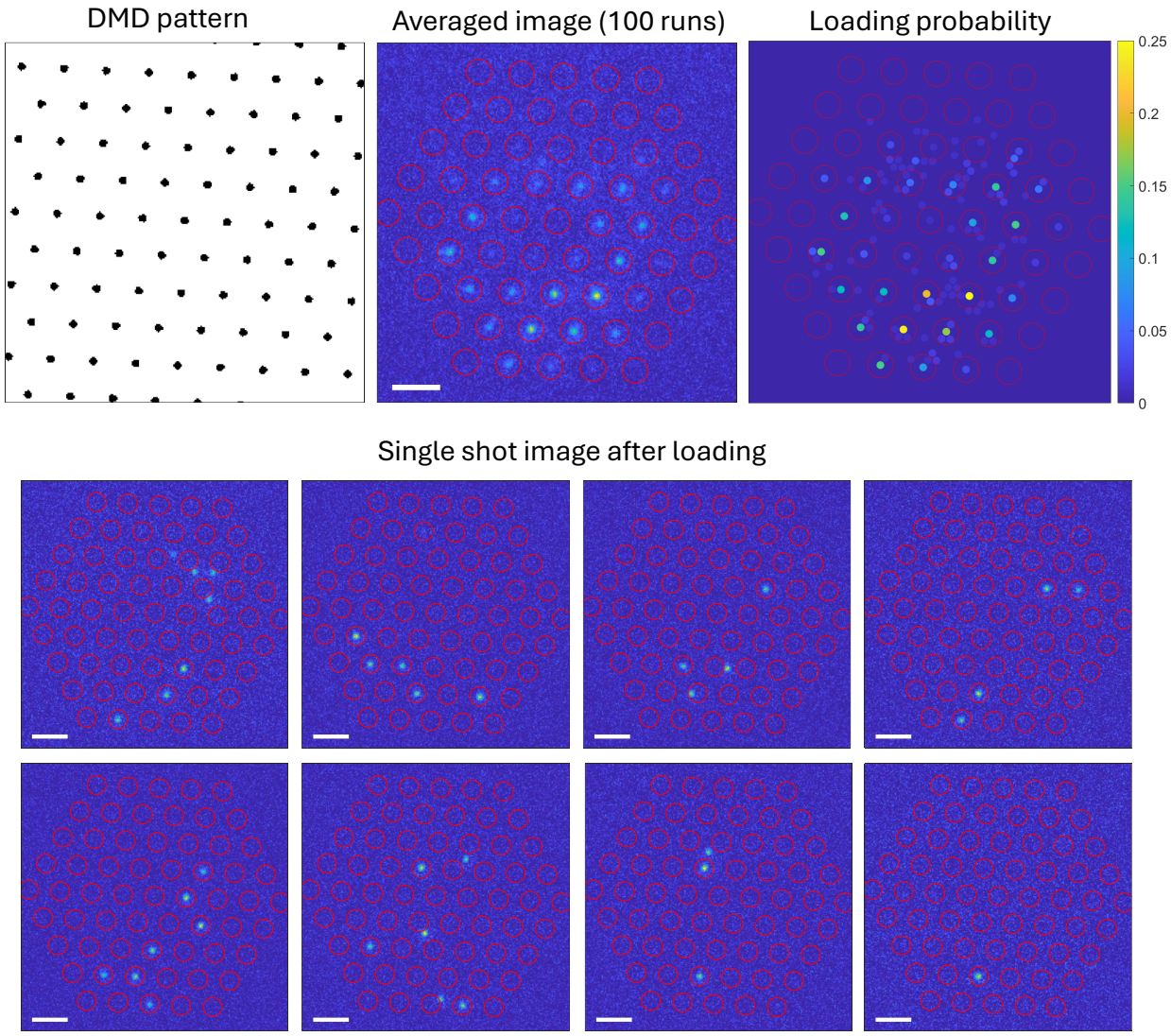

Figure 6.11: Loading single atoms into projected tweezers. Red circles are centered at the expected tweezers positions with a radius of 1.5 lattice sites. The tweezers have a radius of about half a lattice site and the spacing between adjacent tweezers is 5 lattice sites. Scale bar is 5 μm in all images.

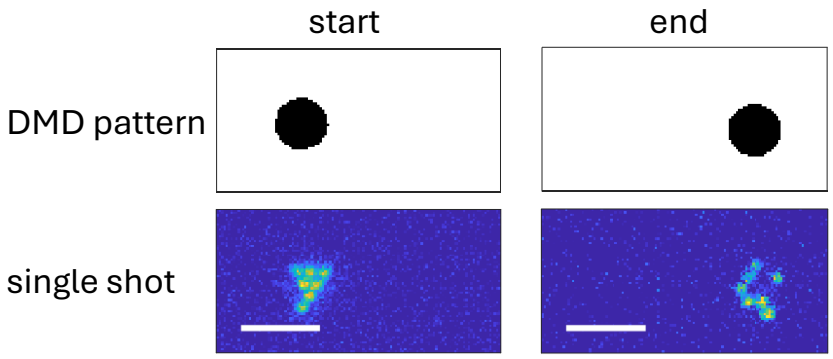

Figure 6.12: Transporting a cluster of atoms with streamed moving patterns. The pattern is a black circle with a radius of 20 DMD pixels (approximately 2 lattice sites) and the distance between start and end positions is 9 lattice sites. Scale bar is 5 μm in all images.

projected tweezers is shown in Fig. 6.12. After loading atoms into a blue-detuned tweezer and ramping the lattice depth to zero, the projected pattern is dynamically updated in real time to move the trap by 9 lattice sites. In this demonstration, the tweezer pattern consists of a black filled circle with a radius of 20 DMD pixels, corresponding to approximately two lattice sites.

When multiple atoms are loaded into the same trap, the lack of internal confinement within the circular pattern means that the relative arrangement of atoms is not preserved during transport. Furthermore, light-assisted collisions during the second imaging step contribute to additional atom loss. These issues won't be present in the case of single-atom transport. There are ongoing experiments aiming to demonstrate controlled transport of individually loaded atoms using projected tweezers, starting from initial configurations such as those shown in Fig. 6.11.

CHAPTER 7

CONCLUSION & OUTLOOK

In the previous chapters, we discuss the design and construction of the QMS apparatus, the optical trapping, cooling and site-resolved imaging in a triangular lattice, and the implementation of a DMD-based dynamic tweezer arrays to address single atoms with real-time control.

This chapter briefly outlines the remaining steps required to complete the QMS: characterization and optimization of single atom loading and transport efficiency, development and integration of atom sorting algorithm, and efficient cooling to reach motional ground-state in the lattice.

7.1 Optimization of single atom loading and transport

We aim to perform atom rearrangement operations selectively on "misplaced" atoms, while keeping the remaining atoms confined in the optical lattice. The implementation of this procedure requires low atomic temperatures and a sufficiently deep tweezer potential, both relative to the lattice trap depth. In the current configuration, the atom temperature is approximately 10 μK and lattice depth is around 120 μK (Fig. 2.6), which implies that a tweezer trap depth on the order of 1 mK would be necessary to ensure robust confinement during rearrangement. However, based on the available laser power, beam parameters and the atomic polarizability at 532 nm (Tab. 2.1), the achievable tweezer depth is estimated to be only around 100 μK. In our initial experiments on atom transport (Fig. 6.12), the lattice was ramped to zero to facilitate motion. However, for future implementations of selective rearrangement where only specific atoms are moved while others remain trapped in the lattice, deeper tweezer potentials will be preferred to ensure robust confinement and minimize perturbation to stationary atoms. One potential workaround is to switch the tweezer wave-

length from 532 nm to 780 nm. At 780 nm, the atomic polarizability is significantly higher, allowing for deeper optical traps. Additionally, high power diode lasers are readily available at this wavelength, and the anti-reflective coatings on our imaging optics are expected to be compatible with 780 nm light.

In addition to experimental upgrades, a careful simulation of the expected vibrational heating under various trap configurations and transport trajectories will be valuable for guiding the next stage of the experiment. Such optimization could be performed from first-principle modeling as described in Ref. [93], or through empirical strategies that leverage machine learning to optimize control parameters [132, 133, 134].

The efficiency of single-atom loading and transport from an optical lattice can be systematically characterized and optimized by varying the design of the trapping potential and the transport trajectories. For the trapping potential, the objective is to maximize single-atom loading efficiency while minimizing crosstalk and perturbations to adjacent lattice sites. To further enhance spatial selectivity, detailed characterization and correction of optical aberrations in the tweezer projection path may be necessary, following procedures similar to those described in Ref. [95]. For transport optimization, the goal is to suppress vibrational heating and atom loss during motion across a rugged lattice potential landscape. The effectiveness of a given transport protocol can be quantified by the retention rate of atoms following the transport process.

7.2 Atom sorting with a parallel multi-tweezer algorithm

A key advantage of SLM-based dynamic tweezers is that each tweezer can be independently controlled, enabling the implementation of more time-efficient atom-sorting algorithms. In particular, algorithms such as the Hungarian algorithm can be used to compute optimal atom-to-site assignments that minimize the total transport distance and duration [113]. Moreover, recent advances demonstrate the potential of incorporating artificial intelligence

(AI) to design control strategies that optimize rearrangement fidelity [116].

7.3 Efficient ground state cooling in the lattice

Efficient ground-state cooling is essential for reaching quantum degeneracy in densely packed atomic arrays [135]. To overcome the limitations of the current cooling scheme, we are implementing electromagnetically induced transparency (EIT) cooling, following approaches similar to those demonstrated in [43]. As an alternative, resolved Raman sideband cooling has also been shown to effectively cool single atoms to their motional ground state [79].

APPENDIX A

OPTICAL DESIGN FOR 2D LATTICE

We use Zemax OpticStudio to simulate the propagation of the off-axis lattice beams through the imaging system (Fig. A.1). The sizes and directions of the beams are carefully engineered to produce the target beam size and an intersection angle of 45° at the atom plane. The part numbers of the lenses can be found in Fig. 5.2. The simulation assumes the parameters listed in Tab. A.1. The beam parameters at different checkpoints are listed in Tab. A.2 for reference. Note that the collimator position is set to obtain a target beam size at the atom plane, which may not result in a collimated fiber output. In practice, the collimator can be slightly adjusted around the current position to achieve different lattice beam size at the objective focus.

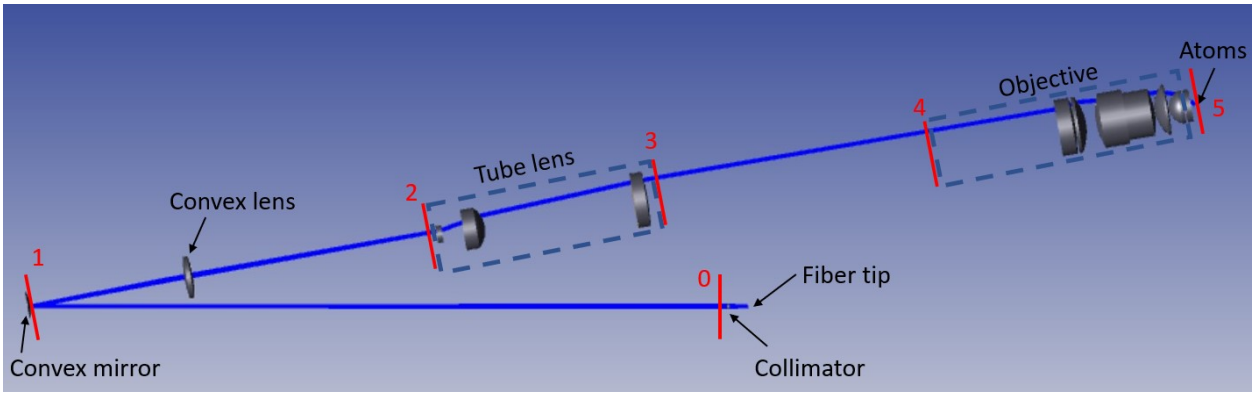

Figure A.1: Zemax model for simulating lattice beam parameters along the beam path

Position	Parameters
Fiber tip	Beam waist is 3.8μm
Collimator	Fiber to collimator distance is 17.6 mm
Convex mirror	Collimator to convex mirror distance is 650 mm
Convex lens	Convex mirror to convex lens distance is 145.7 mm
Tube lens	Convex lens to tube lens (first optics) distance is 231 mm

Table A.1: Parameters for the Zemax simulations

Position	Beam size (mm)	Off-axis distance (mm)	Beam angle (°)
collimator output	1.487	0	0
before convex mirror	0.211	1.84	-9.68
after convex lens	2.47	1.5	0.267
before tube lens first optics	0.353	3.29	0.442
after tube lens last optics	0.701	17.8	0.00
before objective first optics	0.305	17.8	0.00
atom plane	0.046	0.00	-45.0

Table A.2: Lattice beam parameters at various checkpoints. The sign of beam angle is defined such that converging to axis is negative.

APPENDIX B

ALIGNMENT PROCEDURE OF 2D LATTICE

Proper alignment ensures significant overlap among the lattice beams, resulting in deeper and more symmetric optical potentials that are essential for both cooling and imaging.

The alignment of lattice beams follows three general steps:

1. **Coarse alignment on the vertical breadboard.** Using the two mirrors in each beam path, the three beams are aligned to their expected position at the back of the vertical breadboard with one laser-cut alignment target at the intersection point and another target flushed to the back of the vertical breadboard. The drawings of the alignment target is provided in Fig. B.1.

2. **Alignment of the three lattice beams to the upper tube lens.** We begin by placing a 2-inch iris immediately after the upper tube lens and centering it along the optical axis of the tube lens. Assuming the rest of the system is pre-aligned, the position of the lattice beams can be monitored using the lower CCD. We then iteratively adjust the two 2-inch steering mirrors (M1 and M2, as labeled in Fig. 5.2) to ensure that all three lattice beams are symmetrically clipped by the iris aperture and converge at the desired target position on the lower CCD.

3. **Fine alignment of the three lattice beams individually.** After aligning the common path, we adjust the two mirrors in each individual path to maximize the spatial overlap of the three beams at atom plane.

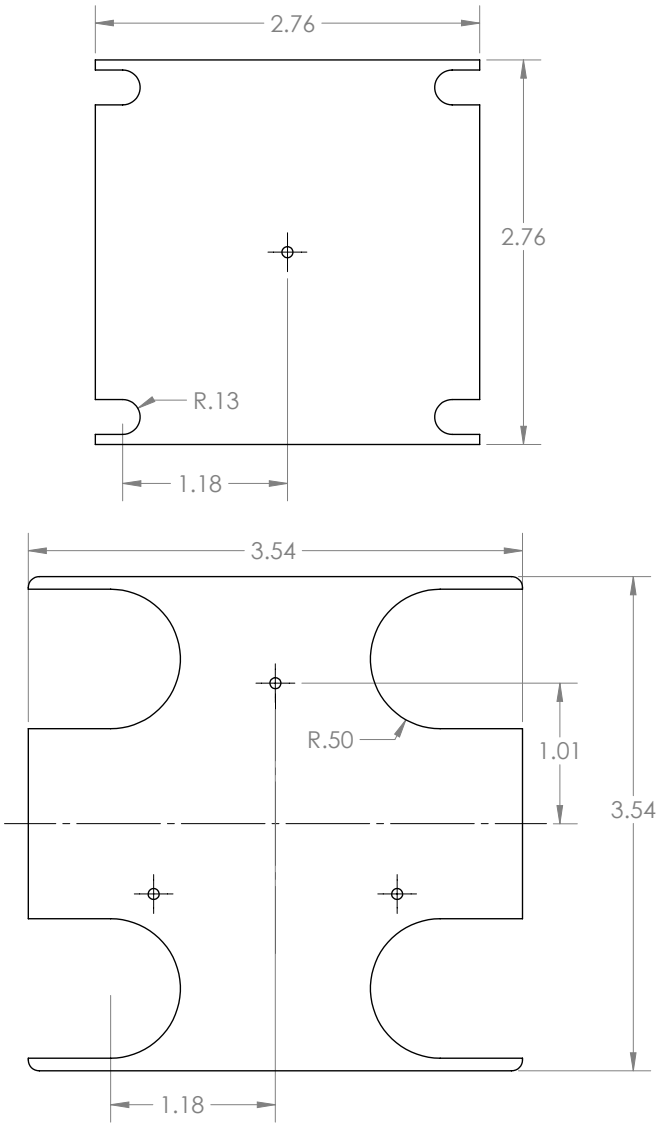

Figure B.1: Drawings of the alignment targets for aligning lattice beams. The upper target is placed at the intersection point and the lower target is flushed against the back surface of the vertical breadboard.

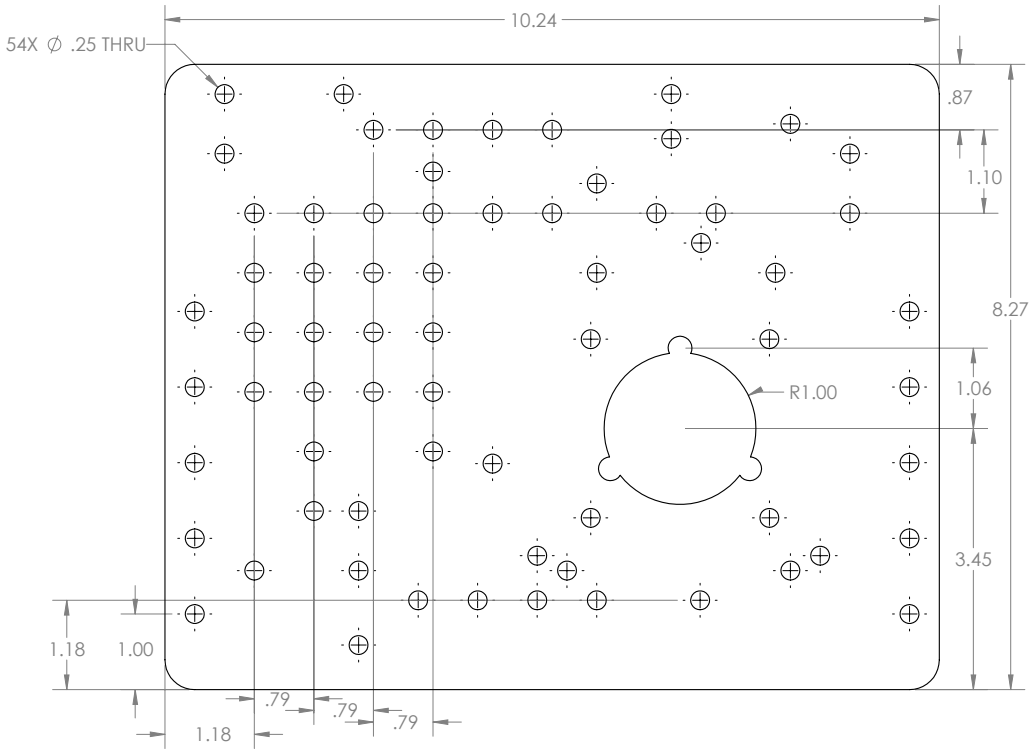

Figure B.2: Mechanical drawing of the custom-machined vertical breadboard. Not all dimensions are shown.

APPENDIX C

ALIGNMENT OF DMD TO THE OPTICAL SYSTEM

To address specific lattice sites with high spatial resolution, it is crucial to maintain precise alignment between the DMD and the upper imaging system. In addition, the other trapping potentials (the 2D optical lattice and the light sheet) must be properly aligned to ensure that the center of the atomic cloud coincides with the center of the DMD projection. We have found that the following steps can usually produce a good alignment of the system:

1. **Alignment of 532 nm laser beam to the center of the DMD chip**. This is done by displaying a "centered" pattern on the DMD and adjusting the two steering mirrors positioned before the DMD such that the intensity distribution of the reflected pattern appears to be symmetric around the center.

2. **Alignment the DMD to the upper tube lens**. This is accomplished by adjusting the two steering mirrors between DMD chip and the upper tube lens. The alignment should center the output beam on the aperture of the tube lens and overlap all the internal reflections from the tube lens optics with the incident beam path.

3. **Alignment of the lower imaging path with DMD as a reference**. Once DMD is aligned to the upper system, we first set the DMD pattern to a centered spot, usually with a radius of 50 pixels in DMD space, and then align the two steering mirrors in between lower objective and lower tube lens such that the DMD reflected beam is simultaneously centered and normal to the lower tube lens surface. The mirrors between the lower tube lens and the lower CCD/Zelux camera are also aligned with the DMD reference beam.

4. **Mark DMD position on the lower CCD**. When the lower imaging path is aligned, we run the sequence to image lattice-trapped atoms and poke a hole on the cloud with

DMD. The position of the hole on the image marks the position of the DMD center, which we will use to perform fine adjustment of lattice beams.

5. **Fine alignment of lattice beam position**. If the lattice trapped atoms are not centered with the DMD pattern, we will then use the two 2" mirrors between the lattice breadboard and the upper tube lens to steer the lattice beams such that the lattice position matches the DMD center. While looking at the single site images of atoms, we first make a fine adjustment on the 2" mirror that is closer to the tube lens such that the atoms are moved to the DMD center. We later use the other 2" mirror to adjust the beam pointing such that the three lattice beams are still symmetrically clipped by a centered iris after the upper tube lens. The beam walking should converge to a point such that the atom cloud center coincides with the DMD center position on the lower CCD and the lattice beams still look symmetric and are not clipped in the beam path.

6. **Fine alignment of the light sheet position**. If the atom density looks not aligned with the previously marked DMD center position, we may need to adjust the light sheet to align the trap center to the DMD reference. This is done by using a compression sequence where the lattice power is ramped down to zero and ramped back up before imaging. During this compression sequence, atoms originally at the outer side of the light sheet potential will fall to the center, therefore the atom image after this procedure is a good indication of the light sheet horizontal alignment. We use the atom image as a reference and adjust the horizontal mirror knob of the last light sheet steering mirror, as well as the translation stage position of the final lens to align the light sheet center to the DMD center.

The above alignment procedure is usually sufficient to bring all trapping potentials (DMD, lattice, light sheet) to the optical axis of the objectives. However, the axial alignment of all cameras (upper CCD, lower CCD, Zelux monitoring camera) and projection device (DMD)

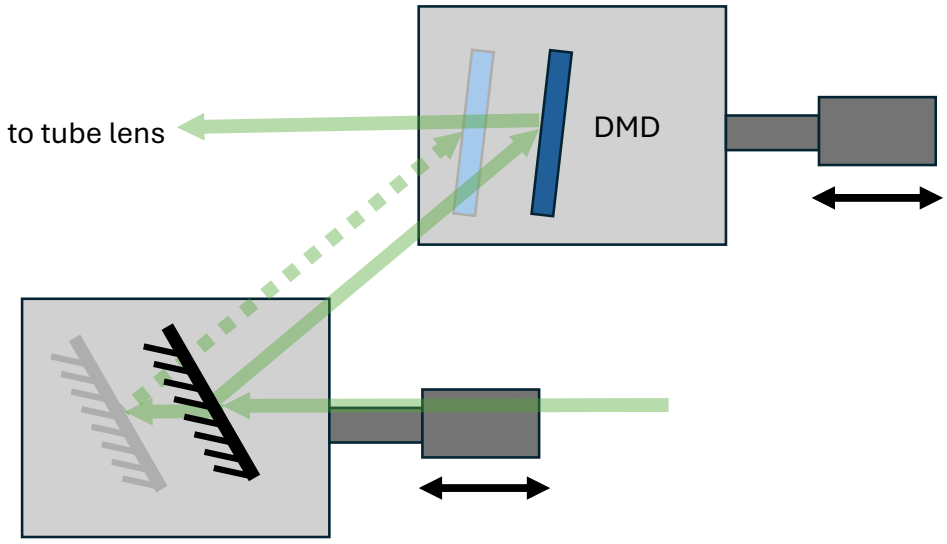

Figure C.1: Alignment of DMD axial position. The DMD chip and the mirror before it are mounted on translation stages. To move the position of DMD along the optical axis, we can translate both stages by the same amount.

still needs to be set correctly to be at the corresponding image plane of atom position. The procedure to align the axial positions of the devices is provided as follows:

1. **Alignment of the two Andor CCDs axial position**. We first use the four picomotor-controlled mirror knobs to focus the atom image on both upper and lower CCD, and then check the image magnification by performing lattice calibration on both frames. If the upper image and lower image have significantly different magnification than specified by the system (around 87), we then move the camera position along the optical axis with a translation stage. After this alignment, the upper and lower atom imaging path should be almost symmetric.

2. **Alignment of DMD's axial position**. When the upper objective and light sheet heights are set such that both CCDs have good atom imaging resolution, we project a pattern on the DMD to modulate and remove atoms and then adjust the axial position of the DMD to optimize the projected pattern resolution. The axial position

adjustment is done by using two translation stages as shown in Fig. C.1. After this alignment, we should be able to simutaneously get a good imaging resolution from the upper CCD and a good projection resolution from the DMD.

3. **Alignment of Zelux camera axial position**. Once the upper objective and light sheet heights are set to focus atom images, we align the Zelux camera axial position to focus the re-imaged DMD pattern.

We noticed that the single site addressing performance of the DMD projected pattern is very sensitive to the defocus aberration. A more careful characterization may be necessary to characterize the precision of the current axial alignment. The characterization can be done by scanning the upper objective height, and at each height, collect atom images on both CCDs and the re-imaged DMD patterns on the Zelux camera. If the images are taken after a modulated DMD pulse, we can extract both the projection resolution of DMD and the imaging resolution of upper CCD from the images. Then we can determine the optimal upper objective height to achieve the best imaging resolution, as well as the optimal height for the best projection resolution. When the DMD axial position is set correctly, those two positions should coincide, meaning that the optimal imaging and projection are achieved simutaneously. Otherwise, the discrepancy can inform which way the DMD should be adjusted. Note that this process should be performed when the system is thermally stable such that the induced defocus is mainly from the objective height setting.

APPENDIX D

ZEMAX SIMULATION OF ABERRATIONS

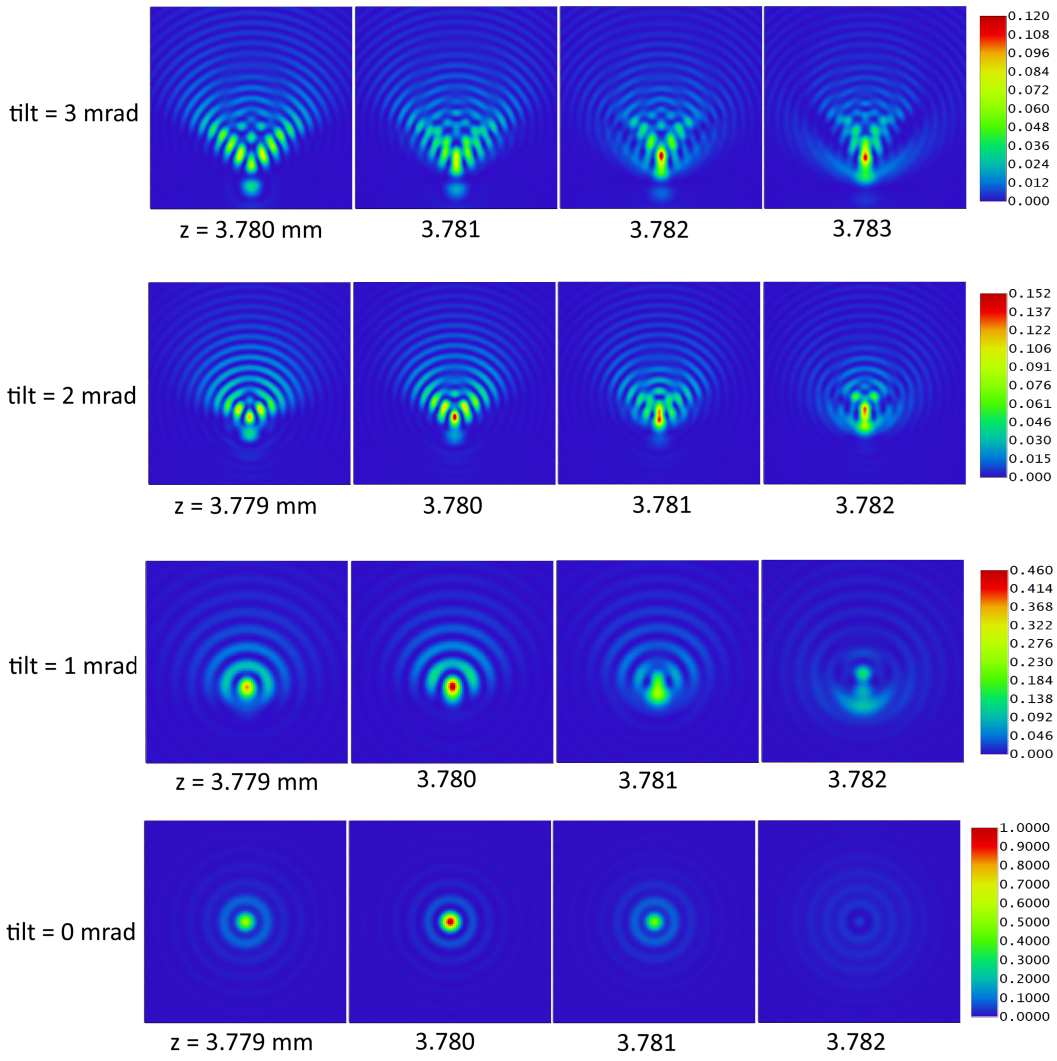

Figure D.1: Zemax simulation of aberration induced by tilt angle of glass cell window. Plots from left to right show the evolution of simulated point-spread function (PSF) of the system at varying object positions along the z-axis. Plots from top to bottom show the PSF of the system at different tilt angles. The designed focal length is $z = 3.78$ mm and variations in the z-position correspond to different defocus in the image plane.

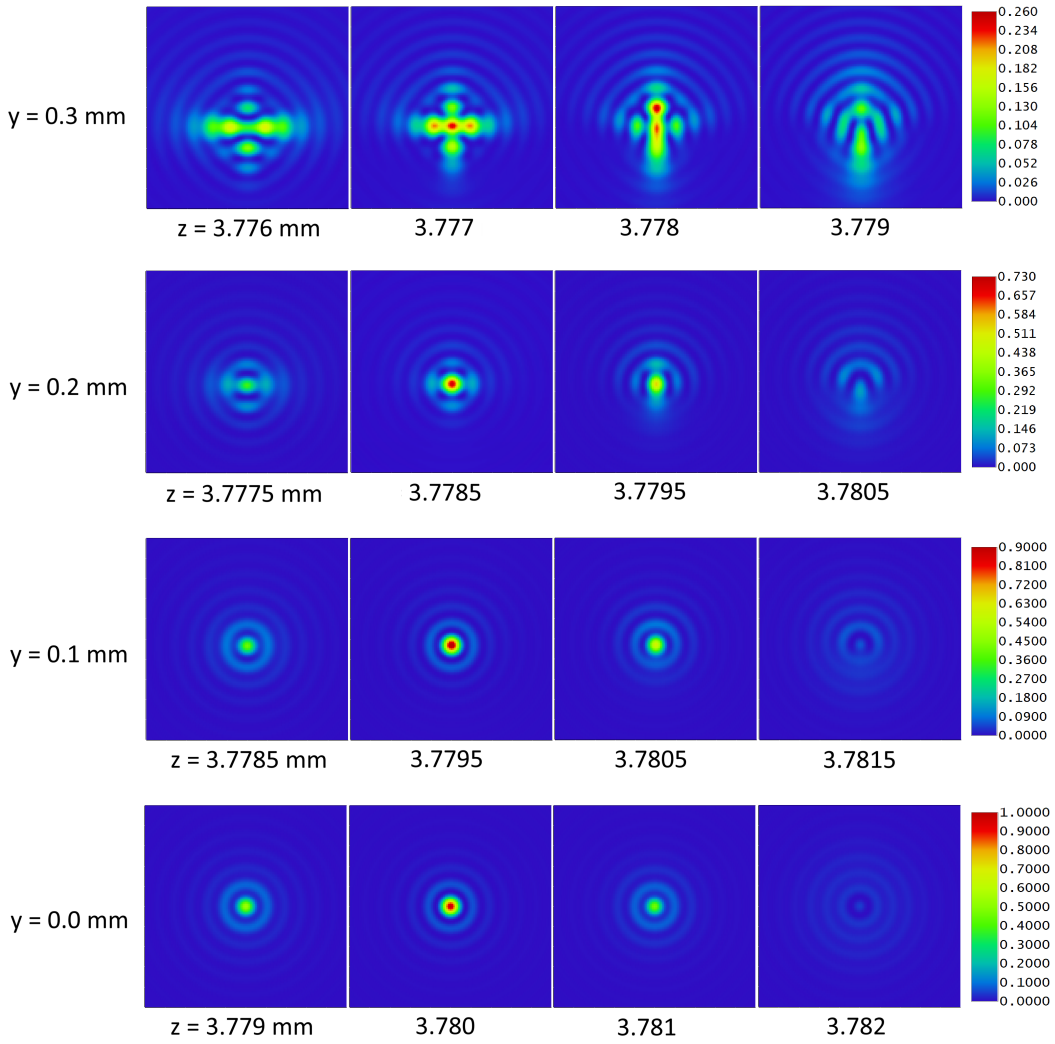

Figure D.2: Zemax simulation of aberration induced by imaging outside of field of view. Plots from left to right show the evolution of simulated point-spread function (PSF) of the system at varying object positions along the z-axis. Plots from top to bottom show the PSF of the system at different horizontal position. The designed focal length is $z = 3.78$ mm and variations in the z-position correspond to different defocus in the image plane. The objective is designed for a field of view of 0.1 mm.

APPENDIX E

DESIGN OF UPPER OBJECTIVE HOLDER

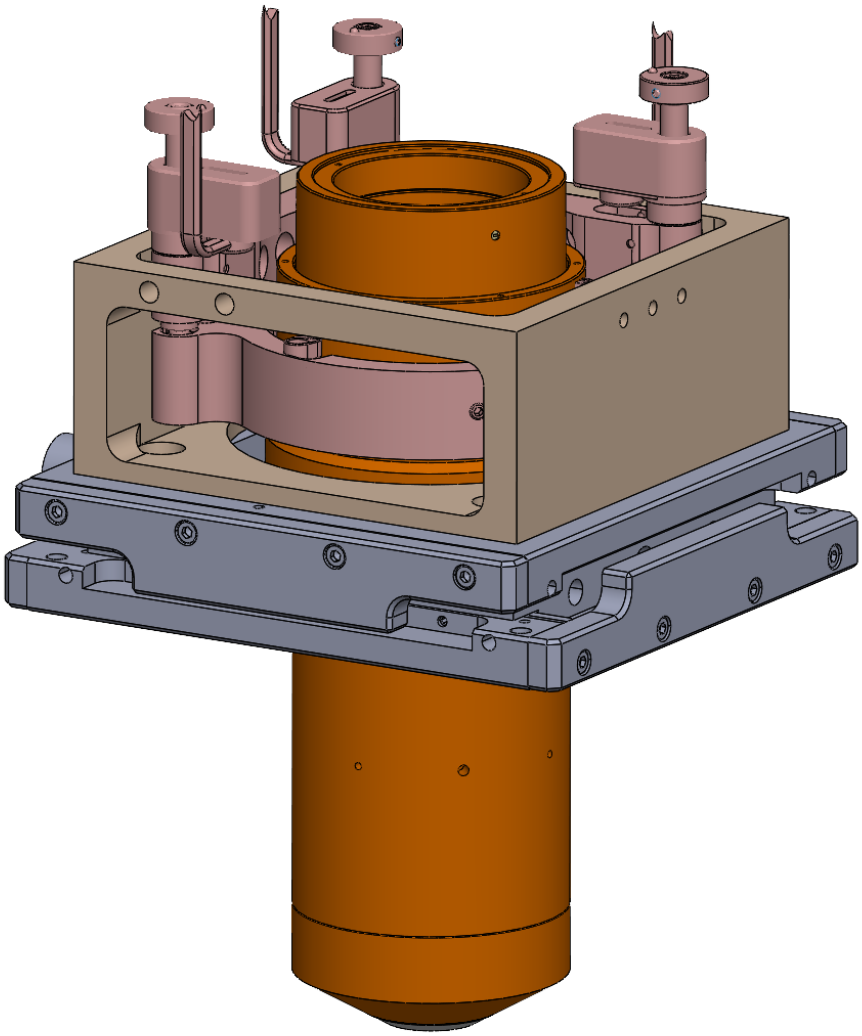

Figure E.1: Illustration of updated design of upper objective holder with piezo actuators

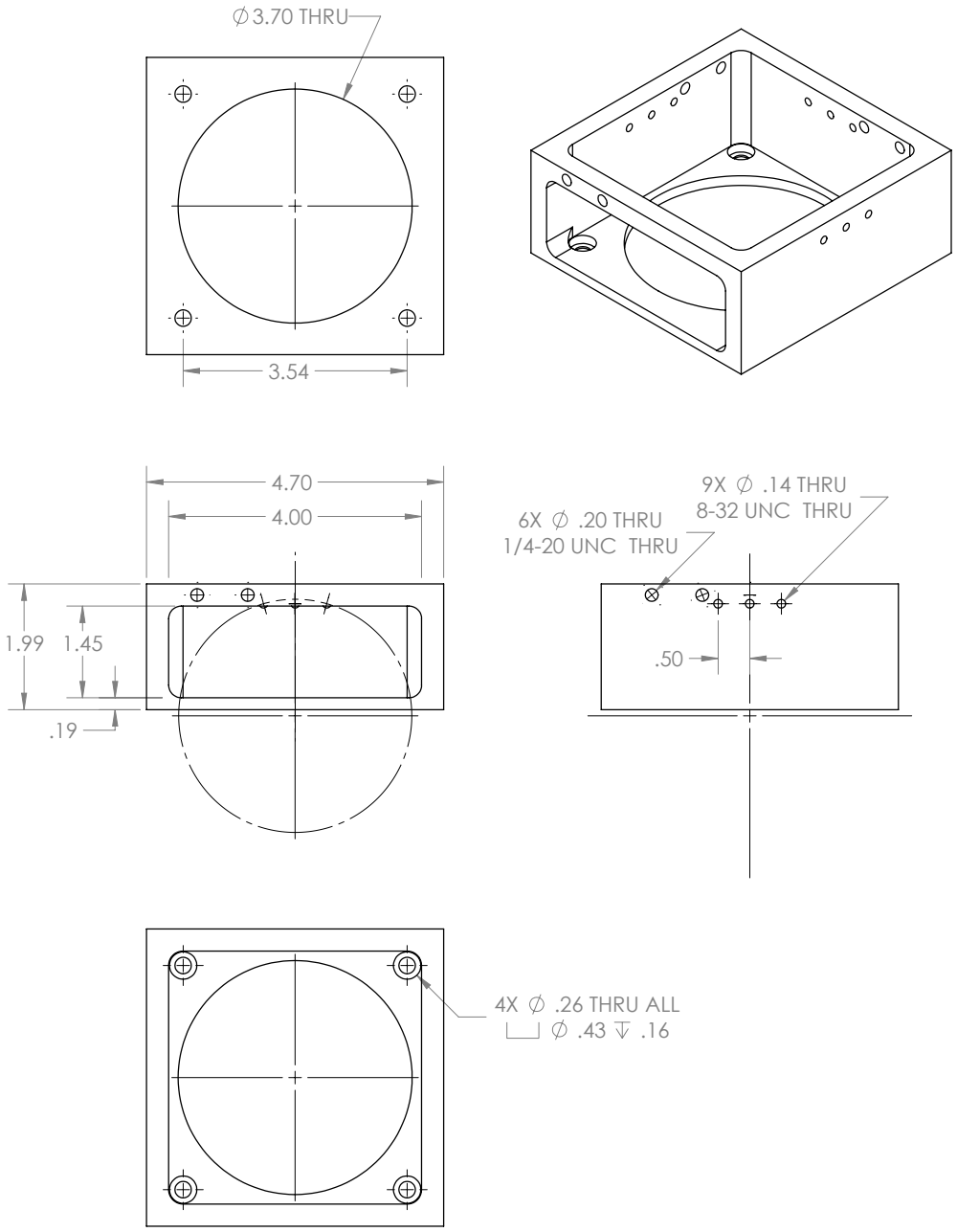

Figure E.2: Mechanical drawings of the upper objective mirror mount holder. The curved edges are solely to facilitate machining. All dimensions are given in inches.

REFERENCES

[1] Immanuel Bloch, Jean Dalibard, and Sylvain Nascimbene. Quantum simulations with ultracold quantum gases. *Nature Physics*, 8(4):267–276, 2012.

[2] Mike H Anderson, Jason R Ensher, Michael R Matthews, Carl E Wieman, and Eric A Cornell. Observation of bose-einstein condensation in a dilute atomic vapor. *science*, 269(5221):198–201, 1995.

[3] Kendall B Davis, M-O Mewes, Michael R Andrews, Nicolaas J van Druten, Dallin S Durfee, DM Kurn, and Wolfgang Ketterle. Bose-einstein condensation in a gas of sodium atoms. *Physical review letters*, 75(22):3969, 1995.

[4] Curtis Charles Bradley, CA Sackett, and RG Hulet. Bose-einstein condensation of lithium: Observation of limited condensate number. *Physical Review Letters*, 78(6): 985, 1997.

[5] Cheng Chin, Rudolf Grimm, Paul Julienne, and Eite Tiesinga. Feshbach resonances in ultracold gases. *Reviews of Modern Physics*, 82(2):1225–1286, 2010.

[6] Logan W Clark, Lei Feng, and Cheng Chin. Universal space-time scaling symmetry in the dynamics of bosons across a quantum phase transition. *Science*, 354(6312): 606–610, 2016.

[7] Zhendong Zhang, Shu Nagata, Kai-Xuan Yao, and Cheng Chin. Many-body chemical reactions in a quantum degenerate gas. *Nature Physics*, 19(10):1466–1470, 2023.

[8] Krutik Patel, Geyue Cai, Henry Ando, and Cheng Chin. Sound propagation in a bose-fermi mixture: From weak to strong interactions. *Physical Review Letters*, 131 (8):083003, 2023.

[9] Iulia M Georgescu, Sahel Ashhab, and Franco Nori. Quantum simulation. *Reviews of Modern Physics*, 86(1):153–185, 2014.

[10] Muqing Xu, Lev Haldar Kendrick, Anant Kale, Youqi Gang, Chunhan Feng, Shiwei Zhang, Aaron W Young, Martin Lebrat, and Markus Greiner. A neutral-atom hubbard quantum simulator in the cryogenic regime. *arXiv preprint arXiv:2502.00095*, 2025.

[11] Chen-Lung Hung, Victor Gurarie, and Cheng Chin. From cosmology to cold atoms: observation of sakharov oscillations in a quenched atomic superfluid. *Science*, 341 (6151):1213–1215, 2013.

[12] Lei Feng, Logan W Clark, Anita Gaj, and Cheng Chin. Coherent inflationary dynamics for bose–einstein condensates crossing a quantum critical point. *Nature Physics*, 14 (3):269–272, 2018.

[13] Jiazhong Hu, Lei Feng, Zhendong Zhang, and Cheng Chin. Quantum simulation of unruh radiation. *Nature Physics*, 15(8):785–789, 2019.

[14] Andreas Trabesinger. Quantum simulation. *Nature Physics*, 8(4):263–263, 2012.

[15] Steven Chu, Leo Hollberg, John E Bjorkholm, Alex Cable, and Arthur Ashkin. Three-dimensional viscous confinement and cooling of atoms by resonance radiation pressure. *Physical review letters*, 55(1):48, 1985.

[16] Florian Schreck and Klaasjan van Druten. Laser cooling for quantum gases. *Nature Physics*, 17(12):1296–1304, 2021.

[17] Ren Zhang, Yanting Cheng, Peng Zhang, and Hui Zhai. Controlling the interaction of ultracold alkaline-earth atoms. *Nature Reviews Physics*, 2(4):213–220, 2020.

[18] K Aikawa, A Frisch, M Mark, S Baier, A Rietzler, R Grimm, and F Ferlaino. Bose-einstein condensation of erbium. *Physical review letters*, 108(21):210401, 2012.

[19] Lincoln D Carr, David DeMille, Roman V Krems, and Jun Ye. Cold and ultracold molecules: science, technology and applications. *New Journal of Physics*, 11(5):055049, 2009.

[20] LR Liu, JD Hood, Yichao Yu, JT Zhang, NR Hutzler, Till Rosenband, and K-K Ni. Building one molecule from a reservoir of two atoms. *Science*, 360(6391):900–903, 2018.

[21] Manuel Endres, Hannes Bernien, Alexander Keesling, Harry Levine, Eric R Anschuetz, Alexandre Krajenbrink, Crystal Senko, Vladan Vuletic, Markus Greiner, and Mikhail D Lukin. Atom-by-atom assembly of defect-free one-dimensional cold atom arrays. *Science*, 354(6315):1024–1027, 2016.

[22] Daniel Barredo, Sylvain De Léséleuc, Vincent Lienhard, Thierry Lahaye, and Antoine Browaeys. An atom-by-atom assembler of defect-free arbitrary two-dimensional atomic arrays. *Science*, 354(6315):1021–1023, 2016.

[23] Christian Gross and Immanuel Bloch. Quantum simulations with ultracold atoms in optical lattices. *Science*, 357(6355):995–1001, 2017.

[24] Waseem S Bakr, Jonathon I Gillen, Amy Peng, Simon Fölling, and Markus Greiner. A quantum gas microscope for detecting single atoms in a hubbard-regime optical lattice. *Nature*, 462(7269):74–77, 2009.

[25] Jacob F Sherson, Christof Weitenberg, Manuel Endres, Marc Cheneau, Immanuel Bloch, and Stefan Kuhr. Single-atom-resolved fluorescence imaging of an atomic mott insulator. *Nature*, 467(7311):68–72, 2010.

[26] Lawrence W Cheuk, Matthew A Nichols, Melih Okan, Thomas Gersdorf, Vinay V Ramasesh, Waseem S Bakr, Thomas Lompe, and Martin W Zwierlein. Quantum-gas microscope for fermionic atoms. *Physical review letters*, 114(19):193001, 2015.

[27] Elmar Haller, James Hudson, Andrew Kelly, Dylan A Cotta, Bruno Peaudecerf, Graham D Bruce, and Stefan Kuhr. Single-atom imaging of fermions in a quantum-gas microscope. *Nature Physics*, 11(9):738–742, 2015.

[28] Maxwell F Parsons, Florian Huber, Anton Mazurenko, Christie S Chiu, Widagdo Setiawan, Katherine Wooley-Brown, Sebastian Blatt, and Markus Greiner. Site-resolved imaging of fermionic li 6 in an optical lattice. *Physical review letters*, 114(21):213002, 2015.

[29] Ryuta Yamamoto, Jun Kobayashi, Takuma Kuno, Kohei Kato, and Yoshiro Takahashi. An ytterbium quantum gas microscope with narrow-line laser cooling. *New Journal of Physics*, 18(2):023016, 2016.

[30] Sandra Buob, Jonatan Höschele, Vasiliy Makhalov, Antonio Rubio-Abadal, and Leticia Tarruell. A strontium quantum-gas microscope. *PRX Quantum*, 5(2):020316, 2024.

[31] Lin Su, Alexander Douglas, Michal Szurek, Robin Groth, S Furkan Ozturk, Aaron Krahn, Anne H Hébert, Gregory A Phelps, Sepehr Ebadi, Susannah Dickerson, et al. Dipolar quantum solids emerging in a hubbard quantum simulator. *Nature*, 622(7984): 724–729, 2023.

[32] Lysander Christakis, Jason S Rosenberg, Ravin Raj, Sungjae Chi, Alan Morningstar, David A Huse, Zoe Z Yan, and Waseem S Bakr. Probing site-resolved correlations in a spin system of ultracold molecules. *Nature*, 614(7946):64–69, 2023.

[33] Ryuta Yamamoto, Hideki Ozawa, David C Nak, Ippei Nakamura, and Takeshi Fukuhara. Single-site-resolved imaging of ultracold atoms in a triangular optical lattice. *New Journal of Physics*, 22(12):123028, 2020.

[34] Jin Yang, Liyu Liu, Jirayu Mongkolkiattichai, and Peter Schauss. Site-resolved imaging of ultracold fermions in a triangular-lattice quantum gas microscope. *PRX Quantum*, 2(2):020344, 2021.

[35] Philipp M Preiss, Ruichao Ma, M Eric Tai, Jonathan Simon, and Markus Greiner. Quantum gas microscopy with spin, atom-number, and multilayer readout. *Physical Review A*, 91(4):041602, 2015.

[36] Joannis Koepsell, Sarah Hirthe, Dominik Bourgund, Pimonpan Sompet, Jayadev Vijayan, Guillaume Salomon, Christian Gross, and Immanuel Bloch. Robust bilayer charge pumping for spin-and density-resolved quantum gas microscopy. *Physical Review Letters*, 125(1):010403, 2020.

[37] Markus Greiner, Olaf Mandel, Tilman Esslinger, Theodor W Hänsch, and Immanuel Bloch. Quantum phase transition from a superfluid to a mott insulator in a gas of ultracold atoms. *nature*, 415(6867):39–44, 2002.

[38] Philip Zupancic, Philipp M Preiss, Ruichao Ma, Alexander Lukin, M Eric Tai, Matthew Rispoli, Rajibul Islam, and Markus Greiner. Ultra-precise holographic beam shaping for microscopic quantum control. *Optics express*, 24(13):13881–13893, 2016.

[39] Simon Stellmer, Benjamin Pasquiou, Rudolf Grimm, and Florian Schreck. Laser cooling to quantum degeneracy. *Physical review letters*, 110(26):263003, 2013.

[40] Jiazhong Hu, Alban Urvoy, Zachary Vendeiro, Valentin Crépel, Wenlan Chen, and Vladan Vuletić. Creation of a bose-condensed gas of 87rb by laser cooling. *Science*, 358(6366):1078–1080, 2017.

[41] Alban Urvoy, Zachary Vendeiro, Joshua Ramette, Albert Adiyatullin, and Vladan Vuletić. Direct laser cooling to bose-einstein condensation in a dipole trap. *Physical review letters*, 122(20):203202, 2019.

[42] Pablo Solano, Yiheng Duan, Yu-Ting Chen, Alyssa Rudelis, Cheng Chin, and Vladan Vuletić. Strongly correlated quantum gas prepared by direct laser cooling. *Physical review letters*, 123(17):173401, 2019.

[43] Mingjie Xin, Wui Seng Leong, Zilong Chen, Yu Wang, and Shau-Yu Lan. Fast quantum gas formation via electromagnetically induced transparency cooling. *Nature Physics*, 21(1):63–69, 2025.

[44] Aaron W Young, Shawn Geller, William J Eckner, Nathan Schine, Scott Glancy, Emanuel Knill, and Adam M Kaufman. An atomic boson sampler. *Nature*, 629(8011): 311–316, 2024.

[45] Adam M Kaufman, Brian J Lester, Collin M Reynolds, Michael L Wall, M Foss-Feig, KRA Hazzard, AM Rey, and CA Regal. Two-particle quantum interference in tunnel-coupled optical tweezers. *Science*, 345(6194):306–309, 2014.

[46] Benjamin M Spar, Elmer Guardado-Sanchez, Sungjae Chi, Zoe Z Yan, and Waseem S Bakr. Realization of a fermi-hubbard optical tweezer array. *Physical review letters*, 128(22):223202, 2022.

[47] Philipp M Preiss, Ruichao Ma, M Eric Tai, Alexander Lukin, Matthew Rispoli, Philip Zupancic, Yoav Lahini, Rajibul Islam, and Markus Greiner. Strongly correlated quantum walks in optical lattices. *Science*, 347(6227):1229–1233, 2015.

[48] Antoine Browaeys and Thierry Lahaye. Many-body physics with individually controlled rydberg atoms. *Nature Physics*, 16(2):132–142, 2020.

[49] T Grünzweig, Andrew Hilliard, M McGovern, and MF Andersen. Near-deterministic preparation of a single atom in an optical microtrap. *Nature Physics*, 6(12):951–954, 2010.

[50] Brian J Lester, Niclas Luick, Adam M Kaufman, Collin M Reynolds, and Cindy A Regal. Rapid production of uniformly filled arrays of neutral atoms. *Physical review letters*, 115(7):073003, 2015.

[51] Sepehr Ebadi, Tout T Wang, Harry Levine, Alexander Keesling, Giulia Semeghini, Ahmed Omran, Dolev Bluvstein, Rhine Samajdar, Hannes Pichler, Wen Wei Ho, et al. Quantum phases of matter on a 256-atom programmable quantum simulator. *Nature*, 595(7866):227–232, 2021.

[52] Dolev Bluvstein, Harry Levine, Giulia Semeghini, Tout T Wang, Sepehr Ebadi, Marcin Kalinowski, Alexander Keesling, Nishad Maskara, Hannes Pichler, Markus Greiner, et al. A quantum processor based on coherent transport of entangled atom arrays. *Nature*, 604(7906):451–456, 2022.

[53] Dolev Bluvstein, Simon J Evered, Alexandra A Geim, Sophie H Li, Hengyun Zhou, Tom Manovitz, Sepehr Ebadi, Madelyn Cain, Marcin Kalinowski, Dominik Hangleiter, et al. Logical quantum processor based on reconfigurable atom arrays. *Nature*, 626 (7997):58–65, 2024.

[54] Sepehr Ebadi, Alexander Keesling, Madelyn Cain, Tout T Wang, Harry Levine, Dolev Bluvstein, Giulia Semeghini, Ahmed Omran, J-G Liu, Rhine Samajdar, et al. Quantum optimization of maximum independent set using rydberg atom arrays. *Science*, 376 (6598):1209–1215, 2022.

[55] MA Norcia, H Kim, WB Cairncross, M Stone, A Ryou, M Jaffe, MO Brown, K Barnes, P Battaglino, TC Bohdanowicz, et al. Iterative assembly of 171 yb atom arrays with cavity-enhanced optical lattices. *PRX Quantum*, 5(3):030316, 2024.

[56] Hannah J Manetsch, Gyohei Nomura, Elie Bataille, Kon H Leung, Xudong Lv, and Manuel Endres. A tweezer array with 6100 highly coherent atomic qubits. *arXiv preprint arXiv:2403.12021*, 2024.

[57] Flavien Gyger, Maximilian Ammenwerth, Renhao Tao, Hendrik Timme, Stepan Snigirev, Immanuel Bloch, and Johannes Zeiher. Continuous operation of large-scale atom arrays in optical lattices. *Physical Review Research*, 6(3):033104, 2024.

[58] Aaron W Young, William J Eckner, Nathan Schine, Andrew M Childs, and Adam M Kaufman. Tweezer-programmable 2d quantum walks in a hubbard-regime lattice. *Science*, 377(6608):885–889, 2022.

[59] Aishwarya Kumar, Tsung-Yao Wu, Felipe Giraldo, and David S Weiss. Sorting ultracold atoms in a three-dimensional optical lattice in a realization of maxwell's demon. *Nature*, 561(7721):83–87, 2018.

[60] CM Chandrashekar and Raymond Laflamme. Quantum phase transition using quantum walks in an optical lattice. *Physical Review A—Atomic, Molecular, and Optical Physics*, 78(2):022314, 2008.

[61] Michal Karski, Leonid Förster, Jai-Min Choi, Andreas Steffen, Wolfgang Alt, Dieter Meschede, and Artur Widera. Quantum walk in position space with single optically trapped atoms. *Science*, 325(5937):174–177, 2009.

[62] Yoav Lahini, Mor Verbin, Sebastian D Huber, Yaron Bromberg, Rami Pugatch, and Yaron Silberberg. Quantum walk of two interacting bosons. *Physical Review A—Atomic, Molecular, and Optical Physics*, 86(1):011603, 2012.

[63] Taylor L Patti, Dominik S Wild, Ephraim Shahmoon, Mikhail D Lukin, and Susanne F Yelin. Controlling interactions between quantum emitters using atom arrays. *Physical review letters*, 126(22):223602, 2021.

[64] Sung-Mi Yoo. Strongly coupled cold atoms in bilayer dense lattices. *New Journal of Physics*, 20(8):083012, 2018.

[65] Daniel A Steck. Cesium d line data. 2003.

[66] Chen-Lung Hung. *In situ probing of two-dimensional quantum gases*. PhD thesis, The University of Chicago, 2011.

[67] Christopher J Foot. *Atomic physics*, volume 7. Oxford university press, 2005.

[68] Fam Le Kien, Philipp Schneeweiss, and Arno Rauschenbeutel. Dynamical polarizability of atoms in arbitrary light fields: general theory and application to cesium. *The European Physical Journal D*, 67:1–16, 2013.

[69] Christof Weitenberg, Manuel Endres, Jacob F Sherson, Marc Cheneau, Peter Schauß, Takeshi Fukuhara, Immanuel Bloch, and Stefan Kuhr. Single-spin addressing in an atomic mott insulator. *Nature*, 471(7338):319–324, 2011.

[70] Nicholas R Hutzler, Lee R Liu, Yichao Yu, and Kang-Kuen Ni. Eliminating light shifts for single atom trapping. *New Journal of Physics*, 19(2):023007, 2017.

[71] Orazio Svelto, David C Hanna, et al. *Principles of lasers*, volume 1. Springer, 2010.

[72] Yichao Yu, Nicholas R Hutzler, Jessie T Zhang, Lee R Liu, Jonathan D Hood, Till Rosenband, and K-K Ni. Motional-ground-state cooling outside the lamb-dicke regime. *Physical Review A*, 97(6):063423, 2018.

[73] P Jeffery Ungar, David S Weiss, Erling Riis, and Steven Chu. Optical molasses and multilevel atoms: theory. *Journal of the Optical Society of America B*, 6(11):2058–2071, 1989.

[74] Jean Dalibard and Claude Cohen-Tannoudji. Laser cooling below the doppler limit by polarization gradients: simple theoretical models. *Journal of the Optical Society of America B*, 6(11):2023–2045, 1989.

[75] Vladan Vuletić, Cheng Chin, Andrew J Kerman, and Steven Chu. Degenerate raman sideband cooling of trapped cesium atoms at very high atomic densities. *Physical Review Letters*, 81(26):5768, 1998.

[76] Andrew J Kerman, Vladan Vuletić, Cheng Chin, and Steven Chu. Beyond optical molasses: 3d raman sideband cooling of atomic cesium to high phase-space density. *Physical review letters*, 84(3):439, 2000.

[77] Egidijus Anisimovas, Fabrice Gerbier, Tomas Andrijauskas, and Nathan Goldman. Design of laser-coupled honeycomb optical lattices supporting chern insulators. *Physical Review A*, 89(1):013632, 2014.

[78] Adam M Kaufman, Brian J Lester, and Cindy A Regal. Cooling a single atom in an optical tweezer to its quantum ground state. *Physical Review X*, 2(4):041014, 2012.

[79] Zhuangzhuang Tian, Haobo Chang, Xin Lv, Mengna Yang, Zhihui Wang, Pengfei Yang, Pengfei Zhang, Gang Li, and Tiancai Zhang. Resolved raman sideband cooling of a single optically trapped cesium atom. *Optics Letters*, 49(3):542–545, 2024.

[80] Jonathon Gillen. *The Quantum Gas Microscope*. PhD thesis, Harvard University, 2009.

[81] Ahmed Omran. *A microscope for Fermi gases*. PhD thesis, Ludwig Maximilians Universität München, 2016.

[82] Jonathan Trisnadi. *The Design and Construction of a Quantum Matter Synthesizer*. PhD thesis, The University of Chicago, 2023.

[83] Mickey McDonald, Jonathan Trisnadi, Kai-Xuan Yao, and Cheng Chin. Superresolution microscopy of cold atoms in an optical lattice. *Physical Review X*, 9(2):021001, 2019.

[84] Sam Lantinga. Simple directmedia layer (sdl). `https://www.libsdl.org/`, 2025. Version 3.2.4.

[85] Jonathan Trisnadi, Mingjiamei Zhang, Lauren Weiss, and Cheng Chin. Design and construction of a quantum matter synthesizer. *Review of Scientific Instruments*, 93 (8), 2022.

[86] TL Gustavson, AP Chikkatur, AE Leanhardt, A Görlitz, Subhadeep Gupta, DE Pritchard, and Wolfgang Ketterle. Transport of bose-einstein condensates with optical tweezers. *Physical Review Letters*, 88(2):020401, 2001.

[87] Antoine Couvert, T Kawalec, G Reinaudi, and David Guéry-Odelin. Optimal transport of ultracold atoms in the non-adiabatic regime. *Europhysics Letters*, 83(1):13001, 2008.

[88] Stefan Kuhr, Wolfgang Alt, Dominik Schrader, Martin Muller, Victor Gomer, and Dieter Meschede. Deterministic delivery of a single atom. *Science*, 293(5528):278–280, 2001.

[89] Stefan Schmid, Gregor Thalhammer, Klaus Winkler, Florian Lang, and Johannes Hecker Denschlag. Long distance transport of ultracold atoms using a 1d optical lattice. *New Journal of Physics*, 8(8):159, 2006.

[90] Till Klostermann, Cesar R Cabrera, Hendrik von Raven, Julian F Wienand, Christian Schweizer, Immanuel Bloch, and Monika Aidelsburger. Fast long-distance transport of cold cesium atoms. *Physical Review A*, 105(4):043319, 2022.

[91] Alex J Matthies, Jonathan M Mortlock, Lewis A McArd, Adarsh P Raghuram, Andrew D Innes, Philip D Gregory, Sarah L Bromley, and Simon L Cornish. Long-distance optical-conveyor-belt transport of ultracold cs 133 and rb 87 atoms. *Physical Review A*, 109(2):023321, 2024.

[92] Markus Greiner, Immanuel Bloch, Theodor W Hänsch, and Tilman Esslinger. Magnetic transport of trapped cold atoms over a large distance. *Physical Review A*, 63(3): 031401, 2001.

[93] GT Hickman and M Saffman. Speed, retention loss, and motional heating of atoms in an optical conveyor belt. *Physical Review A*, 101(6):063411, 2020.

[94] Dylan O Sabulsky, Colin V Parker, Nathan D Gemelke, and Cheng Chin. Efficient continuous-duty bitter-type electromagnets for cold atom experiments. *Review of Scientific Instruments*, 84(10), 2013.

[95] JD Wong-Campos, KG Johnson, B Neyenhuis, J Mizrahi, and C Monroe. High-resolution adaptive imaging of a single atom. *Nature Photonics*, 10(9):606–610, 2016.

[96] Melles Griot. *Melles Griot Optics Guide: Gaussian Beam Optics*. CVI Melles Griot, 2009. Technical Guide, available online at `https://www.idexot.com/techguide-online`.

[97] Christian Gross and Waseem S Bakr. Quantum gas microscopy for single atom and spin detection. *Nature Physics*, 17(12):1316–1323, 2021.

[98] Alexander Impertro, Julian F Wienand, Sophie Häfele, Hendrik von Raven, Scott Hubele, Till Klostermann, Cesar R Cabrera, Immanuel Bloch, and Monika Aidelsburger. An unsupervised deep learning algorithm for single-site reconstruction in quantum gas microscopes. *Communications Physics*, 6(1):166, 2023.

[99] Andrew James Kerman. *Raman sideband cooling and cold atomic collisions in optical lattices*. PhD thesis, stanford university, 2002.

[100] A Fuhrmanek, R Bourgain, Yvan RP Sortais, and Antoine Browaeys. Light-assisted collisions between a few cold atoms in a microscopic dipole trap. *Physical Review A*, 85(6):062708, 2012.

[101] Brian J Lester, Adam M Kaufman, and Cindy A Regal. Raman cooling imaging: Detecting single atoms near their ground state of motion. *Physical Review A*, 90(1): 011804, 2014.

[102] Arthur La Rooij, C Ulm, E Haller, and S Kuhr. A comparative study of deconvolution techniques for quantum-gas microscope images. *New Journal of Physics*, 25(8):083036, 2023.

[103] Marc Cheneau, Romaric Journet, Matthieu Boffety, François Goudail, Caroline Kulcsár, and Pauline Trouvé-Peloux. Fast, accurate, and predictive method for atom detection in site-resolved images of microtrap arrays. *arXiv preprint arXiv:2502.08511*, 2025.

[104] Jonas Winklmann and Martin Schulz. Minimizing readout and state preparation time for neutral atom quantum computing. In *Software Engineering 2025–Companion Proceedings*, pages 10–18420. Gesellschaft für Informatik, Bonn, 2025.

[105] Lewis RB Picard, Manfred J Mark, Francesca Ferlaino, and Rick van Bijnen. Deep learning-assisted classification of site-resolved quantum gas microscope images. *Measurement Science and Technology*, 31(2):025201, 2019.

[106] Linipun Phuttitarn, B_M Becker, Ravikumar Chinnarasu, T_M Graham, and Mark Saffman. Enhanced measurement of neutral-atom qubits with machine learning. *Physical Review Applied*, 22(2):024011, 2024.

[107] Robert M Kent, Linipun Phuttitarn, Chaithanya Naik Mude, Swamit Tannu, Mark Saffman, Gregory Lafyatis, and Daniel J Gauthier. Efficient measurement of neutral-atom qubits with matched filters. *arXiv preprint arXiv:2504.08170*, 2025.

[108] Christopher M Bishop and Nasser M Nasrabadi. *Pattern recognition and machine learning*, volume 4. Springer, 2006.

[109] Kai-Niklas Schymik, Vincent Lienhard, Daniel Barredo, Pascal Scholl, Hannah Williams, Antoine Browaeys, and Thierry Lahaye. Enhanced atom-by-atom assembly of arbitrary tweezer arrays. *Physical Review A*, 102(6):063107, 2020.

[110] Weikun Tian, Wen Jun Wee, An Qu, Billy Jun Ming Lim, Prithvi Raj Datla, Vanessa Pei Wen Koh, and Huanqian Loh. Parallel assembly of arbitrary defect-free atom arrays with a multitweezer algorithm. *Physical Review Applied*, 19(3):034048, 2023.

[111] Woojun Lee, Hyosub Kim, and Jaewook Ahn. Three-dimensional rearrangement of single atoms using actively controlled optical microtraps. *Optics express*, 24(9):9816–9825, 2016.

[112] Hyosub Kim, Woojun Lee, Han-gyeol Lee, Hanlae Jo, Yunheung Song, and Jaewook Ahn. In situ single-atom array synthesis using dynamic holographic optical tweezers. *Nature communications*, 7(1):13317, 2016.

[113] Woojun Lee, Hyosub Kim, and Jaewook Ahn. Defect-free atomic array formation using the hungarian matching algorithm. *Physical Review A*, 95(5):053424, 2017.

[114] Hyosub Kim, Minhyuk Kim, Woojun Lee, and Jaewook Ahn. Gerchberg-saxton algorithm for fast and efficient atom rearrangement in optical tweezer traps. *Optics express*, 27(3):2184–2196, 2019.

[115] Maximilian Ammenwerth, Hendrik Timme, Veronica Giardini, Renhao Tao, Flavien Gyger, Ohad Lib, Dirk Berndt, Dimitrios Kourkoulos, Tim Rom, Immanuel Bloch, et al. Dynamical spatial light modulation in the ultraviolet spectral range. *arXiv preprint arXiv:2504.09529*, 2025.

[116] Rui Lin, Han-Sen Zhong, You Li, Zhang-Rui Zhao, Le-Tian Zheng, Tai-Ran Hu, Hong-Ming Wu, Zhan Wu, Wei-Jie Ma, Yan Gao, et al. Ai-enabled rapid assembly of thousands of defect-free neutral atom arrays with constant-time-overhead. *arXiv preprint arXiv:2412.14647*, 2024.

[117] Ivo HA Knottnerus, Yu Chih Tseng, Alexander Urech, Robert JC Spreeuw, and Florian Schreck. Parallel assembly of neutral atom arrays with an slm using linear phase interpolation. *arXiv preprint arXiv:2501.01391*, 2025.

[118] Shuai Wang, Wenjun Zhang, Tao Zhang, Shuyao Mei, Yuqing Wang, Jiazhong Hu, and Wenlan Chen. Accelerating the assembly of defect-free atomic arrays with maximum parallelisms. *Physical Review Applied*, 19(5):054032, 2023.

[119] Texas Instruments. DLP4500 .45 WXGA DMD Datasheet. `https://www.ti.com/lit/ds/symlink/dlp4500.pdf`, 2022. Revised May 2022.

[120] José CA Rocha, Terry Wright, Unė G Būtaitė, Joel Carpenter, George SD Gordon, and David B Phillips. Fast and light-efficient wavefront shaping with a mems phase-only light modulator. *Optics Express*, 32(24):43300–43314, 2024.

[121] Yibo Wang, Sayali Shevate, Tobias Martin Wintermantel, Manuel Morgado, Graham Lochead, and Shannon Whitlock. Preparation of hundreds of microscopic atomic ensembles in optical tweezer arrays. *npj Quantum Information*, 6(1):54, 2020.

[122] Yuki Torii Chew, Martin Poitrinal, Takafumi Tomita, Sota Kitade, Jorge Mauricio, Kenji Ohmori, and Sylvain de Léséleuc. Ultraprecise holographic optical tweezer array. *Physical Review A*, 110(5):053518, 2024.

[123] Nir Navon, Robert P Smith, and Zoran Hadzibabic. Quantum gases in optical boxes. *Nature Physics*, 17(12):1334–1341, 2021.

[124] Dustin Stuart and Axel Kuhn. Single-atom trapping and transport in dmd-controlled optical tweezers. *New Journal of Physics*, 20(2):023013, 2018.

[125] Aaron Smith, Thomas Easton, Vera Guarrera, and Giovanni Barontini. Generation of optical potentials for ultracold atoms using a superluminescent diode. *Physical Review Research*, 3(3):033241, 2021.

[126] Bichen Zhang, Pai Peng, Aditya Paul, and Jeff D Thompson. Scaled local gate controller for optically addressed qubits. *Optica*, 11(2):227–233, 2024.

[127] Ming-Jie Deng, Yuan-Yuan Zhao, Zi-Xin Liang, Jing-Tao Chen, Yang Zhang, and Xuan-Ming Duan. Maximizing energy utilization in dmd-based projection lithography. *Optics Express*, 30(4):4692–4705, 2022.

[128] Texas Instruments. DLPC350 DLP Datasheet. `https://www.ti.com/lit/ds/symlink/dlpc350.pdf`, 2019. Revised May 2019.

[129] Texas Instruments. DLP9000 DLP Datasheet. `https://www.ti.com/lit/ds/symlink/dlp9000.pdf`, 2016. October 2016.

[130] Klaus Hueck, Anton Mazurenko, Niclas Luick, Thomas Lompe, and Henning Moritz. Note: Suppression of khz-frequency switching noise in digital micro-mirror devices. *Review of Scientific Instruments*, 88(1), 2017.

[131] G Gauthier, I Lenton, N McKay Parry, M Baker, MJ Davis, H Rubinsztein-Dunlop, and TW Neely. Direct imaging of a digital-micromirror device for configurable microscopic optical potentials. *Optica*, 3(10):1136–1143, 2016.

[132] Paul B Wigley, Patrick J Everitt, Anton van den Hengel, John W Bastian, Mahasen A Sooriyabandara, Gordon D McDonald, Kyle S Hardman, Ciaron D Quinlivan, P Manju, Carlos CN Kuhn, et al. Fast machine-learning online optimization of ultra-cold-atom experiments. *Scientific reports*, 6(1):25890, 2016.

[133] Emil T Davletov, VV Tsyganok, VA Khlebnikov, DA Pershin, DV Shaykin, and AV Akimov. Machine learning for achieving bose-einstein condensation of thulium atoms. *Physical Review A*, 102(1):011302, 2020.

[134] Xiaoxiao Ma, Changwen Liang, Rong Sha, Chao Zhou, Qixue Li, Guochao Wang, Jixun Liu, Shuhua Yan, Jun Yang, and Lingxiao Zhu. Accelerated bayesian optimization in deep cooling atoms. *arXiv preprint arXiv:2412.11793*, 2024.

[135] Maxim Olshanii and David Weiss. Producing bose-einstein condensates using optical lattices. *Physical review letters*, 89(9):090404, 2002.

[136] Marcus Culemann. Construction and control of a dark spot optical tweezer array for a quantum gas microscope. Master's thesis, Ludwig-Maximilians-University Munich, 2024.

[137] DS Weiss, J Vala, AV Thapliyal, S Myrgren, U Vazirani, and KB Whaley. Another way to approach zero entropy for a finite system of atoms. *Physical Review A—Atomic, Molecular, and Optical Physics*, 70(4):040302, 2004.